6   # Recurrent evacuation of mantle mush by mafic recharge in

7   # ocean island basalts, recorded by La Palma clinopyroxene

8

9   Alberto Caracciolo*[1], Teresa Ubide[2], Mónica Ágreda-López[1], Raquel Herrera[3], Alvaro Marquez[4],

10 Diego González-García[4], Maria Jose Huertas[4], Eumenio Ancochea[4], Nicolás Chicharro[4,5], Juan

11 Jesús Coello-Bravo[6], Maurizio Petrelli[1]

12

13 [1] University of Perugia, Department of Physics and Geology, Perugia, Italy

14 [2] The University of Queensland, School of the Environment, Brisbane, Australia.

15 [3] Universidad Rey Juan Carlos, ESCET, Área de Geología, Tecvolrisk Research Group; Móstoles,

16 Madrid, Spain.

17 [4] Universidad Complutense, Área de Petrología y Geoquímica, Madrid, Spain.

18 [5] Instituto Geográfico Nacional. Centro Geofísico de Canarias, Santa Cruz de Tenerife, Tenerife,

19 Spain

20 [6] Fundación Telesforo Bravo - Juan Coello; Puerto de la Cruz, Tenerife, Spain.

21

22 Corresponding author: *Alberto Caracciolo, (alberto@hi.is)

23

24

Abstract

Temporal variations in magma plumbing architecture and magmatic processes influence eruption priming and the interpretation of pre- and syn-eruptive signals. Yet, how these processes operate in low-flux volcanoes remains poorly constrained, leaving a key gap in understanding eruption precursors. Here we examine the temporal evolution of magmatic processes at La Palma, Canary Islands, a low-flux ocean-island basaltic system, by interrogating the clinopyroxene zoning record from three historical eruptions during which lava composition transitioned from tephritic to basanitic: El Charco 1712, Teneguía 1971, and Tajogaite 2021. By combining major and trace element data from clinopyroxenes and carrier melts with textural observations, thermobarometry, quantitative trace element mapping, and cluster analysis, we reconstruct the magmatic processes and storage conditions preceding these eruptions. Both tephritic and basanitic magmas were stored in the upper mantle (18–25 km depth) together with an evolved tephritic to phonolitic mush preserved in clinopyroxene antecryst cores. The phonolitic mush was stored at lower temperatures and likely originated by >80% fractionation of a basanitic melt. Repeated injections of basanite recharge melts gradually eroded and remobilized this mush, after which the recharge magma underwent ~10-20% fractional crystallization, producing a tephritic melt. Despite its pivotal role in priming the system, mafic recharge did not act as the immediate trigger for the La Palma historical eruptions. Early-erupted tephrite-hosted clinopyroxenes lack clear recharge-related signatures in their inner rims, suggesting that eruption onset was more likely linked to internal evolution of the reservoir.

Introduction

48   The dynamics of magma plumbing systems regulate not only the timing, composition, and

49   style of volcanic eruptions, but also key subsurface processes such as magma recharge, mixing,

50   and crystal mobilization [e.g.1,2]. Temporal changes in the configuration and behaviour of magma

51   feeding and storage systems can influence eruption priming and the run-up to volcanic activity,

52   with implications for interpreting monitoring signals and improving forecasts. Variations in volcanic

53   plumbing systems over time have recently been explored in high-flux basaltic systems where

54   eruptions are relatively frequent (e.g., Iceland and Hawaii[3–6]). Such variations, however, remain

55   largely underexplored in low-flux basaltic systems where the low eruption periodicity and varied

56   eruption location translate into monitoring challenges and increased risk potential.

57   Magmatic processes occurring within a magma plumbing cannot be directly observed, yet

58   they can be inferred from the chemical zoning and textural features of erupted minerals. This is

59   because growing magmatic crystals can record the thermodynamic and chemical conditions of

60   the magma from which they crystallize, preserving detailed archives of magma evolution and

61   dynamics in their zoning patterns [e.g. 2,7]. In particular, clinopyroxene crystals are outstanding

62   recorders of magmatic processes, as they crystallize over a wide range of depths [e.g. 8] and

63   preserve trace element zoning due to slow diffusion rates[7]. La Palma, the most volcanically active

64   island of the Canary Islands in historical time (eight eruptions since the 15th century), is a great

65   candidate for studying the temporal evolution of magma plumbing characteristics at relatively low-

66   flux ocean island basalt (OIB) systems via clinopyroxene records, as (1) the eruptive products

67   contain abundant clinopyroxene crystals (2) there is a detailed record of historical eruptions [e.g.

68   9,10], (3) recent eruptions have shown petrological variations reflecting remobilization of mushes of

69   basanite to phonolite compositions [11–17] and (4) recent magmatic reactivation led to the 2021

70   Tajogaite eruption with major economic and societal consequences[18]. A study focusing on the

71   temporal evolution of the magma plumbing system feeding historical magma plumbing at La

72   Palma is urgent and lacking to date. Specifically, magma storage is considered to take place

73   dominantly at upper mantle depths [12,14,15,17,19,20] but the relevance of shallow crustal storage and

74   the links between erupted lithologies and storage depths, essential for monitoring efforts, remains

75   unclear.

76   In this work, we interrogate the zoning records preserved in clinopyroxene crystals from

77   three historical eruptions at La Palma: El Charco 1712, Teneguía 1971 and Tajogaite 2021 (Fig.

78   1). All three eruptions erupted early tephrite followed by later basanite lavas [17,21,22] and some lavas

79   hold evidence of phonolitic mush at depth, despite not erupted [14,23]. Specifically, we integrate new

80   major and trace element data across clinopyroxene textures with quantitative trace element

81   mapping, pressure–temperature constraints, and cluster analysis. We combine the mineral

82   dataset with major and trace element geochemistry of the associated carrier melts. By merging

83   these new results with previous work on the 2021 Tajogaite eruption and earlier historical

84   eruptions, we find a striking consistency in the magma chemistry and plumbing system anatomy

85   during historical time, highlighting the key role of mafic recharge in priming plumbing systems at

86   low-flux OIB volcanoes.

87

88 Results

89 Petrography and clinopyroxene textures

90   Lava samples in this study classify as tephrites and basanites based on petrographic

91   observations. Both rock types are porphyritic and contain large crystals of clinopyroxene and Fe-

92   Ti oxides. Tephrites are distinguished by the presence of amphibole (kaersutite), while basanites

93   have olivine (Fig. 2).

94   Clinopyroxene crystals from the three eruptions range up to 5000 μm in size and are

95   referred to with the general term crystals, while those smaller than 100 μm are termed microlites.

96   Clinopyroxene can be found as standalone crystals surrounded by the groundmass or as mineral

97   inclusion in rare plagioclase crystals[14]. Across all eruptions, clinopyroxene can host inclusions of

98   apatite, Fe-Ti oxides, and glassy to microcrystalline melt inclusions (Fig. 2). The groundmass is

99   microcrystalline and predominantly composed of plagioclase, clinopyroxene, and Fe–Ti oxides,

100   as well as olivine in the basanites and amphibole in the tephrites (Fig. 2). Clinopyroxene crystals

101   can be broadly divided into three main textural zones across the three eruptions: core, inner rim,

102   and outer rim. The cores represent the innermost parts of the crystals and are texturally complex,

103   characterized by patchy or sector zoning in back-scattered electron (BSE) images (Fig. 2G-I).

104   Under the petrographic microscope, clinopyroxene cores are green or light brown in plane

105   polarised light, surrounded by brown rims that are often sector zoned. In BSE, the inner rims

106   appear as darker zones than the cores, suggesting an increase in Mg (reverse zoning; Fig. 2G-

107   I). The outermost zone, in contact with the groundmass, is the outer rim, usually forming a

108   relatively thin (5-30 μm) layer that returns lighter BSE contrast (Fig. 2G-I).

109

Clinopyroxene major elements

111   Clinopyroxene crystals from all eruptions are diopside in composition and do not display

112   geochemical differences in terms of En $[Mg / (Ca + Mg + Fe) \times 100]_{mol}$, Fs $[Fe / (Ca + Mg + Fe) \times$

113    $100]_{mol}$, Wo $[Ca / (Ca + Mg + Fe) \times 100]_{mol}$ components (Fig. S6) and Mg# values ($[Mg / (Mg +$

114    $Fe)] \times 100$, molar basis), which range from 52 to 86 (El Charco 1712, Mg#52-84, n=213; Teneguía

115   1971, Mg#56-86, n=164; Tajogaite 2021, Mg#56-86, n=786). However, there are consistent Mg#

116   variations from cores to inner and outer rims. Cores show the broadest range of Mg# values within

117   each eruption (El Charco 1712, Mg#52-83; Teneguía 1971, Mg#60-84; Tajogaite 2021, Mg#56-

118   86), with compositions Mg#<67 consistent with green cores. Inner rims consistently have higher

119   Mg# values defining reverse zoning (El Charco 1712, Mg#74-84; Teneguía 1971, Mg#74-83;

120   Tajogaite 2021, Mg#69-84) and outer rims have lower Mg# 68–78 across the eruptions. Microlites

121   span a range that overlaps both inner and outer rims, encompassing the full range defined by

122   these two textural zones (El Charco 1712, Mg#70-80; Teneguía 1971, Mg#69-80; Tajogaite 2021,

123   Mg#69-82) (Fig. 3 and S7).

124   Bivariate plots of Mg# versus major and minor elements show that clinopyroxene inner

125   rims, outer rims, and microlites generally align along a coherent negative trend in diagrams such

126   as Mg# vs TiO_2, Al_2O_3, and Na_2O, or a subtle positive trend with CaO or Cr_2O_3 (Fig. 3 and S8).

127   Inner rims define the primitive end of the trend, showing higher Mg#-Cr_2O_3 and lower TiO_2-Al_2O_3

128   contents compared to outer rims (Fig. 3 and S8). Microlites span the full compositional range

129   defined by inner and outer rims. In contrast, clinopyroxene cores are scattered over a broad

130   compositional range, including along the main trend but mostly outside of it (Fig. 3 and S8). Core

131   compositions span from primitive, Mg#-rich and TiO_2-poor types, to more evolved, visually green,

132   Mg#-poor and Na_2O-rich compositions, which in Tajogaite 2021 are occasionally found with

133   samples containing rare large crystals of plagioclase [14,17].

134   Overall, clinopyroxene compositions do not systematically vary with host rock type.

135   Crystals from both tephrites and basanites span the full compositional range, though the most

136   evolved cores, with the lowest Mg#, occur mainly in basanites (Fig. S9).

Clinopyroxene trace elements

138   Compatible elements in clinopyroxene such as Cr, Sc, and Ni, exhibit high concentrations

139   and broad variability at low Zr contents (<200 ppm), reflecting more primitive compositions. In

140   contrast, high-Zr (>400 ppm), evolved compositions, are characterized by consistently low

141   concentrations of these elements (Fig. 4A-C and S10). Within each eruption, Cr concentration in

142 clinopyroxene inner rims and microlites increases from early-erupted tephrite-hosted to late-

143 erupted basanite-hosted clinopyroxene (Fig. 4G-I).

144   Incompatible trace elements correlate positively with Zr, with data from all eruptions

145 aligning along a common trend (Fig. 4D-F and S11-S12). At Zr ~400 ppm, some clinopyroxene

146 compositions diverge from this main trend, especially for elements like Y and middle and heavy

147 rare earth elements (MREE-HREE) like Sm, Nd, Eu, Gd, Dy (Fig. 4D-F and S11-S12). High-Zr

148 compositions (>400 ppm) are mostly observed in evolved clinopyroxene cores, which are slightly

149 enriched in HREE (Tm, Yb, Lu) compared to other core compositions (Fig. S15). Normalized

150 clinopyroxene trace element are broadly similar across eruptions, without notable differences

151 between tephrite and basanite samples (Fig. S13-S14). Clinopyroxene cores display both

152 enriched and depleted compositions, while inner rims are generally more depleted than outer rims

153 and microlites (Fig. S13). Overall, trace element patterns are parallel, with consistent trace

154 element abundances across the eruptions (Fig. S13-S14).

155   Clinopyroxene trace-element maps reveal chemical complexities not visible in BSE

156 images (Fig. 5 and Fig. S23). The cores often exhibit extreme heterogeneity with patchy domains,

157 subgrains and/or sector zoning (Fig. 5). Core compositions span from primitive (high Cr, Ni, Sc;

158 low Zr, Mn) to evolved (low Cr, Ni, Sc; high Zr, Mn), mirroring single-spot analyses. Contacts

159 between cores and surrounding portions of the crystal are usually rounded, particularly around

160 evolved cores (low Cr, Sc, Ni; high Zr, Mn). A key feature is the high Cr, Ni and Sc concentration

161 of clinopyroxene inner rims, consistently present across all mapped clinopyroxene crystals,

162 reaching up to 3500 ppm of Cr (Fig. 5 and S23) and increasing from tephrite to basanite as

163 observed for individual eruptions (Fig. 4G-I). The inner rims are either in contact with the

164 groundmass directly or, more frequently, are surrounded by thin outer rims characterized by a

165 drop in Cr, Sc, and Ni and higher Zr, Ti, and Mn relative to inner rims (Fig. 5 and S23). Multiple

166 high-Cr zones are observed in the zoning record of tephrite- and basanite-hosted clinopyroxenes

167   from Teneguía 1971 and Tajogaite 2021, whereas in El Charco 1712 they are restricted only to

168   single inner rims (Fig. S16).

169

Major and trace element composition of the matrix

171   The matrix from the Teneguía 1971 and El Charco 1712 eruptions ranges in composition

172   from basanite to tephrite, overlapping matrix results from the Tajogaite 2021 eruption (Fig. S17)

173   [17]. The mean MgO content of the matrix is 4.9 ± 0.7 wt% and 4.8 ± 0.9 wt% in El Charco 1712

174   and Teneguía 1971, respectively, similar to the matrix from the 2021 Tajogaite eruption of 4.7 ±

175   0.7 wt% (Fig. 6A)[17].

176   Tephrite matrices display slightly higher Zr and incompatible trace element concentrations

177   than basanites, indicating a more evolved character (Fig. 6B-C). Basanite compositions from the

178   Tajogaite 2021 and Teneguía 1971 eruptions are similar and define overlapping fields (Fig. 6B-

179   C). In contrast, basanites from El Charco 1712 are more evolved, plotting close to the tephrite

180   fields of the other eruptions. The El Charco 1712 tephrite matrix is the most evolved, reaching the

181   highest Zr and incompatible element concentrations (Fig. 6B–C), consistent with its most enriched

182   trace-element patterns (Fig. 6D-F).

183

Pressure and temperature of clinopyroxene crystallization

185   Primitive clinopyroxene cores exhibit the greatest pressure variability within individual

186   eruptions, extending down to 9.4 kbar (32 km) (Fig. 7A-C). Most primitive core pressures,

187   hereafter defined as within the 10th–90th percentile, range from 6.4–7.7 kbar (22.2–26.5 km) for

188   El Charco 1712, 6.2–6.9 kbar (21.5–23.9 km) for Teneguía 1971, and 6.6–8.6 kbar (22.9–29.4

189   km) for Tajogaite 2021. Evolved cores (Mg# < 67) record lower pressures, mostly 4.3–6.1 kbar

190   (15.3–21.2 km), than primitive cores, with no systematic differences across eruptions (Fig. 7A-C).

191   Inner rims, outer rims, and microlites show broadly similar pressure distributions across all

192   eruptions (Fig. 7A-C). Inner rim pressures cluster within 5.4–7.0 kbar (19.7–24.2 km), outer rims

193   within 5.0–7.0 kbar (17.6–24.2 km), and microlites between 5.2–7 kbar (18.3–24.2 km). Overall,

194   clinopyroxene barometry indicates upper mantle storage (below the local Moho at 10-14 km[24,25].

195   We do not observe pressure differences across eruptions and textures beyond calibration

196   uncertainties, except for some primitive cores likely crystallizing deeper (>7 kbar) than other

197   textural categories (Fig. 7A-C).

198   Regarding temperatures, primitive clinopyroxene cores (1107-1145 °C), inner rims (1129-

199   1155 °C), outer rims (1114 – 1147 °C) and microlites (1118 – 1153 °C) exhibit comparable

200   temperature ranges across eruptions. The evolved cores record the lowest temperatures (1001 –

201   1025 °C), with no significant differences across the three eruptions (Fig. 7D-F).

202

Discussion

Limited temporal variation of tephrite-basanite carrier melts

205   The microcrystalline matrix represents a crystal-free proxy for carrier melts, unlike whole-

206   rock compositions, which are often influenced by recycled crystals[17,26]. Major element

207   homogeneity over time (~5 wt% MgO, in agreement with the filtering of OIB melts to eruptible

208   liquids[26]) is mirrored in the trace elements, as matrix compositions from all three eruptions define

209   a single array in incompatible trace element space (Fig. 6). The only notable difference is the

210   more evolved trace element character of tephrite melts from the El Charco 1712 eruption. REE

211   patterns are parallel across all eruptions, indicating compositions controlled by fractional

212   crystallization. Trace element modelling shows that within each eruption, the transition from

213 basanite to tephrite requires only ~10-20% fractionation (Fig. 6B-D). However, the more evolved

214 El Charco 1712 matrices require ~20-30% fractionation (Fig. 6B-D). This higher degree of

215 fractionation does not appear to correlate with pre-eruption repose time, as only 35 years

216 separated El Charco 1712 from the previous eruption (San Antonio 1677). This timescale is

217 shorter than the 50-year break preceding Tajogaite 2021 and longer than the 22 years preceding

218 Teneguía 1971. Instead, the more evolved character of El Charco 1712 carrier melts may reflect

219 limited mafic recharge into the system, allowing greater crystal fractionation and melt

220 differentiation. This is supported by the lack of evidence for multiple high-Cr recharge events in

221 mapped clinopyroxenes from El Charco 1712, in contrast to the periodic high-Cr recharge

222 signatures identified in clinopyroxenes from Teneguía 1971 and Tajogaite 2021 (Fig. S16).

Upper mantle magma storage

224   Based on our clinopyroxene-melt themobarometric calculations performed on new data

225 and published compositions, clinopyroxene crystallization depths and temperatures appear

226 consistent both within individual eruptions and across historical time, within uncertainties of the

227 applied thermobarometers (Fig. 7). The only exceptions are a subset of primitive cores, which

228 likely suggest deeper crystallization relative to other textural groups, and the evolved cores, which

229 crystallised at lower temperatures. Regardless of the calibration used, clinopyroxene crystals

230 consistently record crystallization within the upper mantle beneath La Palma (Fig. 7 and S4-S5),

231 at depths of approximately 18–25 km, with some primitive cores likely crystallizing below 25 km.

232 These depths are consistent with the location of seismicity recorded before and during the 2021

233 Tajogaite eruption at 20-25 km depth[25].

234   Our results align with previous barometry studies on the 2021 Tajogaite eruption.

235 González-García et al. (2023)[19] applied the thermobarometer of Mollo et al. (2018)[27] to

236 clinopyroxene cores and rims, reporting pressures (10th–90th percentile) within the range of 6.0–

237   7.9 kbar (21–27 km depth). Similarly, pressures derived from amphibole crystals span 5.4–

238   7.8 kbar (19–27 km), suggesting similar storage depths for both tephrite and basanite magmas

239   [12,19]. Ubide et al. (2023)[17] applied the Putirka et al. (2003)[28] barometer to inner rims and microlites,

240   obtaining pressures in the range of 2.8–6.9 kbar (10–24 km). Our Tajogaite 2021 inner rims and

241   microlites (5.5–7.0 kbar; 19–24 km) fall within the lower part of that depth range. This difference

242   may reflect different equilibrium criteria and thermobarometers, though results agree within

243   uncertainties. Romero et al. (2022)[29] report higher clinopyroxene crystallization pressures

244   between 7.6 – 11.7 kbar (26-40 km), similar to those calculated by Castro and Feisel (2022)[30], in

245   the range 7-10 kbar (24-34 km) and to those obtained by Chamberlain et al. (2025)[12], where mean

246   pressures for clinopyroxene cores, rims and microlites are between 7.3-8.6 kbar (25-29 km).

247   These studies used the calibration of Neave and Putirka (2017)[31], which is not specifically

248   designed for mafic alkaline magmas and is noted here to yield higher pressure estimates for

249   Tajogaite 2021 compared to barometers calibrated for such compositions (Fig. S4). An upper

250   mantle extraction depth is also corroborated by melt and fluid inclusion studies during the 2021

251   Tajogaite eruption, which point out magma storage depth between 15-30 km[20,32]. Similarly,

252   microthermometry on fluid inclusions from Tajogaite 2021 indicates magma storage at depths of

253   22 to 27 km, in addition to a shallower zone at 4 to 16 km depth[33]. The existence of this shallow

254   zone, likely containing early-erupted tephrite magma, is also supported by experimental

255   studies[34,35] and shallow seismicity at 10-12 km during the 2021 Tajogaite eruption[25,36].

256   Interestingly, we do not observe evidence for this shallow zone in the petrological record, nor in

257   the storage depths of tephrite magmas derived from amphibole-based barometry[19], nor in the

258   depth of phonolite-like magmas derived from inclusions of clinopyroxene in plagioclase crystals[14].

259   This suggests that this shallow zone is somewhat cryptic and may represent a transient storage

260   level rather than a mature reservoir, where early-erupted tephrite magmas temporarily stagnate

261   with insufficient time for clinopyroxene to re-equilibrate[37].

262   Our results also agree with findings from previous literature concerning other historical

263   eruptions at La Palma. Previous studies on the Teneguía 1971 eruption report storage depths of

264   20–45 km[11,38]. These estimates are deeper than those obtained in our study, likely because they

265   used whole-rock compositions instead of matrix or glass, which typically results in overestimated

266   pressures and temperatures[39]. Additionally, we note that the Teneguía 1971 clinopyroxene

267   compositions for these studies [11,38], acquired using the same EMPA instrument, show

268   systematically lower CaO and slightly higher Na_2O contents compared to our data (Fig. S8).

269   These differences may reflect a calibration issue affecting CaO and Na_2O measurements (Fig.

270   S8), with lower CaO and higher Na_2O in those datasets potentially explaining the higher-pressure

271   estimates. The 1949 San Juan eruption was also fed by magma reservoir located at 21- 27 km

272   or deeper, according to clinopyroxene-melt barometry[23]. Fluid inclusions in olivine and

273   clinopyroxene crystals from the 1949 San Juan eruption record entrapment pressures of 6.0-6.8

274   kbar (21-24 km) and 2-3.4 kbar (8-12 km)[40]. Overall, published thermobarometry on historical

275   eruptions is consistent with findings from the 2021 Tajogaite eruption and our work, revealing

276   temporally consistent magma storage of eruption-feeding reservoirs under Cumbre Vieja.

277

278   # Clinopyroxene records of magma history: Coupling clustering

279   texture, chemistry, and thermobarometry

280

281   ## Evolved melts related to cold phonolitic mushes in the upper mantle

282   Clusters 0 and 1 are characterized by the highest Zr and Mn contents and the lowest Cr,

283   Sc, and Ni concentrations (Fig. 8). Cluster 1 differs from Cluster 0 by slightly higher Cr, Sc, and

284   Ni. Both clusters show the most enriched REE patterns (Fig. S18-S19). They occur exclusively in

285   clinopyroxene cores and often form patchy domains (Fig. 9). When present in other textural

286   positions, they are restricted to microlite cores, as shown by cluster-colored microlite maps (Fig.

287   9A–B), likely representing core remnants of larger crystals. The exclusive occurrence of Clusters

288   0 and 1 in mineral cores and their resorbed textures suggest crystallization at depth, from melts

289   no longer present at the time of eruption. We interpret these clusters as representing evolved and

290   fractionated melt compositions growing patchy cores with relatively low Mg# values (Fig. S7 and

291   S20A), compositions in major- and trace element disequilibrium with the tephrite-basanite carrier

292   melts (Fig. S7 and S21). Clusters 0 and 1 clinopyroxenes also define a separate evolutionary

293   trend in the Mg – Na – Fe2+(+Mn) diagram[41] compared to tephrite and basanite related

294   compositions (see 4.3.3), suggesting a different origin (Fig. S22). We therefore infer that Clusters

295   0 and 1 represent clinopyroxene antecrysts that did not crystallize from carrier liquids but instead

296   formed in evolved melt pockets within a crystal mush (Fig. 10).

297   To investigate the nature of these evolved melt pockets, we calculated the trace element

298   composition of melts in equilibrium with clinopyroxene, using partition coefficients (Kd) derived

299   from multiple parameterizations[42] (see Supplement). The reconstructed melt compositions define

300   a trend broadly consistent with fractional crystallization, with Clusters 0 and 1 representing the

301   most differentiated compositions (Fig. S21D-F). Despite uncertainties from using fixed Kd values,

302   our fractional crystallization modelling, starting from a primitive basanite matrix composition from

303   2021, indicates that up to 80–90% crystallization is required to produce the most evolved

304   reconstructed melt compositions represented by Clusters 0 and 1 (Fig. S21). This aligns with the

305   ~80-85% crystallization estimated to generate phonolitic magmas from basanitic magmas

306   beneath La Palma[43,44] and OIB settings in general[45]. We also observe fractionation of Y, MREE,

307   and, to a lesser extent, HREE at fixed Zr in Clusters 0 and 1, with these elements showing lower

308   concentrations in reconstructed melt compositions relative to LREE (Fig. 22). This likely reflects

309   increased partitioning of MREE and HREE into amphibole and clinopyroxene during fractionation

310   of evolved alkali melts, depleting the residual melts in these elements[46]. Additionally, most of the

311 REE patterns of clinopyroxene from Clusters 0 and 1 show an upward inflection of HREE (Tm,

312 Yb, Lu) compared to light REE. This is a typical behaviour of high-Na clinopyroxene crystallizing

313 from phonolite melts, where HREE preferentially partition into the M1 site, whereas other REE

314 remain mostly distributed in the M2 site [e.g.14,47]. All together, these observations support the

315 occurrence and recycling of a phonolite-like mush under La Palma, as also supported by other

316 studies focused on plagioclase antecrysts[14]. The occurrence of grey phonolitic xenopumice

317 fragments in the Tajogaite 2021 products[13] and the presence of minor phonolitic outcrops across

318 Cumbre Vieja[15,16] further indicates that magma storage at multiple levels beneath La Palma

319 commonly results in the formation of phonolites.

320 Understanding the depth of crystallization of phonolite-derived Clusters 0 and 1

321 clinopyroxene cores is challenging, as the exact composition of the melts from which crystallized

322 is unknown. There is evidence that evolved tephriphonolite and phonolite rocks form within the

323 lowermost crust under La Palma[15]. However, as also suggested by Klugel et al. (2022)[15],

324 formation of phonolites cannot be solely related to the lower crust. Our evolved clinopyroxene

325 cores represented by Clusters 0 and 1 are surrounded by tephritic to basanitic inner rims (Fig. 9)

326 formed at upper mantle depths and at 1129-1155 °C (see 5.2), in line with literature findings[17,19].

327 Considering that basanite-tephrite inner rims crystallized in the mantle during historical time,

328 evolved clinopyroxene cores must also have formed in the mantle. Jegal et al. (2025)[14] estimated

329 pressures of 5.4 ± 0.8 kbar and temperatures of 1021 ± 6 °C for a green evolved clinopyroxene

330 included in a plagioclase antecryst, by pairing them with a titanite-hosted tephriphonolitic melt

331 inclusion. Building on this approach, we used a Monte Carlo simulation starting from that melt

332 inclusion composition as putative liquid for our evolved clinopyroxene cargo, finding mean

333 crystallization depths for evolved clinopyroxene from El Charco 1712, Teneguía 1971 and

334 Tajogaite 2021 of 4.8 ± 0.8 kbar (17 ± 2.9 km), 5.1 ± 0.4 kbar (18 ± 1.5 km) and 5.0 ± 0.8 kbar

335 (18 ± 2.9 km). Mean temperatures of evolved clinopyroxene for the same eruptions are 1021 ±

336 13 °C, 1018 ± 8 °C and 1019 ± 12 °C, respectively. Our results agree with Jegal et al. (2025)[14],

337   placing evolved clinopyroxene crystallization in a cold upper mantle storage region (Fig. 10), as

338   also observed at other OIB volcanoes[48].

339

Magma recharge and subsequent differentiation

341   Cluster 5 displays the highest Cr, Ni, and Sc and lowest Zr and Mn concentrations (Fig.

342   8). It is the most depleted in REE and the least fractionated, with Mg#>67 (Fig. S18 and S20A).

343   Cluster 3 is similar to Cluster 5 but is distinguished by lower Cr, Sc, and Ni concentrations (Fig.

344   8) and a slightly more fractionated character (Fig. S18). In general, Clusters 3 and 5 are found in

345   primitive cores, inner rims, and microlites, all with Mg# >67 (Fig. S20A). Their major and trace

346   element compositions are in chemical equilibrium with carrier melts, suggesting that they are true

347   phenocrysts (Fig. S7 and S21). In basanite-hosted clinopyroxenes, Cluster 5 consistently

348   characterizes the inner rims across all eruptions, typically forming a homogeneous euhedral zone

349   (Fig. 9). In contrast, in tephrite-hosted clinopyroxenes, inner rims are characterized by the more

350   fractionated Cluster 3, preceded by Cluster 5 compositions (Fig. 9). Importantly, the pattern that

351   emerges from these observations is that inner rims are commonly associated to clusters 3 and 5,

352   which define reverse zoning relative to cores.

353   The dominance of primitive inner rims suggests mafic magma recharge prior to eruptions,

354   similar to other low-flux basaltic volcanoes (e.g., Etna[7,49]). We interpret Cluster 5 as representing

355   pre-eruptive basanite recharge that disrupts the resident crystal mush (Fig. 10). As for Cluster 3,

356   its trace element composition suggests crystallization from a magma that underwent fractionation

357   following mafic recharge, sufficient to deplete the melt in compatible elements. Cluster 3 therefore

358   represents a slightly more fractionated flavour of Cluster 5, likely linked to the tephrite magma

359   (Fig. 10). However, the significance of Cluster 3 is complex, as it occurs in different textural

360   positions. When present in clinopyroxene cores, Cluster 3 either forms homogeneous cores

361   (Teneguía 1971, Tajogaite 2021), or patchy domains (El Charco 1712) or is linked to Cluster 5

362   through sector zoning (Fig. 9B). The occurrence of Cluster 3 in mineral cores suggests that the

363   remobilized mush was liked zoned, i.e., not composed exclusively of phonolitic antecrysts

364   (Clusters 0 and 1), but also contained tephritic crystals (Cluster 3). Importantly, in tephrite-hosted

365   clinopyroxene, Cluster 3 dominates inner rims, which consistently overgrows Cluster 5

366   compositions, suggesting fractionation following mafic recharge. In contrast, in basanite-hosted

367   clinopyroxene, Cluster 3, when present, generally precedes the final mafic recharge event in the

368   zoning record (Fig. 9). Although we lack temporal constraints for the El Charco 1712 samples,

369   tephrite samples erupted earlier than the basanites[22], similar to the 1971 Teneguía[21] and 2021

370   Tajogaite eruptions[17]. To explore the temporal variation of mafic recharge in the three eruptions,

371   we examined Cr concentrations in inner rims and microlites (Fig. 4G-I). Cr concentrations are

372   significantly lower in the early-erupted tephrite-hosted clinopyroxene inner rims and microlites

373   compared to those in basanite-hosted clinopyroxene. This pattern is consistent with observations

374   from the 2021 Tajogaite eruption, where there is evidence for a progressive and gradual increase

375   in Cr concentration of recharge melts over the course of the eruption (Fig. 4I), similar to recent

376   basaltic eruptions where similar datasets are available (e.g., Mt Etna 2021 paroxysms[49]). Cluster-

377   coloured maps also show Cr-poor, Cluster 3 inner rims in tephrite-hosted clinopyroxene and Cr-

378   rich, Cluster 5 inner rims in basanite-hosted clinopyroxene (Fig. 9). Hence, considering similarities

379   with the 2021 Tajogaite eruption, we argue that also during El Charco 1712 and Teneguía 1971,

380   there was a progressive input of a mafic magma that gradually evacuated and remobilized a

381   tephritic to phonolitic crystal mush in the upper mantle (Fig. 10).

382

Cryptic primitive seed for the phonolite lineage?

384   Cluster 4 is characterized by the lowest Ti, V and Al_2O_3 concentrations, coupled with

385   relatively high Cr and Ni contents, although lower than those of Cluster 5 (Fig. 8 and S20). It is

386   extremely rare, occurring as single-spot data in two cores from Teneguía 1971 and Tajogaite

387 2021. In mapped clinopyroxenes, it appears as a large, resorbed core in one crystal from

388 Tajogaite 2021 and as patches within a Cluster 1 core in one crystal from El Charco 1712. Despite

389 its sporadic occurrence and geochemical characteristics, Cluster 4 likely represents a melt

390 composition that crystallized at depth, as it is confined to mineral cores. The lower Cr

391 concentrations and the highly resorbed clinopyroxene core mapped in Tajogaite 2021 (Fig. 9C)

392 suggest crystallization from a less mafic melt than the recharge magma, followed by partial

393 dissolution during interaction with the recharging melt. The low Ti, V and Al_2O_3 contents of Cluster

394 4 suggest crystallization at low degrees of undercooling, possibly in a quiet magmatic

395 environment, during which Al, Ti and V remain in the residual melt due to crystallization kinetics

396 [50,51].

397   The major element composition of Cluster 4 clinopyroxenes defines an evolutionary trend

398 in the Mg–Na–Fe^{2+}(+Mn) diagram[41] that highlights its transitional nature between basanite

399 (Cluster 3 and 5) and phonolite (Cluster 0) (Fig. S22). Cluster 4 cores fall at the start of the

400 phonolitic trend, suggesting it records a primitive composition, capable of evolving into phonolitic

401 melts.

402

Magma ascent in the plumbing system

404   Cluster 2 is marked by the highest Ti, V and Al_2O_3 concentrations, along with elevated Sc

405 levels, while Cr remains similar to Cluster 1 (Fig. 8 and S20). Cluster 2 is predominantly found in

406 outer rims, together with a minor proportion of Cluster 1 in El Charco 1712 and Teneguía 1971

407 samples. Microlites also show Cluster 2, but only in their outermost portions (Fig. 9). Therefore,

408 Cluster 2 is related to the very final crystallization process following mafic recharge, and its

409 increased uptake of Al-Ti is consistent with crystallisation at high degrees of undercooling during

410 magma ascent [7,51]. The Cr-poor, Ti- and Al-rich character of Cluster 2, and its textural dominance

411   in outer rims, are consistent with crystallization during magma ascent and surface crystallization

412   upon lava emplacement (Fig. 10), as also suggested at Etna volcano [7,49].

Mafic recharge priming OIB through time

414   Our findings from historical eruptions at La Palma underscore two key aspects with

415   broader implications for low-flux OIB volcanoes globally: (1) the temporal consistency of

416   geochemical characteristics and magma storage depths across different eruptions, and (2) the

417   pivotal role of mafic recharge in eroding and remobilizing crystal mushes.

418   Cluster analysis reveals six common geochemical groups preserved across all three

419   eruptions, indicating a consistent evolution of magmatic processes over time. This is supported

420   by dominant crystallization trends, formed during recharge, fractionation and ascent, which show

421   remarkably uniform major and trace element systematics. Likewise, magma storage pressures

422   and temperatures remain largely invariant across eruptions (Fig. 10)[11,15]. Overall, these findings

423   align with observations from other low-flux OIB volcanoes, where magma accumulation and

424   differentiation occur predominantly in the upper mantle [48,52–54], underscoring the central role of

425   mantle-seated processes in modulating volcanic activity at OIB.

426   Regarding the role of mafic recharge, we acknowledge its importance in remobilizing

427   deep-seated crystal mushes. Nonetheless, we find little evidence in the tephrite-hosted

428   clinopyroxene cargo that mafic recharge, as represented by Cluster 5, acted as the immediate

429   eruption-driving mechanism during eruptions studied in this work, as these crystals lack Cluster

430   5 signatures in their inner rims, raising questions about the immediate eruption triggering.

431   Volcanic eruptions can be triggered by reservoir failure, which may result from magma pressure

432   build-up (e.g., magma recharge, volatile exsolution) or external factors (e.g., earthquakes, loading

433   or unloading)[1]. For the La Palma eruptions studied here, the recharge magma in early-erupted

434   tephrite-hosted clinopyroxenes is always confined to earlier growth zones (Fig. 9), likely reflecting

435   earlier episodes of recharge that did not immediately trigger the eruptions. Hence, we suggest

436   that these mafic recharge events preserved in the inner portions of the zoning record represent

437   repeated injections of mafic magma in the time preceding the eruptions (Fig. 10A). These

438   repeated mafic inputs played a key role in gradually unlocking and remobilizing the relatively cold,

439   evolved tephritic to phonolitic mush. This is consistent with observations from the 2021 Tajogaite

440   eruption, for which seismicity suggests magma recharge since 2017[36,55], while phase equilibrium

441   experiments and olivine zoning records indicate cooling of the tephrite magma prior to the 2021

442   Tajogaite eruption[12,34]. Thus, while mafic recharge was not the immediate eruption trigger, it

443   played a key role in gradually priming the system, by recycling the resident tephritic to phonolitic

444   crystal mush. Reservoir failure was probably reached because volatile exsolution following

445   magma differentiation led to overpressure[1,26]. Once the eruptions initiated, the tephrite magmas

446   were drained first, which in turn activated the recharge basanite reservoir, supplying fresher mafic

447   basanite magma that dominated the late-erupted products (Fig. 10B). These findings highlight

448   that, in low-flux OIB settings such as La Palma, mafic recharge is a key process in priming the

449   plumbing system, even if it is not the immediate eruption trigger. This slightly deviates from

450   observations at other basaltic volcanoes worldwide, where mafic recharge is often identified as

451   the immediate eruption-triggering mechanism [e.g.7,48,49,56]. From a monitoring perspective, this

452   underscores the importance of recognizing geophysical and geochemical signals of deep

453   recharge (e.g., seismicity, deformation, changes in gas flux) as potential indicators of an eruption

454   priming. Such signals may reflect the progressive destabilization of crystal-rich reservoirs and

455   could provide critical windows for hazard assessment and early warning in similar intraplate

456   volcanic systems.

457

458

Conclusions

We have explored the temporal evolution of magmatic processes under La Palma by targeting the zoning record of clinopyroxene crystals from the 1712 El Charco, 1971 Teneguía and 2021 Tajogaite eruptions, together with their carrier melts. By combining textural, geochemical, barometric and clustering constraints, we propose that the magma dynamics and storage conditions beneath La Palma have remained broadly consistent through historical time. Tephrite-basanite magmas are predominantly stored in deep, likely vertically extended, upper mantle reservoirs between ~18–25 km depth, with primitive clinopyroxene cores possibly crystallizing deeper and evolved phonolite mushes crystallising in cooled reservoirs after >80% fractional crystallization of basanite melts (Fig. 10). Mafic basanite melts, preserved in Cr-rich clinopyroxene inner rims, repeatedly recharged the La Palma plumbing system, eroding and disaggregating resident tephritic to phonolitic mushes. Following recharge, the basanite magma undergoes ~10-20% fractional crystallization, producing eruptible tephritic magmas. Hence, mafic recharge is a vital mechanism to unlock and remobilize mush systems and therefore represents a key eruption primer. In terms of the immediate eruption trigger, La Palma historical eruptions suggest initiation by the internal evolution of the tephrite reservoir (e.g. volatile exsolution), as early-erupted clinopyroxene inner rims shows no clear evidence of mafic recharge, as represented by Cluster 5, immediately preceding the eruptions.

Methods

Sampling and electron microprobe (EMPA)

Samples from the 1712 El Charco, 1971 Teneguía and 2021 Tajogaite eruptions consist of fresh lavas that transition from tephrites to basanites throughout the eruption (Fig. 1 and

482   Supplementary Material). Samples from Tajogaite 2021 correspond to the same sample set

483   published in Ubide et al. (2023)[17] (Supplementary Data Table 1, SDT1).

484   Clinopyroxene crystals from the different eruptions were analysed using three different

485   electron microprobe analysers (EMPA). Data are reported in Supplementary Data Table 2

486   (SDT2). Tajogaite 2021 crystals were analysed at the Centro Nacional de Microscopía Electrónica

487   of the Complutense University in Madrid, Spain, using a JEOL JXA-8900M electron microprobe

488   equipped with four wavelength-dispersive spectrometers (WDS). Measurements were conducted

489   using a beam current of 20 nA, an accelerating voltage of 15 kV and a beam diameter of 5 μm.

490   Elemental counting times were 10 s on the peak and 5 s on background positions. Calibration

491   standards included: albite for Na and Si; sillimanite for Al; microcline for K; almandine for Fe and

492   Mn; kaersutite for Mg, Ca, and Ti; fluor-apatite for P, F, and Cl; and pure metal elements for Ni

493   and Cr. Data were corrected using the ZAF matrix correction procedure. The analyses were

494   conducted in 2021 and 2022, following the same procedure as described in Ubide et al. (2023),

495   as the clinopyroxene data presented here were acquired during the same analytical sessions.

496   These new EMPA data presented in this work complement the Ubide et al. (2023)[17] dataset by

497   adding crystal core and outer rim compositions to the previously reported crystal inner rim and

498   microlite analyses.

499   El Charco 1712 crystals were analysed at the Unidad de Microscopía Electrónica of the

500   University of Huelva, Spain, using a JEOL JXA-8200 electron microprobe, equipped with four

501   WDS and one energy-dispersive X-ray spectrometer (EDS). Measurements were conducted

502   using a beam current of 20 nA, an accelerating voltage of 15 kV and a beam diameter of 5 μm.

503   Elemental counting times were set at 10 seconds on peak and 5 seconds on background for each

504   element. Calibration standards included: K-feldspar for Al, Na, and K; wollastonite for Ca and Si;

505   fayalite for Fe; forsterite for Mg; manganosite for Mn; chromite for Cr; rutile for Ti. Data were

506   corrected using the ZAF matrix correction procedure.

507   Teneguía 1971 crystals were analysed at the Centro Nacional de Microscopía Electrónica

508   of the Complutense University in Madrid, Spain, using a new JEOL Field Emission Gun (FEG)

509   JXA-iHP200F electron microprobe, equipped with four WDS. Measurements were conducted

510   using a beam current of 10 nA, an accelerating voltage of 15 kV and a beam diameter of 5 μm or

511   a focused beam. Elemental counting times were 10s on the peak and 5s on background positions.

512   Calibration standards and data correction procedure are the same as for the JEOL JXA-8900M

513   microprobe described above.

514   To assess data consistency across three microprobe instruments, we re-analyzed

515   selected clinopyroxene crystals of the 1712 (30 analyses) and 2021 (38 analyses) samples using

516   the new JEOL JXA iHP200F electron microprobe at the Centro Nacional de Microscopía

517   Electrónica (Madrid). Re-analyses were conducted at the same locations as the original analyses.

518   Overall, the new data are consistent with the original measurements within analytical uncertainty

519   (based on Poisson statistics), confirming the robustness and inter-instrument reproducibility of the

520   dataset (Fig. S1-S2). Minor offsets observed in some analyses likely reflect minor positional

521   offsets or patchy crystal domains. Data quality was monitored by analyzing clinopyroxene

522   secondary standards from the Smithsonian Institution of Washington (Kakanui augite NMNH

523   122142, Cr-augite NMNH 164905 and Diopside NMNH 117733). Accuracy and precision

524   determined using the Cr-augite standard NMNH 164905, which closely matches the composition

525   of our samples, are better than 1–6% and 1–3% for major elements, respectively. For minor

526   elements, accuracy ranges from 2–7% and precision from 1–8%, except for Mn, which exceeds

527   10%. Data of secondary standards are reported in Supplementary Data Table 3 (SDT3).

Laser Ablation-Inductively Coupled Plasma Mass Spectrometry (LA-ICP-MS)

LA-ICP-MS was used to determine trace element compositions of clinopyroxene crystals via single-spot analyses (following Petrelli et al. (2016)[57] (Supplementary Data Table 4, SDT4), to acquire quantitative trace element maps of clinopyroxene (following Ágreda-López et al. 2025[58]) (Zenodo repository 10.5281/zenodo.17635257) and to measure major and trace element compositions of the microcrystalline matrix (following the rastering method of Ubide et al. 2023[17]) (Supplementary Data Table 6, SDT6). LA-ICP-MS analyses were done at the Dipartimento di Fisica e Geologia, University of Perugia, using a 193 nm Analyte G2 laser ablation system operated with Chromium software coupled to a quadrupole iCAP-Q ICP-MS (Thermo Fisher Scientific) operated with Qtegra software. For all analyses, helium carrier gas was set to 0.6 and 0.3 L min⁻¹ for the ablation cell and cup, respectively.

Matrix compositions were analysed following the method described in Ubide et al. (2023)[17], consisting in laser rastering over equigranular microcrystalline areas via overlapping spots. In total, 10 rasters were acquired per thin section across four thin sections (two basanite and two tephrite samples) from the El Charco 1712 and Teneguía 1971 eruptions. These data are complemented by published matrix analyses from Tajogaite 2021[17], to which the reader can refer for full details on analytical conditions and matrix data reduction, which uses BCR-2G glass reference material as external standard and normalisation to total 100wt.% oxides as internal standard. For major elements, accuracy and precision were assesed using glass reference materials BHVO-2G and GSD-1G, resulting mostly in values <5% and always better than 8% (Supplementary Data

551   Table 7, SDT7). For trace elements, accuracy was monitored using glass reference

552   materials BHVO-2G, GSD-1G, NIST-610 and NIST-612 (Supplementary Data Table 8,

553   SDT8). Accuracy for BHVO-2G and GSD-1G is within 5–10% relative to accepted values,

554   except for Ta which was ~13%. Precision is always <3% for both major and trace

555   elements (SDT7-8).

556   Trace element composition of clinopyroxene single-spots were acquired using a

557   spot size of 30 μm and repetition rate of 10 Hz[57]. Data reduction was performed using

558   Iolite[59], using a 3D trace element calibration including NIST-SRM610, NIST-SRM612,

559   GSD-1G and BHVO-2G as the calibrators, Ca as measured by EMPA as the internal

560   standard, and USGS-BCR2G as the quality control. This configuration ensured precision

561   and accuracy within ±5% for most analysed trace elements, with all elements exhibiting

562   accuracy better than ±10% (Supplementary Data Table 5, SDT5).

563   Compositional maps of clinopyroxene were acquired using oversampling, by

564   overlapping laser squares to generate subsequent ablation lines that build the mapped

565   area[58]. We used a spot size of 10 μm, resulting in a resolution of 5 μm[58]. Dosage was set

566   at 10, Scan speed at 100 μm/s, and the repetition rate at 100 Hz. We analysed 10

567   elements (Ca, Sc, Ti, V, Cr, Mn, Ni, Sr, Zr, Ce). NIST-SRM610 was used as a calibration

568   standard and Ca was used as internal standard. Measurements of the secondary

569   standard USGS-BCR2G alongside the unknown maps yielded accuracies better than

570   10% relative to preferred values for all elements, except Sc, which was within 15%.

571   Precision was better than 10% relative standard deviation, with most elements showing

572   precision between 0% and 5% (Supplementary Data Table 5, SDT5). Clinopyroxene

573   maps can be found in the Zenodo repository at this link: 10.5281/zenodo.17635257.

574   Data processing and image reconstruction of chemical maps were performed

575   using HDIP software (Teledyne Photon Machines). HDIP was used to align and calibrate

576   raw LA-ICP-MS signal intensities, reconstruct the spatial distribution of each element, and

577   export fully calibrated concentration matrices (in ppm) of clinopyroxene crystals. This was

578   done by manually segmenting clinopyroxene crystals within each map and removing the

579   surrounding microcrystalline groundmass, mineral oxides, mineral inclusions, large

580   cracks, and voids. Additionally, we retained only data between the 1st and 99th percentile

581   to eliminate outlier spikes. Clinopyroxene matrices were subsequently processed and

582   visualized using a Python script designed to apply one of three alternative scaling

583   approaches, logarithmic scaling, histogram equalization (HE), or adaptive histogram

584   equalization (AHE), to enhance chemical contrast, depending on the statistical distribution

585   and dynamic range of each element. Logarithmic transformation was applied when

586   elemental concentrations spanned several orders of magnitude, helping to highlight

587   subtle variation in low-concentration domains that would otherwise be suppressed by

588   linear rescaling. Histogram equalization, a global contrast enhancement technique, was

589   applied to datasets with moderate skew to redistribute pixel intensities and make use of

590   the full dynamic range of the display. For highly skewed or spatially heterogeneous data,

591   adaptive histogram equalization was employed. Unlike the HE method, AHE operates on

592   small image regions to enhance local contrast and resolve fine-scale compositional

593   structures. The most appropriate visualization method was automatically selected for

594   each element by comparing visual contrast and feature detectability.

595

596

Clustering

Clustering is an unsupervised machine-learning technique used to partition complex, high-dimensional datasets into groups ("clusters") based on similarity in their multivariate features [e.g. 58,60,61]. This approach can identify similar chemical features by grouping together data that exhibit comparable elemental compositions. This can reveal patterns in large geochemical datasets that may correspond to distinct crystal zones, growth stages, or textural domains, without prior labels, and then facilitating the subsequent petrologic interpretation [62]. Here, we applied clustering to the trace element clinopyroxene dataset (Sc, Ti, V, Cr, Mn, Ni, Sr, and Zr) from the three studied eruptions, which included both single-spot analyses (n=318) and quantified pixels from compositional maps (n=398776), using the k-means algorithm implemented in Python 3.

Thermobarometry

Magma storage pressures were estimated using clinopyroxene-melt barometers following guidelines for clinopyroxene-melt equilibrium and selection of calibrations provided by MacDonald et al. (2023)[63], who found that thermobarometers calibrated on isothermal–isobaric experimental datasets[8,28] yield greater accuracy under low undercooling conditions, whereas those incorporating decompression and undercooling experiments[27] perform better at higher degrees of undercooling. Low undercooling is typically associated with the formation of crystal cores and sector zoned compositions, while high undercooling occurs during magma decompression and degassing, promoting the crystallization of crystal rims and microlites[63]. Hence, we used the barometer from Putirka et al. (2003)[28] (SEE= ± 1.7 kbar, 5.6 km) coupled with the thermometer from Putirka (2008)[8] (Eq. 33, SEE= ±45 °C) for clinopyroxene cores and inner rim

620 compositions, whereas for clinopyroxene outer rims and microlites we used the

621 thermobarometer by Mollo et al. (2018)[27] (SEE= ± 1.5 kbar, 4.9 km and ± 28 °C). These

622 thermobarometers are calibrated for mafic alkaline magmas. For evolved clinopyroxene

623 core compositions, here defined as cores with Mg#<67, we employed a thermobarometer

624 specific for differentiated alkaline magmas by Masotta et al. (2013)[64] (SEE= ± 1.15 kbar,

625 ± 3.8 km and ± 18.2 °C).

626 We applied an eruption-specific clinopyroxene–melt matching approach, pairing

627 clinopyroxene compositions with melt compositions from the same eruption. We used

628 clinopyroxene and melt compositions from this study (SDT2 and SDT6) and from the

629 literature (Supplementary Data Table 9 and 10, SDT9-SDT10). For Tajogaite 2021, we

630 used 422 clinopyroxene compositions from this study and 904 from the literature[17,19]. Melt

631 compositions for Tajogaite 2021 included groundmass and tephra glass (n = 708),

632 microcrystalline groundmass or matrix (n = 176), and melt inclusions (MI, n = 72) from the

633 literature[13,17,65,66]. For the 1971 Teneguía eruption, clinopyroxene compositions come

634 exclusively from this study (n = 164). Published data from Teneguía 1971[11,38] were not

635 included as they show systematically lower CaO and higher Na_2O contents compared to

636 published data (Fig. S8). Melt compositions comprised matrix glass data from this study

637 (n = 40) and one glass composition from the literature [37]. For the El Charco 1712 eruption,

638 we used 213 clinopyroxene compositions from this study. Melt compositions included

639 matrix glass (n = 40) from this study and one published glass analysis[37]. Evolved

640 clinopyroxene core compositions were paired with one titanite-hosted, tephriphonolite

641 melt pocket composition found in a plagioclase macrocryst from the 2021 Tajogaite

642 eruption[14]. To increase the number of equilibrium pairs for evolved clinopyroxene cores,

643 we performed a Monte Carlo simulation, varying the starting melt pocket composition by

644 ±5%, generating 1000 compositions to capture analytical variability. Equilibrium between

645 clinopyroxene and putative melts was evaluated by selecting clinopyroxene–melt pairs

646 that met four criteria based on the agreement between measured and predicted

647 components: DiHd (diopside + hedenbergite) within ±10%, EnFs (enstatite + ferrosilite)

648 within ±5%, CaTs (calcium–tschermak component) within 6%, and CaTi (calcium–

649 titanium component) within ±2% [63]. Melt H_2O concentration was set at 1 wt% for the

650 tephrite-basanite magma, as suggested for the 2021 Tajogaite primitive magma[34], and to

651 3 wt% for evolved core compositions[15]. However, we note that H_2O has little effect on

652 thermobarometry calculations[15,17]. All calculations were performed with the Thermobar

653 Phyton tool [67].

654 Throughout this work, we base our conclusions on thermobarometry calculations

655 obtained following guidelines from MacDonald et al. (2023) [63], as their equilibrium criteria

656 improve precision of pressure and temperature estimates of sector zoned clinopyroxene

657 compositions. However, to increase the number of clinopyroxene–melt equilibrium pairs

658 and evaluate different thermobarometric calibrations[8,27,28,31], we applied alternative

659 thermobarometric approaches using a more relaxed set of equilibrium criteria (Fig. S4-

660 S5). These required differences between measured and predicted clinopyroxene

661 components to be within 12% for DiHd, 10% for EnFs, and 6% for CaTs, within 2σ of the

662 thresholds proposed by Neave et al. (2019)[68], and a $(K_D(Fe–Mg)_{cpx–melt})$ of 0.28 ± 0.08 [8].

663 Overall, this alternative approach yields a larger number of clinopyroxene–melt

664 equilibrium pairs and results comparable to those obtained using the MacDonald et al.

665 (2023) [63] guidelines (Fig. S4-S5).

Figures
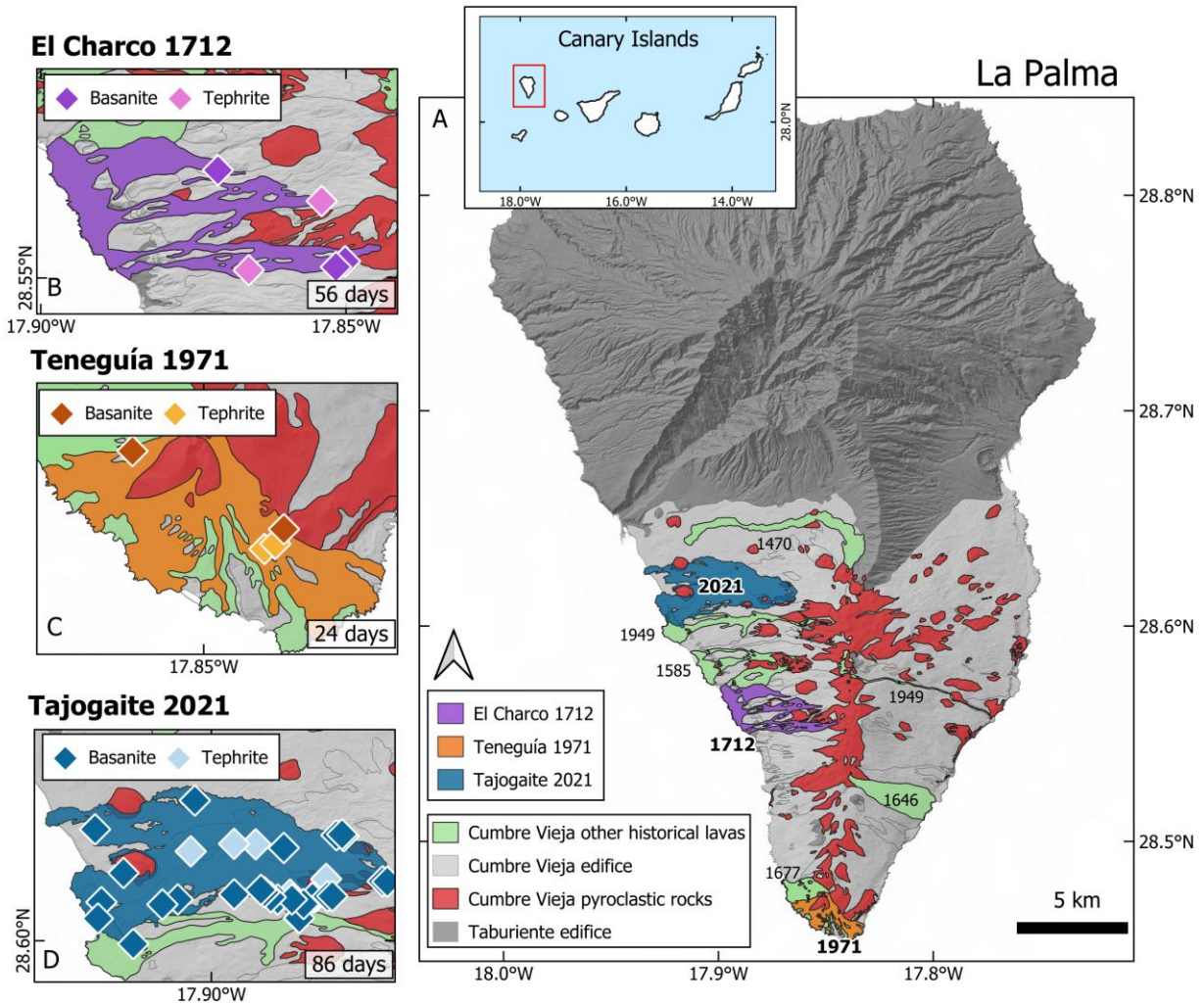
Fig. 1 Geological map of La Palma and sample localities of studied eruptions. (A) simplified geological map of La Palma island, with inset showing the location of the island in the Canaries. The Cumbre Vieja edifice shows historical eruptions occurred since the 15th century. (B-D) Zoom of historical eruptions studied in this work and sample localities of (B) El Charco 1712, (C) Teneguía 1971 (D) Tajogaite 2021 eruptions. Sample location is indicated by coloured diamonds, distinguishing between amphibole-bearing tephrite and olivine-bearing basanite samples. The

674   duration of each eruption is shown in the bottom right corner. Geological data are from the

675   Cartográfica de Canarias (https://www.grafcan.es/).

676

677
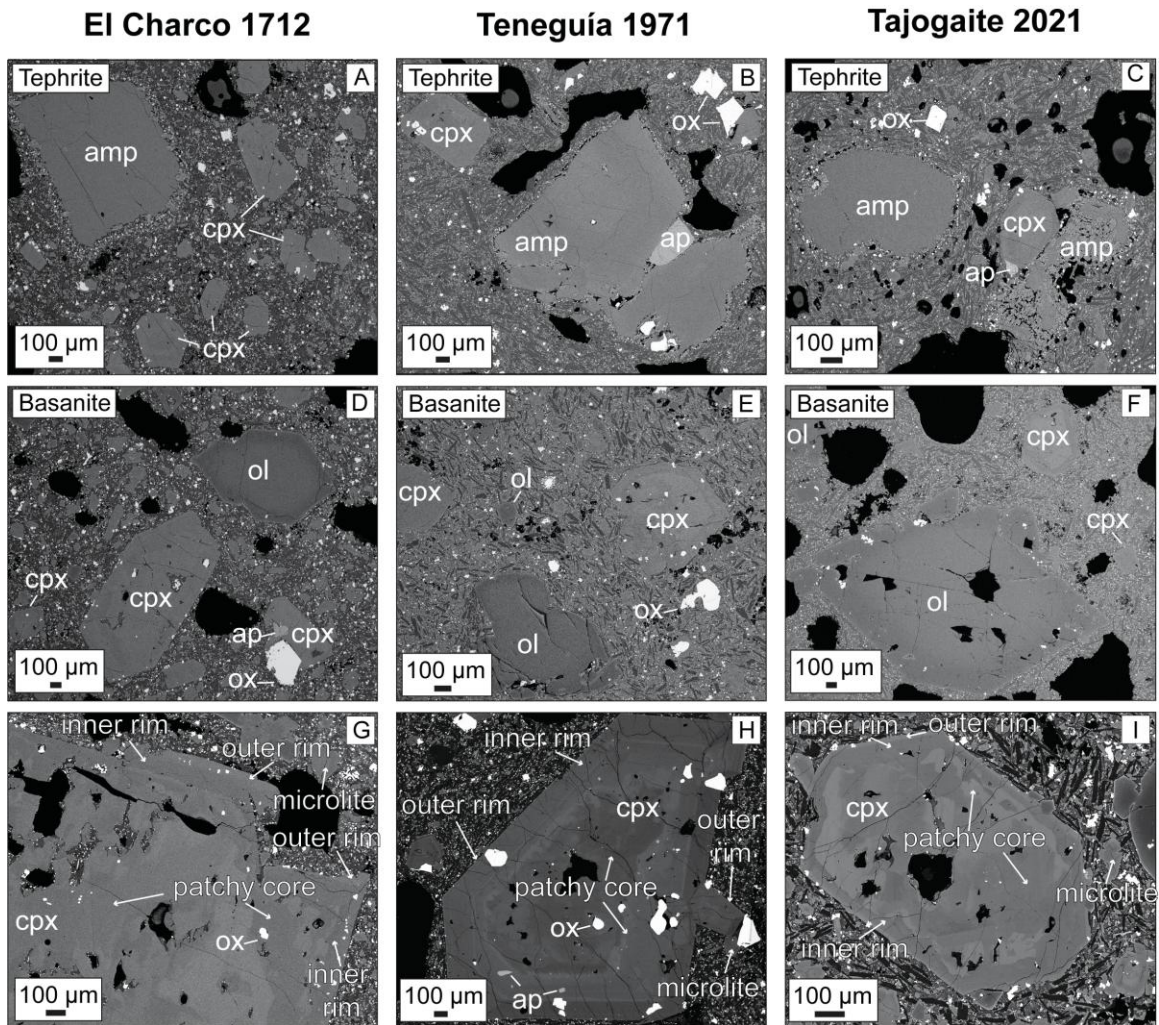
Fig. 2. Petrographic features of tephrite and basanite samples from the three eruptions studied in this work in backscattered electron images (BSE). (A-C) Representative BSE images of tephrite samples, showing a mineral assemblage characterized by crystals of clinopyroxene and amphibole. (D-F) Representative BSE images of basanite samples, showing a mineral assemblage dominated by crystals of clinopyroxene and olivine. (G-I) BSE images of clinopyroxene crystals, highlighting mineral zoning and different textural positions studied in this work. cpx: clinopyroxene; ol: olivine; amp: amphibole; ox: oxide; ap: apatite.

685
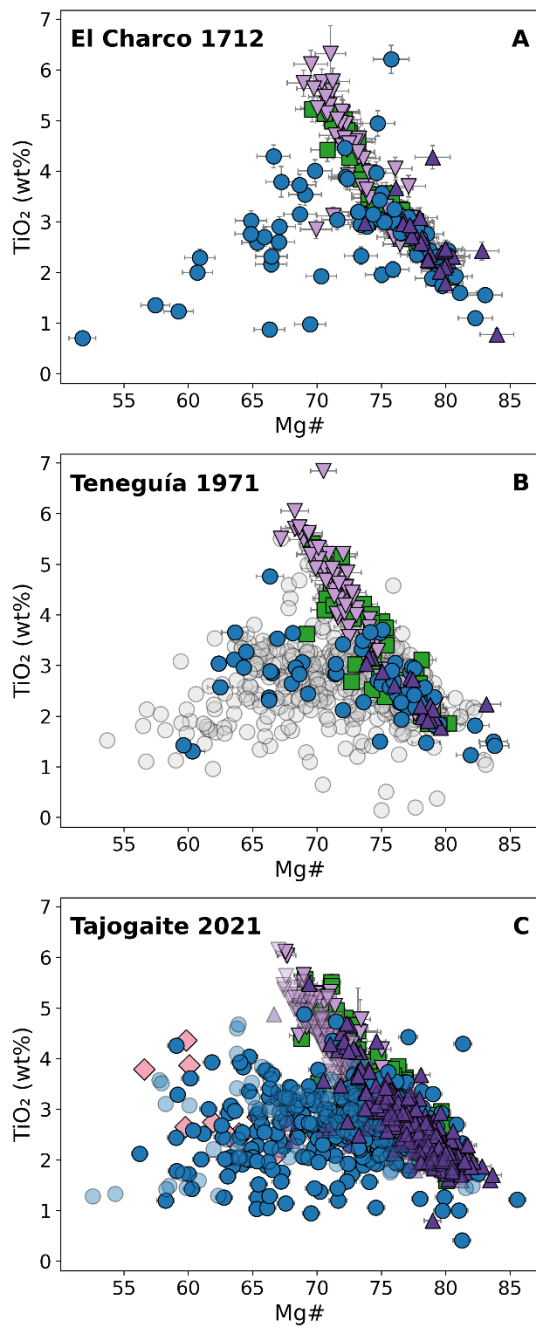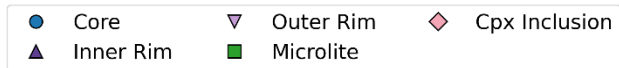
Fig. 3. Major element compositions of clinopyroxene crystals showing variation in Mg# as a

function of TiO$_2$ for samples from (A) El Charco 1712 (B) Teneguía 1971, and (C) Tajogaite 2021.

Data are categorized by textural position: core, inner rim, outer rim, microlite, and clinopyroxene

inclusions. Literature data for Teneguía 1971[11,38] are not grouped into textures and are plotted as

faded filled grey circles. For Tajogaite 2021, literature data[19] are shown with faded colours according to textural positions. Inner rim and microlite compositions from the 2021 Tajogaite eruption[17] are here plotted using the same colour scheme as our dataset, as they were collected from the same crystals and complement our study. Error bars indicate 1σ uncertainties derived from EMPA counting statistics.
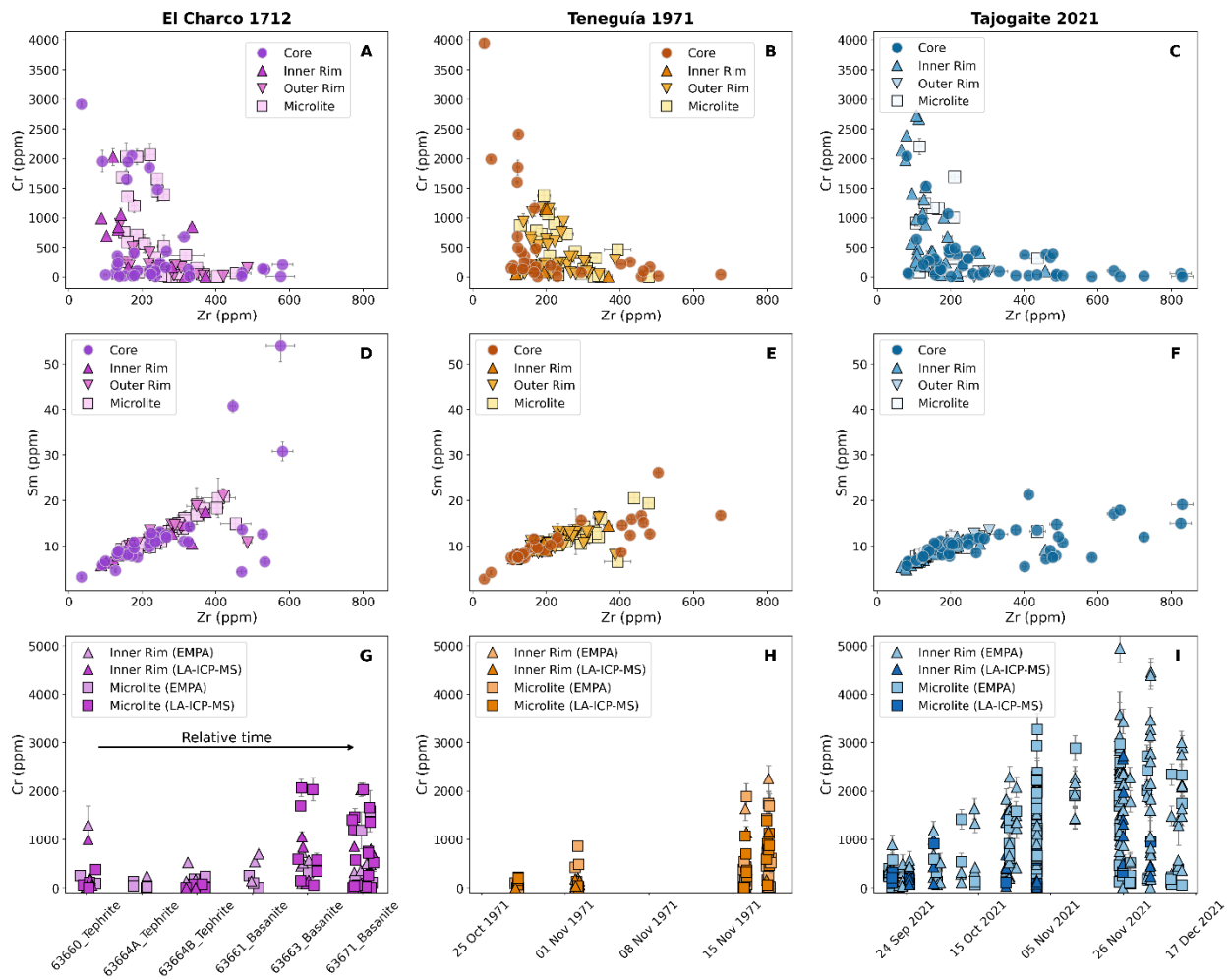
Fig. 4. Trace element characteristics of different clinopyroxene textural positions, showing the LA-ICP-MS concentration of (A–C) Cr and (D-F) Sm in the different eruptions. Symbols and colours represent different textural positions. (G-I) Temporal variation of Cr concentration in inner rim and microlite compositions measured using both EMPA and LA-ICP-MS. For El Charco 1712, samples

701   are ordered from early-erupted tephrite to late-erupted basanite to provide temporal context. For

702   Teneguía 1971 and Tajogaite 2021, samples are plotted according to eruption age. LA-ICP-MS

703   error bars indicate the internal 2SE analytical uncertainty, whereas EMPA error bars reflect 1σ

704   analytical uncertainty based on counting statistics.
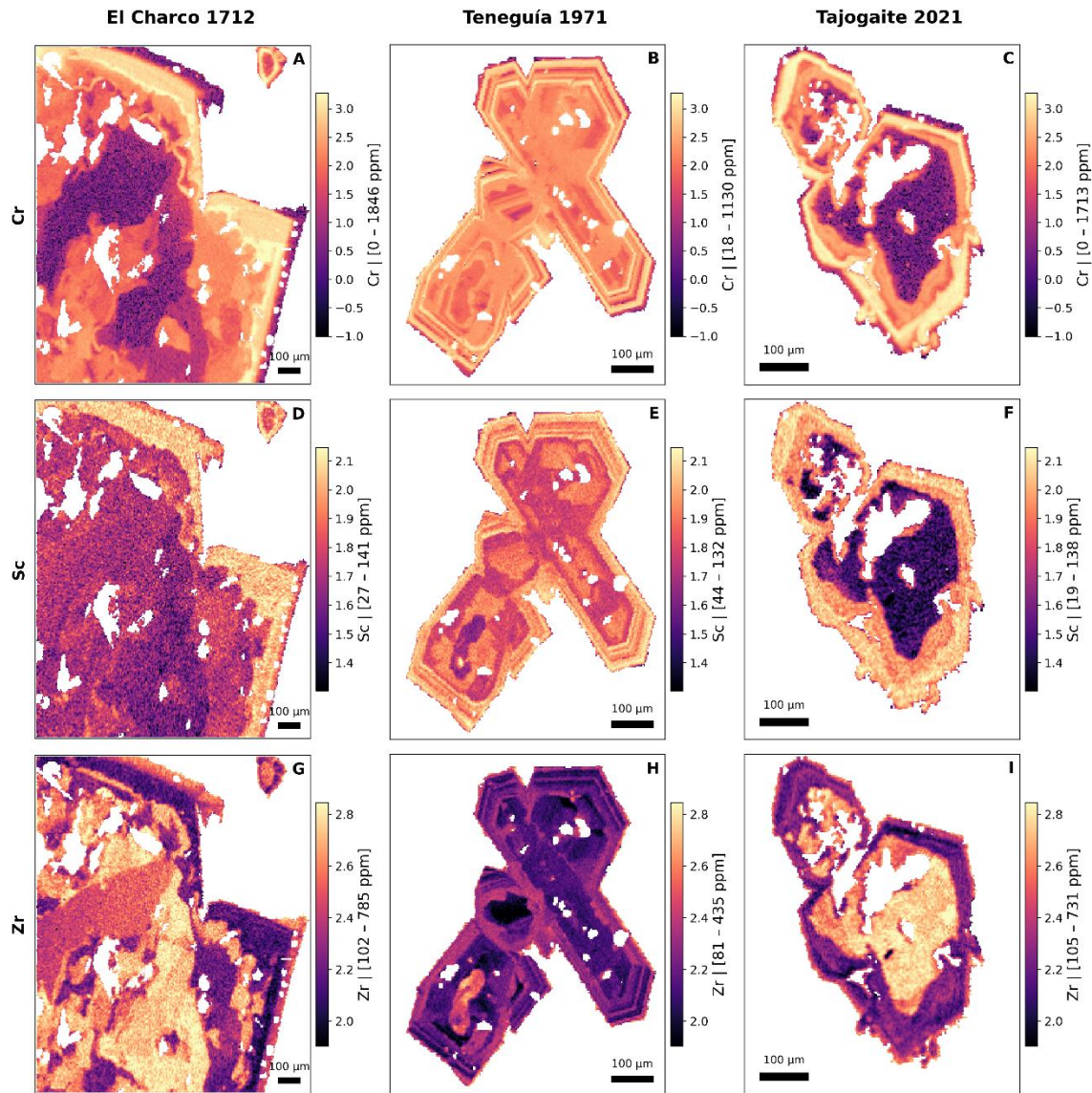
705

706   **Fig. 5.** Trace element maps of representative basanite-hosted clinopyroxene crystals from each

707   eruption, El Charco 1712, Teneguía 1971, and Tajogaite 2021, showing the spatial distribution

708   of Cr (A–C), Sc (D–F), and Zr (G–I) concentrations. Maps are visualized using a logarithmic

709   scale and scaled to the maximum common range of Cr (0.1–6000 ppm; $\log_{10}$ = -1–3.3), Sc (20–

710 140 ppm; $\log_{10}$ = 1.3–2.15) and Zr (80–700 ppm; $\log_{10}$ = 1.9–2.85) observed across the three

711 maps to allow direct comparison of variations among samples and eruptions. Colour bars

712 specify the element and the corresponding concentration range in ppm for each sample.
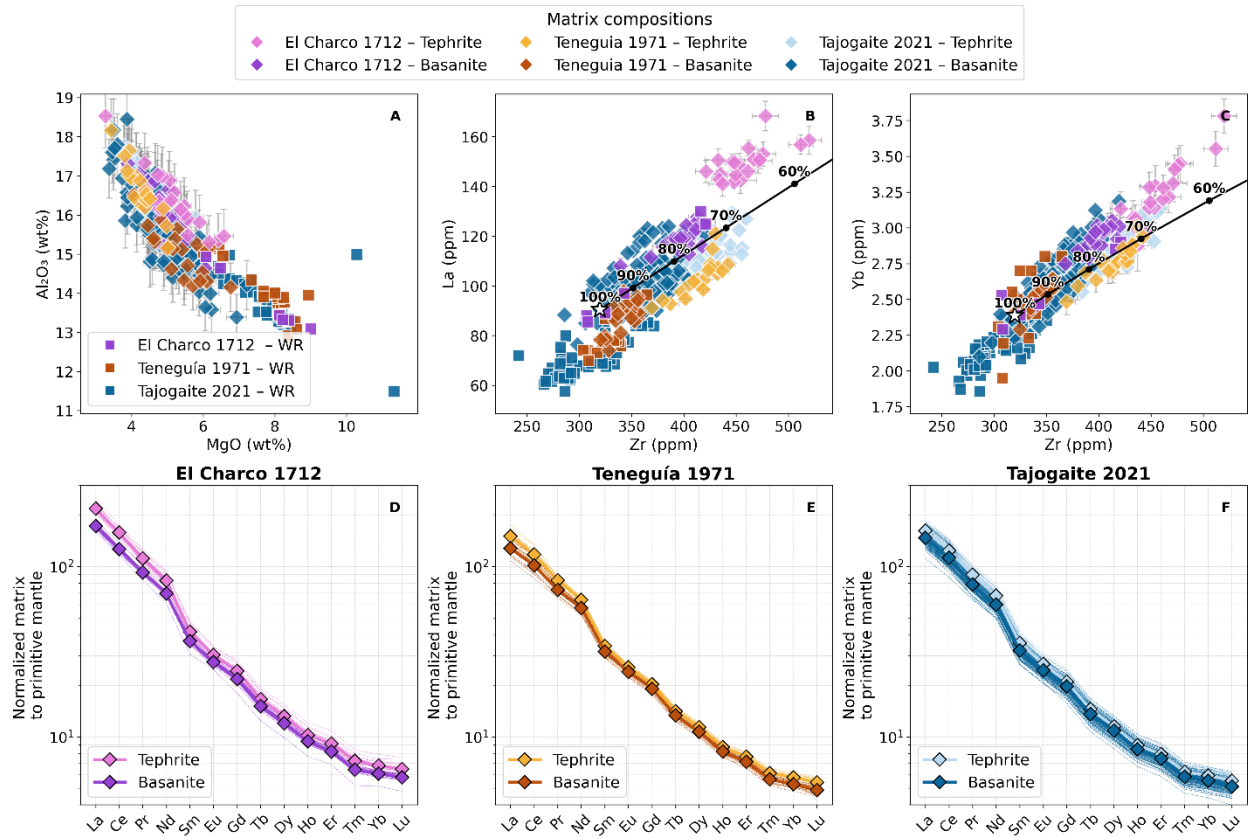
713

714 **Fig. 6.** Major and trace element composition of the microcrystalline matrix. (A) Variation of MgO

715 vs Al_2O_3. (B) Variation of Zr vs La and (C) Zr vs Yb concentrations. Our data are compared to

716 recent whole-rock (WR) major and trace element data from the literature published after 2000 for

717 El Charco 1712[44,69], Teneguía 1971[11,38,44,69] and Tajogaite 2021[17,66,70]. The black line in B and C

718 shows a fractional crystallization model at 10% increments, starting from a primitive matrix

719 composition (white star). See Supplementary Material for modelling details. (D-F) REE patterns

720 of matrix composition, normalized to the composition of primitive mantle[71]. Symbols are color-

721 coded according to tephrite and basanite samples. For major elements, error bars represent 2σ
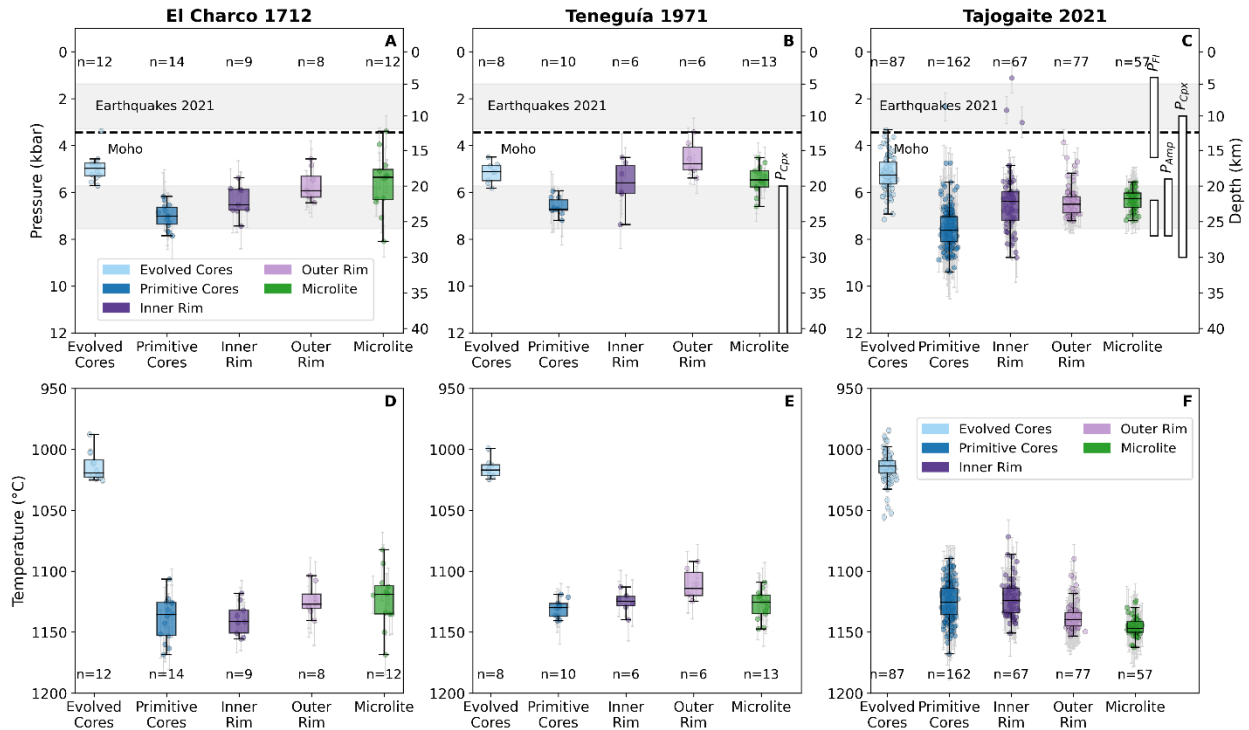
Fig. 7. Thermoobarometry results. (A-C) Barometry and (D-F) thermometry results for the different eruptions illustrated as box plots. Data are grouped in boxplots and color-coded according to individual textural positions. The box represents the interquartile range (25th to 75th percentile), the horizontal line indicates the median, and the whiskers extend to the most extreme data points within 1.5 times the interquartile range from the lower and upper quartiles. Individual estimates are shown as circles, with error bars representing the standard deviation of the estimate at the 1σ level. The number of estimates that pass the equilibrium criteria (see Supplementary Materials) is indicated for each textural category. Calculations include clinopyroxene and melt compositions from this study and from the literature[13,14,17,19,37,65,66]. Gray fields in A-C panels indicate the location of seismicity during the 2021 Tajogaite eruption[25]. White rectangles indicate literature pressure ranges based on cpx (P_{Cpx}), amphibole (P_{Amp}) and fluid inclusions (P_{FI}).

736 Pressures were converted into depths using a crustal density of 2800 kg/m^3 and 3100 kg/m^3 above

737 and below the Moho, respectively[24,72].
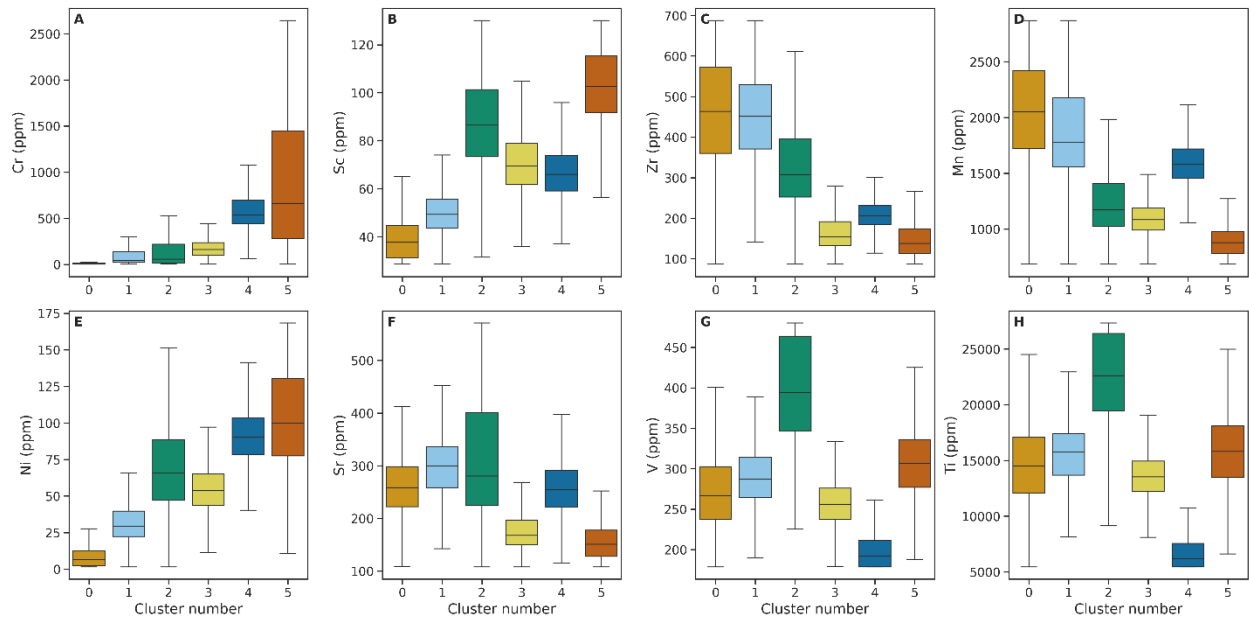
738

739 **Fig. 8**. Boxplots showing the clustering results for Cr, Sc, Zr, Mn, Ni, Sr, V and Ti. The boxes

740 represent the interquartile range (25th–75th percentile), the horizontal line indicates the median,

741 and the whiskers extend to the most extreme data points within 1.5 times the interquartile range

742 from the lower and upper quartiles. For clustering, we merged pixel-level concentrations (in ppm)

743 from the chemical maps with single-spot data and considered data between 0.1st and 99.9th

744 percentiles to avoid outliers. We tested 2 to 10 cluster grouping and selected six, as this

745 configuration best captured the main textural and chemical features without unnecessary

746 complexity (Fig. S3).

747
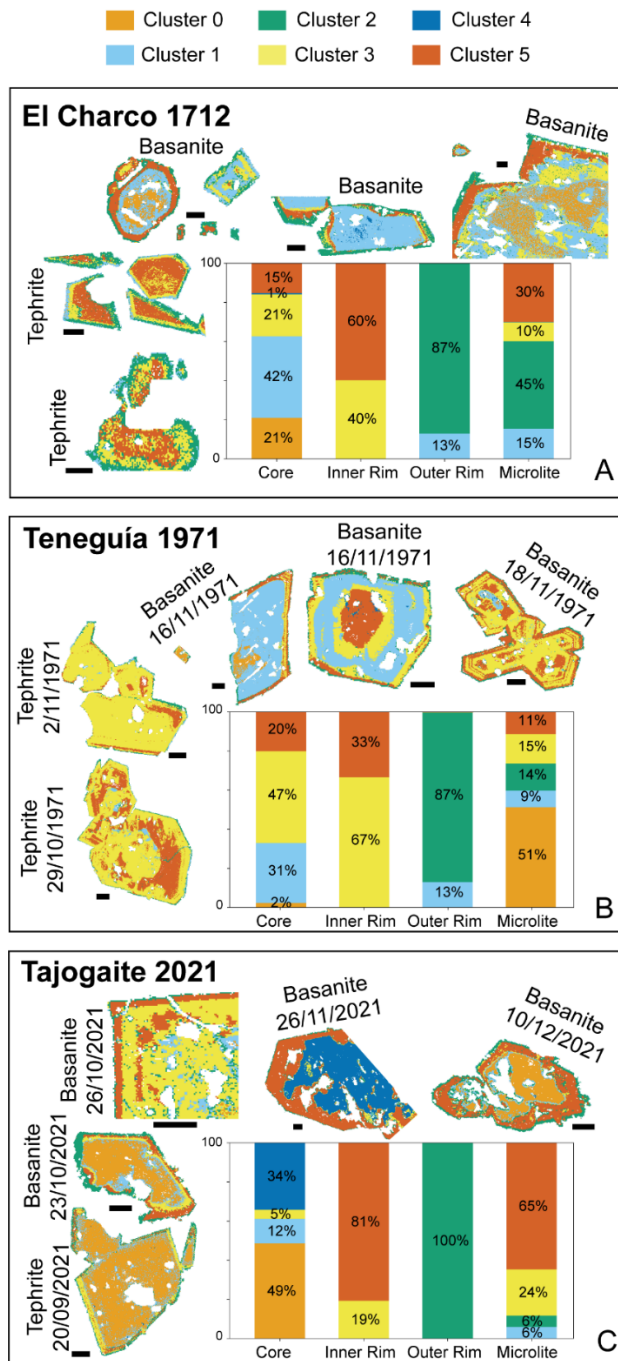
Fig. 9. Summary and visualization of the clustering results for A) El Charco 1712, B) Teneguía 1971, and C) Tajogaite 2021. Each panel includes: (1) cluster-coloured maps of clinopyroxenes, indicating whether they are hosted in tephrite or basanite samples and, where applicable, the eruption date. The black bar in each map indicates a scale bar of 100 µm; (2) stacked bar displaying, for each textural position, the proportions of the different clusters.
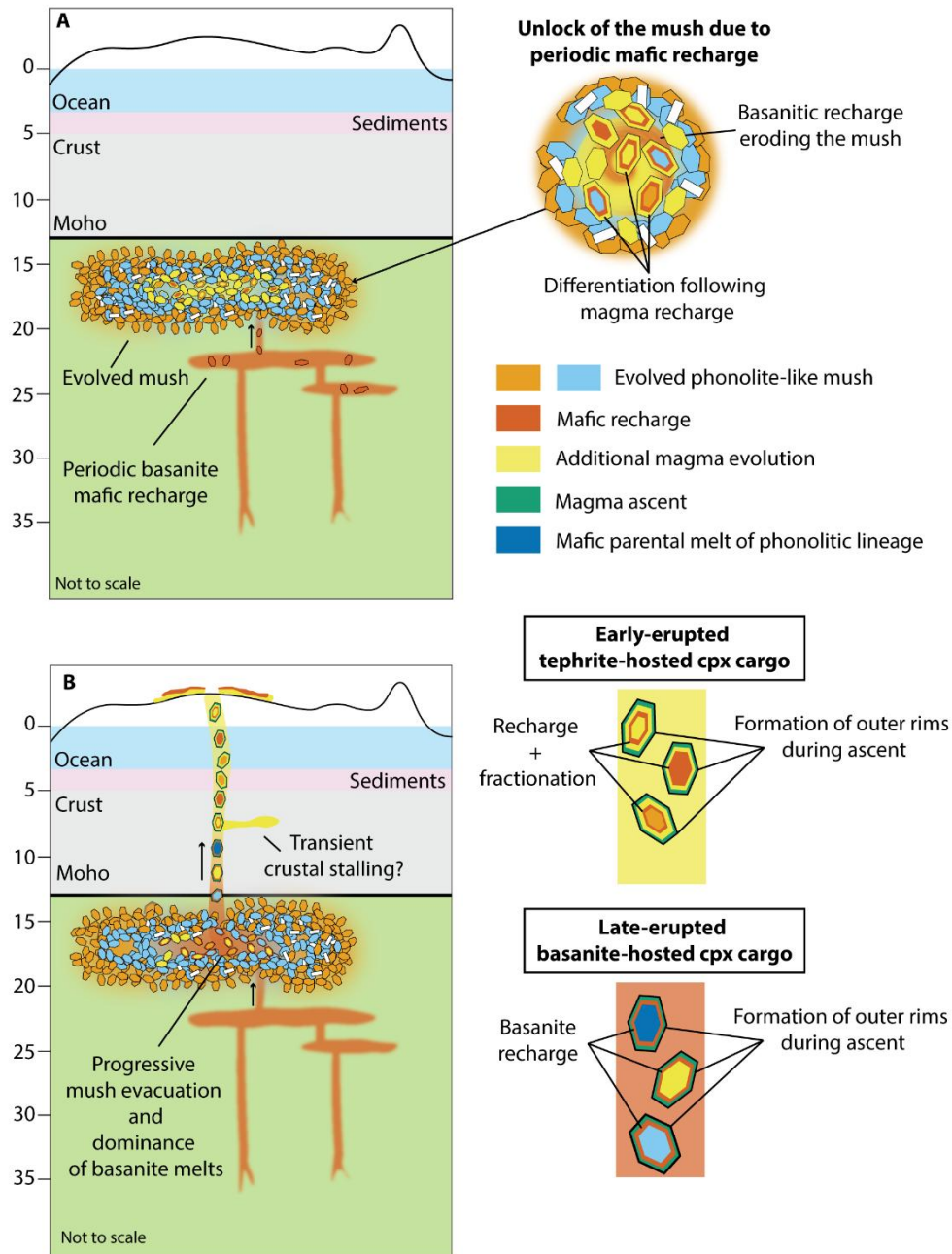
Fig. 10. Conceptual cartoon summarizing the main findings of this study. (A) Schematic illustration of the magmatic plumbing system beneath La Palma prior to El Charco 1712, Teneguía 1971 and Tajogaite 2021 eruptions. Basanite melts periodically recharge a tephritic to phonolitic (Cluster 0 and 1) crystal mush reservoir in the upper mantle, leading to partial remobilization and disaggregation of the resident antecrystic mush. Fractionation of the basanite melt following recharge produces eruptible tephrite magma. This recharge–

760   disaggregation–fractionation process creates specific zoning patterns reflected in the early-

761   erupted clinopyroxene record, characterized by tephritic inner rims (Cluster 3) preceded by

762   basanite compositions (Cluster 5) (B) Eruptions are likely triggered by internal evolution of the

763   tephrite reservoir following fractionation of the basanite magma. Once the tephrite magma is

764   exhausted, more primitive basanite magma is drained, carrying a crystal cargo dominated by

765   clinopyroxene crystals with basanite recharge (Cluster 5) inner rims and antecrystic cores. During

766   ascent and/or surface cooling, outer rims (Cluster 2) crystallize. Evidence for lower crustal stalling,

767   as proposed by geophysical[25], melt and fluid inclusions[33,40] and experimental studies[34,35], is not

768   recorded in our petrological record, implying it may represent a transient storage level.

769

Acknowledgements

784 archive from the Universidad Complutense de Madrid hosting the samples from the 1971

785 Teneguía and 1712 El Charco eruptions. We thank analytical support from Alfredo Larios and

786 Maider Virumbrales (UCM, Madrid) at Centro Nacional de Microscopía Electrónica at Universidad

787 Complutense de Madrid.

788

Author contributions

790 AC, TU, and MP developed the study conceptualization. AC wrote the first draft and prepared all

791 figures, with input and editing from all authors. Fieldwork was conducted by AM, MP, RH, MJH,

792 EA, NC, and JJCB. Funding acquisition was led by MP and AM. Investigation and laboratory work

793 were carried out by MP, AC, RH, MAL, MJH, DGG, AM, EA, and NC. All authors contributed to

794 writing and editing the manuscript.

795

Competing interests

797 The authors declare no competing interests

Data Availability

799 All data included in this article are included in Supplementary Data Tables (SDTs) in the

800 online version of the article. Additionally, data are available in the repository Zenodo at

801 the link: https://doi.org/10.5281/zenodo.17635257. Samples from the 2021 Tajogaite,

802 1971 Teneguía and 1712 El Charco eruptions are curated at Litoteca de Petrologia at

803 UCM and are available for sharing and collaborations upon request to Dr. A. Márquez

804

References

1. Caricchi, L., Townsend, M., Rivalta, E. & Namiki, A. The build-up and triggers of volcanic eruptions. *Nat Rev Earth Environ* **2**, 458–476 (2021).

2. Ubide, T., Neave, D. A., Petrelli, M. & Longpré, M. A. Crystal Archives of Magmatic Processes. *Front Earth Sci (Lausanne)* **9**, 1–7 (2021).

3. Caracciolo, A. *et al*. Magma plumbing systems and timescale of magmatic processes during historical magmatism on Reykjanes Peninsula. *Earth Planet Sci Lett* **621**, 118378 (2023).

4. Caracciolo, A. *et al*. Mush disaggregation and dike propagation timescales at active volcanoes – Evidence from the 2022-2023 Fagradalsfjall eruptions. *Journal of Petrology* https://doi.org/10.1093/petrology/egaf054 (2025) doi:10.1093/petrology/egaf054.

5. Gao, R., Lassiter, J. C., Clague, D. A. & Bohrson, W. A. Evolution of Hawaiian Volcano Magmatic Plumbing System and Implications for Melt/Edifice and Melt/Lithosphere Interaction: Constraints from Huallai Xenoliths. *Journal of Petrology* **63**, (2022).

6. Pietruszka, A. J., Marske, J. P., Heaton, D. E., Garcia, M. O. & Rhodes, J. M. An isotopic perspective into the magmatic evolution and architecture of the rift zones of kilauea volcano. *Journal of Petrology* **59**, 2311–2352 (2018).

7. Ubide, T. & Kamber, B. S. Volcanic crystals as time capsules of eruption history. *Nat Commun* **9**, 326 (2018).

826   8.   Putirka, K. D. Thermometers and barometers for volcanic systems. *Rev Mineral*

827   *Geochem* **69**, 61–120 (2008).

828   9.   Longpré, M. A. & Felpeto, A. Historical volcanism in the Canary Islands; part 1: A

829   review of precursory and eruptive activity, eruption parameter estimates, and

830   implications for hazard assessment. *Journal of Volcanology and Geothermal*

831   *Research* **419**, (2021).

832   10.   Hernandez-Pacheco, A. & Valls, M. C. The historic eruptions of La Palma Island

833   (Canaries). *Arquipélago. Série Ciências da Natureza* 83–94 (1984).

834   11.   Barker, A. K., Troll, V. R., Carracedo, J. C. & Nicholls, P. A. The magma plumbing

835   system for the 1971 Teneguía eruption on La Palma, Canary Islands. *Contributions to*

836   *Mineralogy and Petrology* **170**, 1–21 (2015).

837   12.   Chamberlain, K. J. *et al.* Crystal cargo perspectives on magma assembly and

838   dynamics during the 2021 Tajogaite eruption, La Palma, Canary Islands. *Volcanica* **8**,

839   399–425 (2025).

840   13.   Day, J. M. D. *et al.* Mantle source characteristics and magmatic processes during the

841   2021 La Palma eruption. *Earth Planet Sci Lett* **597**, (2022).

842   14.   Jegal, Y. *et al.* Plagioclase antecrysts record syn-eruptive incorporation of evolved

843   mush during the 2021 Tajogaite eruption (La Palma, Spain). *Contributions to*

844   *Mineralogy and Petrology* **180**, (2025).

845   15.   Klügel, A., Albers, E. & Hansteen, T. H. Mantle and Crustal Xenoliths in a

846   Tephriphonolite From La Palma (Canary Islands): Implications for Phonolite

847   Formation at Oceanic Island Volcanoes. *Front Earth Sci (Lausanne)* **10**, (2022).

848   16.   Klügel, A., Galipp, K., Hoernle, K., Hauff, F. & Groom, S. Geochemical and

849   volcanological evolution of la palma, Canary Islands. *Journal of Petrology* **58**, 1227–

850   1248 (2017).

851   17.   Ubide, T. *et al*. Discrete magma injections drive the 2021 La Palma eruption. *Sci Adv*

852   https://www.science.org (2023).

853   18.   Fourgassie, L. *et al*. Post-traumatic stress disorder in adult population of La Palma

854   (Spain) after the 2021 Tajogaite eruption: Environmental and sociodemographic

855   predictors. *International Journal of Disaster Risk Reduction* **127**, (2025).

856   19.   González-García, D., Boulesteix, T., Klügel, A. & Holtz, F. Bubble-enhanced

857   basanite–tephrite mixing in the early stages of the Cumbre Vieja 2021 eruption, La

858   Palma, Canary Islands. *Sci Rep* **13**, (2023).

859   20.   Dayton, K. *et al*. Deep magma storage during the 2021 La Palma eruption. *Sci Adv* **9**,

860   1–8 (2023).

861   21.   Ibarrola, E. Temporal modification of the basaltic materials from the 1971 eruption

862   of the Teneguía volcano (La Palma, Canary Islands). *Estudios Geológicos* 49–58

863   (1974).

864   22.   Chicharro, N. La erupción de El Charco de 1712, La Palma. Características

865   petrológicas e implicaciones en la peligrosidad volcánica. (Universidad

866   Complutense de Madrid, 2024).

867   doi:https://docta.ucm.es/entities/publication/b8280.

868   23.   Klügel, A., Hoernle, K. A., Schmincke, H. U. & White, J. D. L. The chemically zoned

869   1949 eruption on La Palma (Canary Islands): Petrologic evolution and magma supply

870   dynamics of a rift zone eruption. *J Geophys Res Solid Earth* **105**, 5997–6016 (2000).

871   24.   Ranero, C. R., Torné, M. & Banda, E. Gravity and multichannel seismic reflection

872   constraints on the lithospheric structure of the Canary Swell. *Mar Geophys Res*

873   *(Dordr)* **17**, 519–534 (1995).

874   25.   D'Auria, L. *et al.* Rapid magma ascent beneath La Palma revealed by seismic

875   tomography. *Sci Rep* **12**, (2022).

876   26.   Ubide, T., Larrea, P., Becerril, L. & Galé, C. Volcanic plumbing filters on ocean-island

877   basalt geochemistry. *Geology* **50**, 26–31 (2022).

878   27.   Mollo, S. *et al.* An integrated P-T-H2O-lattice strain model to quantify the role of

879   clinopyroxene fractionation on REE+Y and HFSE patterns of mafic alkaline magmas:

880   Application to eruptions at Mt. Etna. *Earth-Science Reviews* vol. 185 32–56 Preprint

881   at https://doi.org/10.1016/j.earscirev.2018.05.014 (2018).

882   28.   Putirka, K. D., Mikaelian, H., Ryerson, F. & Shaw, H. New clinopyroxene-liquid

883   thermobarometers for mafic, evolved, and volatile-bearing lava compositions, with

884   applications to lavas from Tibet and the Snake River Plain, Idaho. *American*

885   *Minerologist* **88**, 1542–1554 (2003).

886   29.   Romero, J. E. *et al.* The initial phase of the 2021 Cumbre Vieja ridge eruption (Canary

887   Islands): Products and dynamics controlling edifice growth and collapse. *Journal of*

888   *Volcanology and Geothermal Research* **431**, (2022).

889   30.   Castro, J. M. & Feisel, Y. Eruption of ultralow-viscosity basanite magma at Cumbre

890   Vieja, La Palma, Canary Islands. *Nat Commun* **13**, (2022).

891   31.   Neave, D. A. & Putirka, K. D. A new clinopyroxene-liquid barometer , and

892   implications for magma storage pressures under Icelandic rift zones. *American*

893   *Mineralogist* **102**, 777–794 (2017).

894   32.   Dayton, K. *et al*. Magmatic Storage and Volatile Fluxes of the 2021 La Palma

895   Eruption. *Geochemistry, Geophysics, Geosystems* **25**, (2024).

896   33.   Zanon, V., Schiavi, F., Cyrzan, K. & Pankhurst, M. J. *Toward a near Real-Time Magma*

897   *Ascent Monitoring by Combined Fluid Inclusion Barometry and Ongoing Seismicity*.

898   *Sci. Adv* vol. 10 https://www.science.org (2024).

899   34.   Andújar, J. *et al*. Evolution of the crustal reservoir feeding La Palma 2021 eruption.

900   Insights from phase equilibrium experiments and petrologically derived time scales.

901   *Journal of Volcanology and Geothermal Research* **463**, (2025).

902   35.   Fabbrizio, A. *et al*. Phase equilibrium experiments and thermodynamic simulations

903   to constrain the pre-eruptive conditions of the 2021 Tajogaite eruption (Cumbre

904   Vieja volcano, La Palma, Canary Islands). *Journal of Volcanology and Geothermal*

905   *Research* **442**, (2023).

906   36.   del Fresno, C. *et al*. Magmatic plumbing and dynamic evolution of the 2021 La Palma

907   eruption. *Nat Commun* **14**, (2023).

908   37.   Klügel, A., Hansteen, T. H. & Galipp, K. Magma storage and underplating beneath

909   Cumbre Vieja volcano, La Palma (Canary Islands). *Earth Planet Sci Lett* **236**, 211–226

910   (2005).

911   38.   Weis, F. A., Skogby, H., Troll, V. R., Deegan, F. M. & Dahren, B. Magmatic water

912   contents determined through clinopyroxene: Examples from the Western Canary

913   Islands, Spain. *Geochemistry, Geophysics, Geosystems* **16**, 2127–2146 (2015).

914   39.   Wieser, P. E., Gleeson, M. L. M., Matthews, S., DeVitre, C. & Gazel, E. *Determining*

915   *the Pressure-Temperature-Composition (P-T-X) Conditions of Magma Storage*.

916   *Reference Module in Earth Systems and Environmental Sciences* (Elsevier Inc.,

917   2024). doi:10.1016/b978-0-323-99762-1.00024-3.

918   40.   Hansteen, T. H., Kluè, A. & Schmincke, H.-U. *Multi-Stage Magma Ascent beneath the*

919   *Canary Islands: Evidence from Fluid Inclusions*. (1998).

920   41.   Larsen, M. L. Clinopyroxenes and Coexisting Mafic Minerals from the Alkaline

921   Dimaussaq Intrusion, South Greenland. **17**, 258–290 (1976).

922   42.   Bédard, J. H. Parameterizations of calcic clinopyroxene - Melt trace element

923   partition coefficients. *Geochemistry, Geophysics, Geosystems* **15**, 303–336 (2014).

924   43.   Johansen, T. S., Hauff, F., Hoernle, K., Klügel, A. & Kokfelt, T. F. Basanite to phonolite

925   differentiation within 1550-1750 yr: U-Th-Ra isotopic evidence from the A.D. 1585

926   eruption on La Palma, Canary Islands. *Geology* **33**, 897–900 (2005).

927   44.   Turner, S. *et al.* 238 U–230 Th–226 Ra disequilibria constraints on the magmatic

928   evolution of the Cumbre Vieja volcanics on La Palma, Canary Islands. *Journal of*

929   *Petrology* **56**, 1999–2024 (2015).

930   45.   Berthod, C. *et al.* Mantle xenolith-bearing phonolites and basanites feed the active

931   volcanic ridge of Mayotte (Comoros archipelago, SW Indian Ocean). *Contributions to*

932   *Mineralogy and Petrology* **176**, (2021).

933   46.   Ubide, T., Galé, C., Arranz, E., Lago, M. & Larrea, P. Clinopyroxene and amphibole

934   crystal populations in a lamprophyre sill from the Catalonian Coastal Ranges (NE

935   Spain): A record of magma history and a window to mineral-melt partitioning. *Lithos*

936   **184–187**, 225–242 (2014).

937   47.   Baudouin, C., France, L., Boulanger, M., Dalou, C. & Devidal, J. L. Trace element

938   partitioning between clinopyroxene and alkaline magmas: parametrization and role

939   of M1 site on HREE enrichment in clinopyroxenes. *Contributions to Mineralogy and*

940   *Petrology* **175**, (2020).

941   48.   Beloša, L. *et al.* Magmatic evolution and architecture of an oceanic intraplate

942   volcano: Vesteris Seamount, Atlantic Ocean. *Front Earth Sci (Lausanne)* **12**, (2024).

943   49.   MacDonald, A., Ubide, T., Mollo, S. & Taddeucci, J. Spatial and temporal mush

944   heterogeneity during eruptions recorded in clinopyroxene from the 2021 paroxysms

945   at Mt. Etna, Italy. *Contributions to Mineralogy and Petrology* **179**, (2024).

946   50.   MacDonald, A., Ubide, T., Mollo, S., Masotta, M. & Pontesilli, A. Trace element

947   partitioning in zoned clinopyroxene as a proxy for undercooling: Experimental

948   constraints from trachybasaltic magmas. *Geochim Cosmochim Acta* **336**, 249–268

949   (2022).

950   51.   Mollo, S., Del Gaudio, P., Ventura, G., Iezzi, G. & Scarlato, P. Dependence of

951   clinopyroxene composition on cooling rate in basaltic magmas: Implications for

952   thermobarometry. *Lithos* **118**, 302–312 (2010).

953   52.   Barker, A. K., Rydeblad, E. M. & Silva, S. M. D. M. Magma Storage at Ocean Islands:

954   Insights From Cape Verde. in *Crustal Magmatic System Evolution: Anatomy,*

955 *Architecture, and Physico-Chemical Processes* 45–78 (wiley, 2021).

956 doi:10.1002/9781119564485.ch3.

957 53. Longpré, M. A., Troll, V. R. & Hansteen, T. H. Upper mantle magma storage and

958 transport under a Canarian shield-volcano, Teno, Tenerife (Spain). *J Geophys Res*

959 *Solid Earth* **113**, (2008).

960 54. Longpré, M. A., Klügel, A., Diehl, A. & Stix, J. Mixing in mantle magma reservoirs prior

961 to and during the 2011-2012 eruption at El Hierro, Canary Islands. *Geology* **42**, 315–

962 318 (2014).

963 55. Torres-González, P. A. *et al.* Unrest signals after 46 years of quiescence at Cumbre

964 Vieja, La Palma, Canary Islands. *Journal of Volcanology and Geothermal Research*

965 **392**, 106757 (2020).

966 56. Petrone, C. M. *et al.* Magma recharge and mush rejuvenation drive paroxysmal

967 activity at Stromboli volcano. *Nat Commun* **13**, (2022).

968 57. Petrelli, M., Morgavi, D., Vetere, F. & Perugini, D. Elemental imaging and petro-

969 volcanological applications of an improved Laser Ablation Inductively Coupled

970 Quadrupole Plasma Mass Spectrometry. *Periodico di Mineralogia* vol. 85 25–39

971 Preprint at https://doi.org/10.2451/2015PM0465 (2016).

972 58. Ágreda-López, M. *et al.* The crystal cargo provides a chronicle of pre-caldera

973 dynamics in mafic volcanic systems: insights from Colli Albani. *Bull Volcanol* **87**,

974 (2025).

975   59.   Paton, C., Hellstrom, J., Paul, B., Woodhead, J. & Hergt, J. Iolite: Freeware for the

976   visualisation and processing of mass spectrometric data. *J Anal At Spectrom* **26**,

977   2508–2518 (2011).

978   60.   Costa, S. *et al.* A data driven approach to mineral chemistry unveils magmatic

979   processes associated with long-lasting, low-intensity volcanic activity. *Sci Rep* **13**,

980   1–15 (2023).

981   61.   Musu, A. *et al.* The magmatic evolution of South-East Crater (Mt. Etna) during the

982   February–April 2021 sequence of lava fountains from a mineral chemistry

983   perspective. *Bull Volcanol* **85**, (2023).

984   62.   Petrelli, M. Machine Learning in Petrology: State-of-the-Art and Future Perspectives.

985   *Journal of Petrology* **65**, (2024).

986   63.   MacDonald, A., Ubide, T., Mollo, S., Pontesilli, A. & Masotta, M. The Influence of

987   Undercooling and Sector Zoning on Clinopyroxene-Melt Equilibrium and

988   Thermobarometry. *Journal of Petrology* **64**, 1–18 (2023).

989   64.   Masotta, M., Mollo, S., Freda, C., Gaeta, M. & Moore, G. Clinopyroxene-liquid

990   thermometers and barometers specific to alkaline differentiated magmas.

991   *Contributions to Mineralogy and Petrology* **166**, 1545–1561 (2013).

992   65.   Longpré, M. A. *et al.* Shifting melt composition linked to volcanic tremor at Cumbre

993   Vieja volcano. *Nat Geosci* https://doi.org/10.1038/s41561-024-01623-x (2025)

994   doi:10.1038/s41561-024-01623-x.

995   66.   Pankhurst, M. J. *et al*. Rapid response petrology for the opening eruptive phase of the

996   2021 Cumbre Vieja eruption, La Palma, Canary Islands. *Volcanica*

997   https://doi.org/11.21223/rs.3.rs-963593/v1 (2022).

998   67.   Wieser, P. E. *et al*. Thermobar: An open-source Python3 tool for thermobarometry

999   and hygrometry. *Volcanica* **5**, 349–384 (2022).

1000   68.   Neave, D. A. *et al*. Clinopyroxene-Liquid Equilibria and Geothermobarometry in

1001   Natural and Experimental Tholeiites: The 2014-2015 Holuhraun Eruption, Iceland.

1002   *Journal of Petrology* **60**, 1653–1680 (2019).

1003   69.   Carracedo, J. C., Badiola, E. R., Guillou3, H., De La Nuez, J. & Torrados, F. J. P.

1004   *Geology and Volcanology of La Palma and El Hierro, Western Canaries*. *Estudios*

1005   *GeoJ* vol. 57 175–273 (2001).

1006   70.   Day, J. M. D. *et al*. Mantle source characteristics and magmatic processes during the

1007   2021 La Palma eruption. *Earth Planet Sci Lett* **597**, 117793 (2022).

1008   71.   Palme, H. & O'Neill, H. Cosmochemical Estimates of Mantle Composition. in

1009   *Treatise on Geochemistry: Second Edition* vol. 3 1–39 (Elsevier Inc., 2014).

1010   72.   Tenzer, R., Bagherbandi, M. & Vajda, P. Global model of the upper mantle lateral

1011   density structure based on combining seismic and isostatic models. *Geosciences*

1012   *Journal* **17**, 65–73 (2013).

1013

Recurrent evacuation of mantle mush by mafic recharge in ocean island basalts, recorded by La Palma clinopyroxene

Alberto Caracciolo, Teresa Ubide, Mónica Ágreda-López, Raquel Herrera, Alvaro Marquez, Diego González-García, Maria Jose Huertas, Eumenio Ancochea, Nicolás Chicharro, Juan Jesús Coello-Bravo, Maurizio Petrelli

Supplementary Material Text and Figures

Corresponding author: Alberto Caracciolo, (alberto@hi.is)

Table of Contents

1. Geological setting

The Canary Islands are an example of intraplate volcanism, commonly attributed to a hotspot beneath Jurassic oceanic lithosphere (Wilson, 1973), although alternative plate-related models have also been proposed (e.g. Anguita et al., 2025). La Palma is one of the westernmost and youngest islands of the archipelago. It is composed of the older, now extinct Garafía and Taburiente shield volcanoes in the north, and the younger, historically active Cumbre Vieja ridge in the south (Fig. 1). La Palma is the most volcanically active island in the Canaries during historical times, having experienced eight eruptions since the late 15th century, including the most recent Tajogaite eruption in 2021 (Carracedo et al., 2022; Hernandez-Pacheco and Valls, 1984). Historical eruptions occurred in 1470, 1585, 1677-78, 1712, 1949, 1971 and 2021, with return periods varying between 22 and 237 years (Longpré and Felpeto, 2021). Eruptions at Cumbre Vieja are typically strombolian, producing highly alkaline magma series, ranging from basanitic to tephritic lavas (Klugel et al., 1999) although more evolved phonolites are occasionally erupted (Klügel et al., 2022). In this work, we focus on the 1712 El Charco, 1971 Teneguía and 2021 Tajogaite eruptions (Fig. 1), for which we have well characterized samples across the tephrite and basanite stages.

The 1712 El Charco eruption is the least documented eruption of the Canaries and the available information is described by Romero Ruiz (1990). The 1712 eruption occurred in the central west part of Cumbre Vieja and began on October 9, with the opening of a main cone and multiple secondary vents along a 3 km-long fracture, trending SE–NW. Although there was some phreatomagmatic activity, the eruption was essentially strombolian, producing lava flows approximately 5 km in length that reached the sea, forming several lava deltas. The eruption lasted for 56 days, from October 9 to December 3, 1712 (Romero Ruiz, 1990). This event produced tephrite to basanite lavas (Chicharro Fermín, 2024), with an estimated total lava volume of 36 x 10^6 m^3 (Longpré and Felpeto, 2021). Samples for El Charco 1712 were collected from different parts of the lava field, and amphibole-bearing tephrites are consistently found at the bottom of the olivine-bearing basanites (Supplementary Data Table 1, SDT1).

The 1971 Teneguía eruption took place at the southern tip of La Palma, near the site of the 1677–1678 eruption. Activity began on October 26 with the opening of an eruptive fissure that produced pyroclastic material and lava flows, which rapidly reached the coast. Several vents were active during the eruption. The eruption continued for 24 days, ending on November 18, 1971. This event produced tephrite to basanite lavas and the total eruption volume is estimated to be 40 x 10^6 m^3 (Afonso et al.,

1974; Longpré and Felpeto, 2021). Samples from the 1971 Teneguía eruption were collected during the eruption, allowing the construction of a time series of samples (SDT1).

The Tajogaite 2021 eruption began on 19 September 2021, at Cabeza de Vaca locality, in the middle part of Cumbre Vieja ridge. The eruption began with Strombolian activity and lava fountaining, transitioning to more intense lava and pyroclastic emissions from multiple vents in October–November 2021. Early tephritic magmas shifted to basanitic compositions over the first few days, with the eruption ending on 13 December 2021. The minimum erupted volume is estimated at 170 ± 85 $\times 10^6$ m^3 (Bonadonna et al., 2022). For this most recent eruption, modern geophysical and petrological monitoring provide a more detailed eruption evolution. The first signs of volcanic unrest preceding the 2021 Tajogaite eruption occurred in 2017, interpreted as related to magmatic intrusions (Fernández et al., 2021; Torres-González et al., 2020). After eight days of seismic swarms, the eruption began on 19 September 2021, producing tephritic magma rich in amphibole and clinopyroxene until the first break on 27 September (Pankhurst et al., 2022; Ubide et al., 2023). Following the few-hours long break, the eruption continued emitting more fluid basanite magmas, dominated by olivine and clinopyroxene crystals, until the end of the eruption, on 13 December 2021 (e.g. Day et al., 2022; Ubide et al., 2023). Temporal changes are observed during the 2021 Tajogaite eruption, the most significant being a shift towards more mafic melts over the course of the eruption, followed by a reversal in that trend since the end of November to the end of the eruption, as observed in clinopyroxene, plagioclase and olivine rims, microlites, matrix and whole rock compositions (Bonechi et al., 2024; Chamberlain et al., 2025; Day et al., 2022; Dayton et al., 2023; Ubide et al., 2023). The eruption is overall interpreted as a result of a mafic basanite magma gradually invading a tephrite reservoir (e.g. Day et al., 2022; Ubide et al., 2023), with the basanite sourced from the upper mantle and interacting with a tephrite reservoir located in the upper mantle (e.g. Chamberlain et al., 2025; Ubide et al., 2023) or in the middle to lower crust (Fabbrizio et al., 2023; Scarrow et al., 2024). Samples from Tajogaite 2021 eruption were collected both during and after the eruption and correspond to the same sample set published in Ubide et al. (2023) (SDT1).
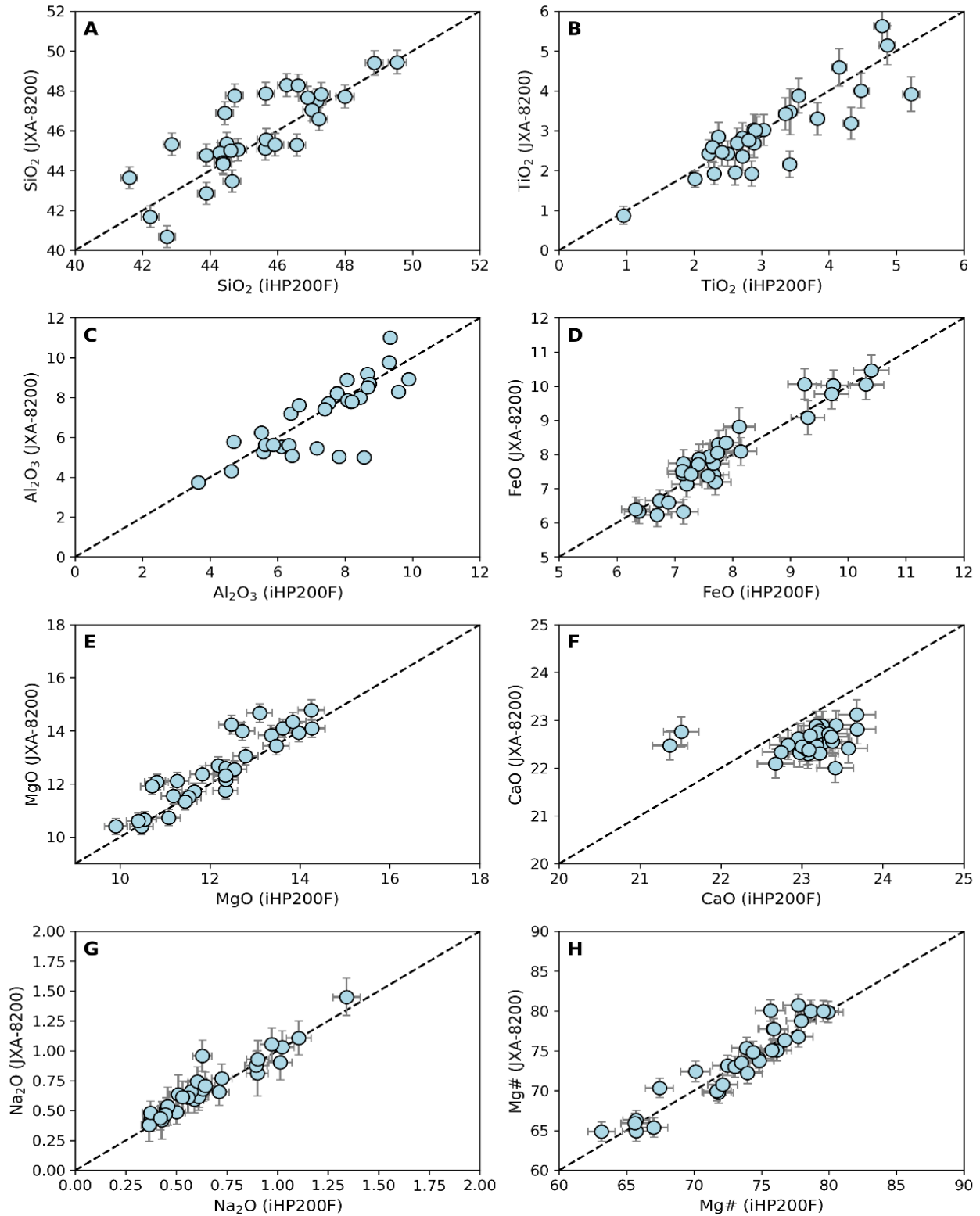
Fig. S1. EMPA Comparison El Charco 1712. Comparison of major and minor element data for samples from El Charco 1712 collected with the new iHP200F microprobe in Madrid and JXA-8200 microprobe in Huelva. Error bars indicate 2σ uncertainties derived from EMPA counting statistics.

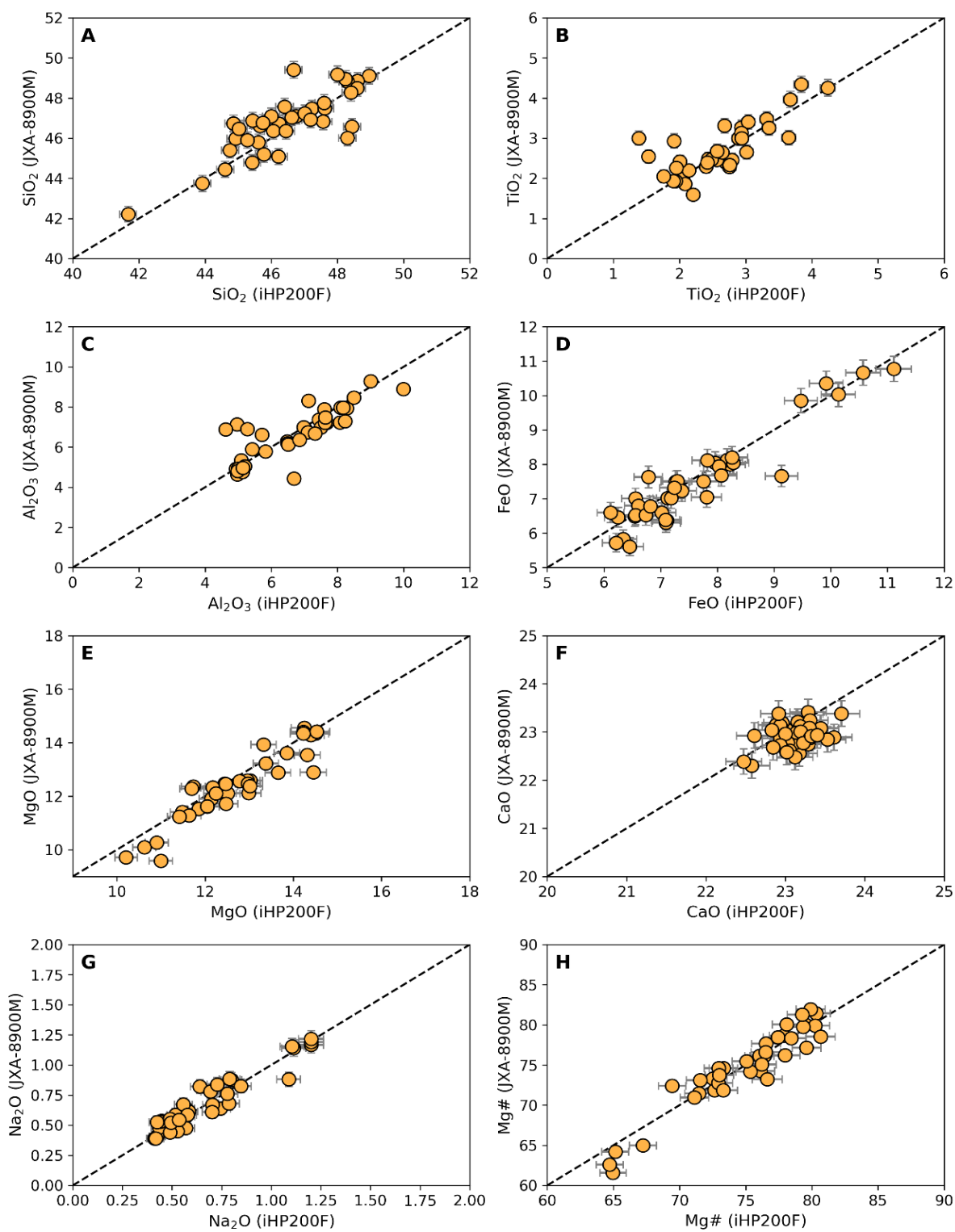**Comparison: iHP200F (Madrid new) vs JXA-8900M (Madrid old)**

Fig. S2. EMPA Comparison Tajogaite 2021. Comparison of major and minor element data for samples from Tajogaite 2021 collected with the iHP200F microprobe in Madrid and the old JXA-8900M microprobe in Madrid. Error bars indicate 2σ uncertainties derived from EMPA counting statistics.

El Charco 1712 – Cpx 22
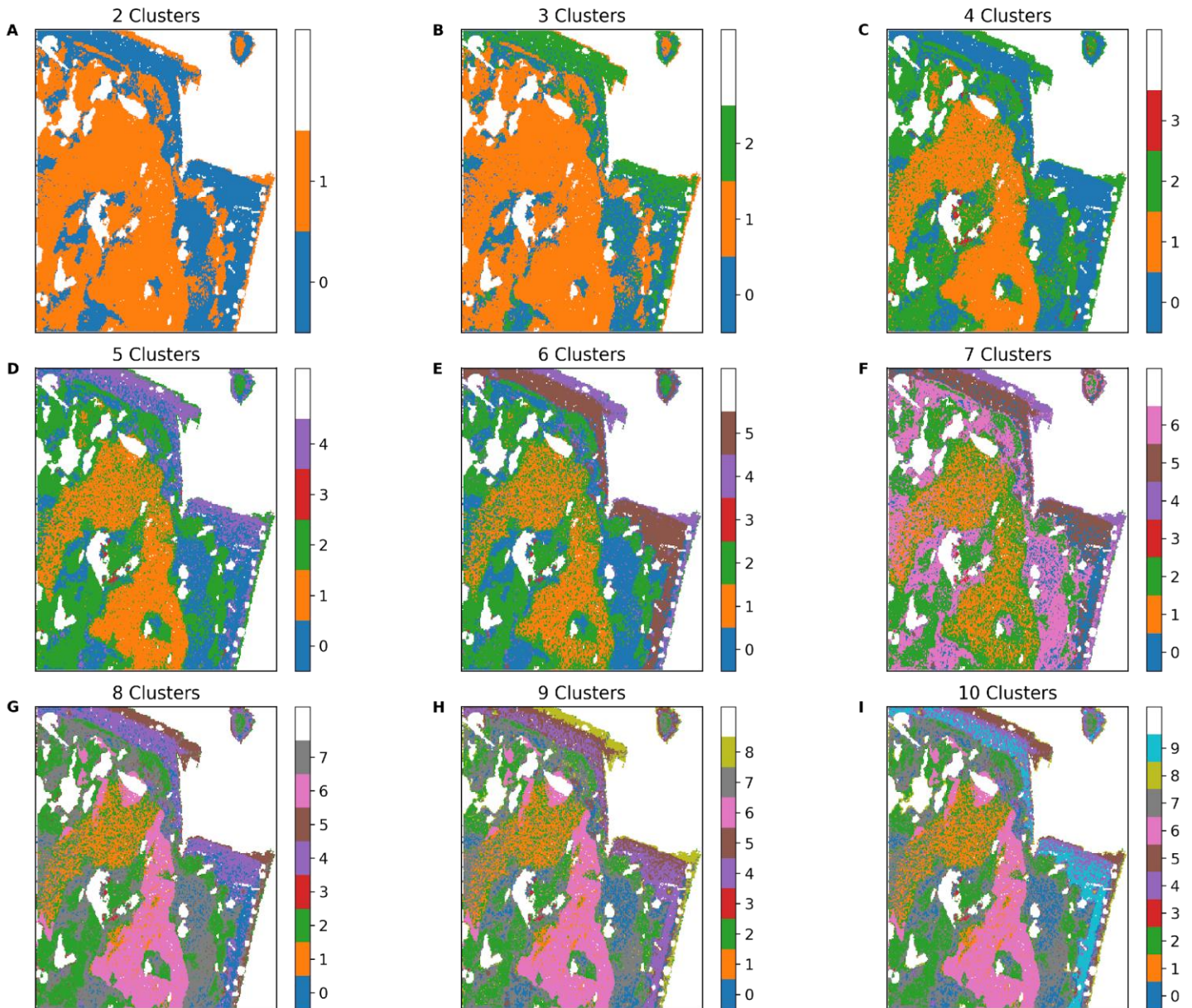
Fig. S3. Clustering number. Example of a clinopyroxene map from El Charco 1712 (Cpx 22), color-coded according to varying numbers of clusters (ranging from 2 to 10). Based on visual inspection, we consider 6 clusters to be the optimal number, as it avoids both oversimplification and excessive complexity of the chemical variations.

Legend: Primitive Core, Inner Rim, Outer Rim, Microlite, B2015; W2015

El Charco 1712 — **Teneguía 1971** — **Tajogaite 2021**

Panel A (El Charco 1712, P (kbar) - P2003): n = 56, n = 25, n = 52, n = 42, n = 15
Panel B (El Charco 1712, P (kbar) - P2003 + P2008): n = 52, n = 25, n = 52, n = 42, n = 13
Panel C (El Charco 1712, P (kbar) - M2018): n = 57, n = 25, n = 52, n = 42, n = 15
Panel D (El Charco 1712, P (kbar) - M2018 + P2008): n = 56, n = 25, n = 52, n = 42, n = 13
Panel E (El Charco 1712, P (kbar) - N&P2017 + P2008): n = 50, n = 24, n = 49, n = 42, n = 14

Panel F (Teneguía 1971, P (kbar) - P2003): n = 46, n = 16, n = 72, n = 41, n = 458
Panel G (Teneguía 1971, P (kbar) - P2003 + P2008): n = 44, n = 16, n = 72, n = 41, n = 437
Panel H (Teneguía 1971, P (kbar) - M2018): n = 47, n = 16, n = 72, n = 41, n = 467
Panel I (Teneguía 1971, P (kbar) - M2018 + P2008): n = 46, n = 16, n = 72, n = 41, n = 471
Panel J (Teneguía 1971, P (kbar) - N&P2017 + P2008): n = 42, n = 16, n = 72, n = 41, n = 410

Panel K (Tajogaite 2021, P (kbar) - P2003): n = 380, n = 256, n = 387, n = 157, n = 5
Panel L (Tajogaite 2021, P (kbar) - P2003 + P2008): n = 377, n = 256, n = 386, n = 157, n = 5
Panel M (Tajogaite 2021, P (kbar) - M2018): n = 369, n = 256, n = 388, n = 156, n = 5
Panel N (Tajogaite 2021, P (kbar) - M2018 + P2008): n = 381, n = 256, n = 388, n = 157, n = 5
Panel O (Tajogaite 2021, P (kbar) - N&P2017 + P2008): n = 336, n = 253, n = 386, n = 157, n = 5

Earthquakes 2021

KDE Density — KDE Density — KDE Density

Depth (km)

SEE

9

Fig. S4. Comparison of P results. Comparison of clinopyroxene – melt magma storage depths using different temperature-dependent barometers coupled with different thermometers. For this comparison we used more relaxed equilibrium criteria as explained in Supplementary Section 5. P2003: barometer of Putirka et al. (2003), coupled with the thermometer of Putirka et al. (2003). P2003 + P2008: barometer of Putirka et al. (2003), coupled with the thermometer (eq. 33) of Putirka (2008). M2018: barometer of Mollo et al. (2018), coupled with thermometer of Mollo et al. (2018). M2018 + P2008: barometer of Mollo et al. (2018), coupled with thermometer (eq. 33) of Putirka (2008). N&P2017 + P2008: barometer of Neave & Putirka (2017) coupled with thermometer (eq. 33) of Putirka (2008). Overall, we note only minor differences among the various calibrations, all of which suggest clinopyroxene crystallization in the upper mantle. Gray fields indicate the location of seismicity during the 2021 Tajogaite eruption (D'Auria et al., 2022). B2015: Barker et al. (2015). W2015: Weis et al. (2015).
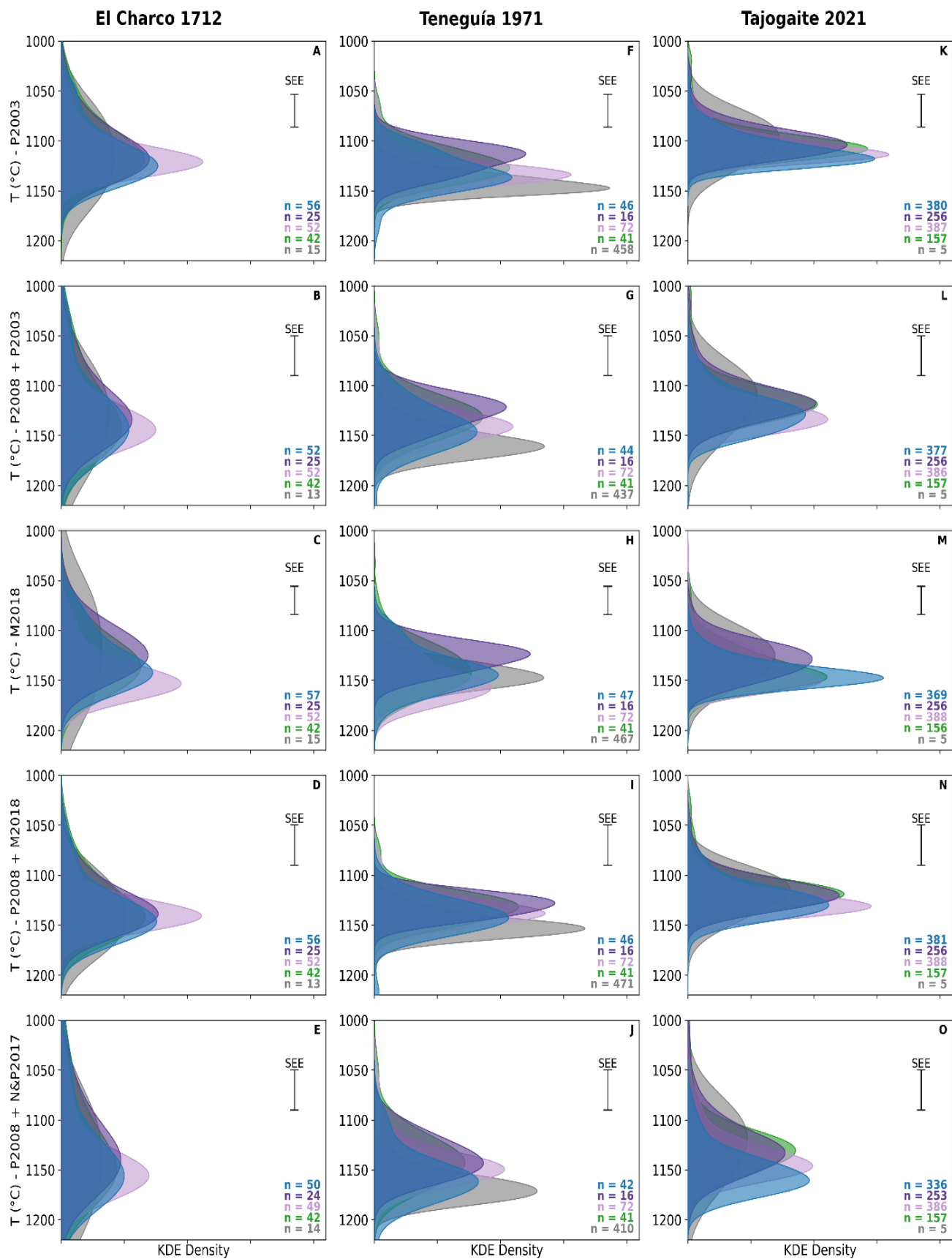
Fig. S5. Comparison of T results. Comparison of clinopyroxene – melt magma storage temperatures using different pressure-dependent thermometers coupled with different barometers. P2003: thermometer of Putirka et al. (2003), coupled with the barometer of Putirka et al. (2003). P2003 + P2008: thermometer of Putirka et al. (2003), coupled with the barometer (eq. 33) of Putirka (2008). M2018: thermometer of Mollo et al. (2018), coupled with barometer of Mollo et al. (2018). M2018 + P2008: thermometer of Mollo et al. (2018), coupled with barometer (eq. 33) of Putirka (2008). N&P2017 + P2008: thermometer of Neave & Putirka (2017) coupled with barometer (eq. 33) of Putirka (2008).

2. Clinopyroxene major elements
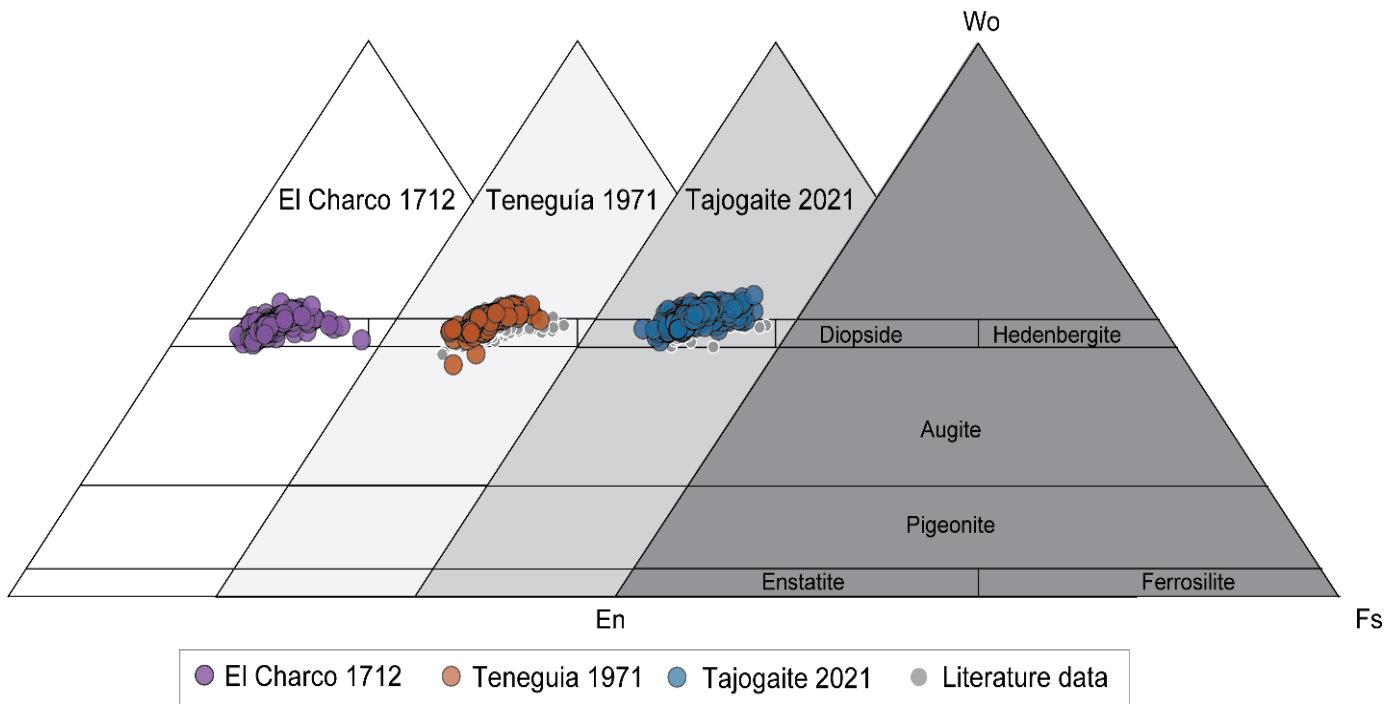
Fig. S6. Classification of Cpx. Composition of clinopyroxene crystals in the En-Fs-Wo ternary diagram. All compositions plot within the diopside field, with no differences between eruptions. Gray symbols represent clinopyroxene data from the literature (Barker et al., 2015; González-García et al., 2023; Ubide et al., 2023; Weis et al., 2015).
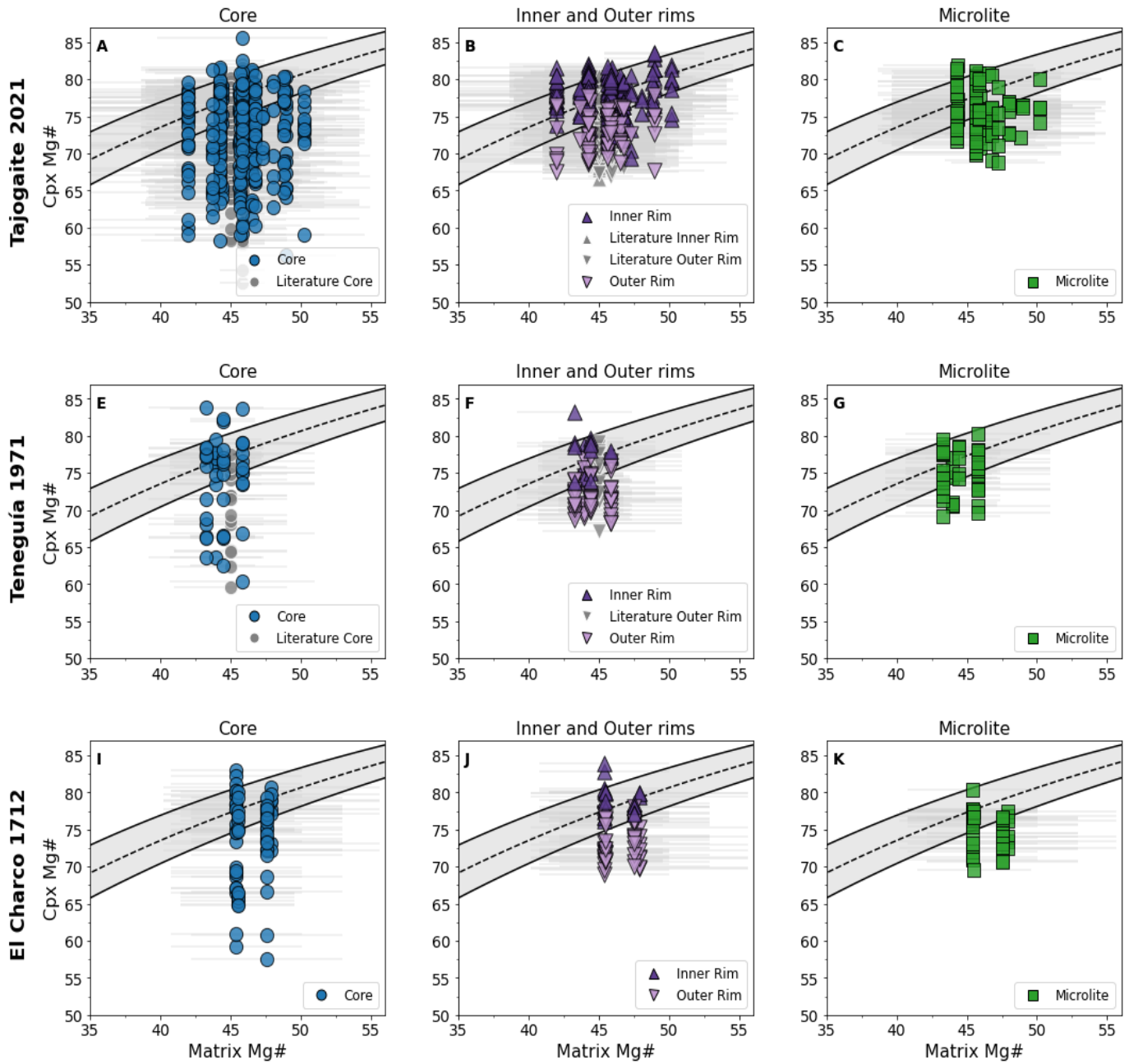
Fig. S7. Cpx – melt equilibrium. Matrix Mg# vs clinopyroxene Mg# for (A-C) Tajogaite 2021 (E-G) Teneguía 1971 and (I-K) El Charco 1712. Each symbol and color represent a different textural position (Core, Inner and Outer rims, Microlites, and Cpx inclusions), as indicated in the legend. Gray symbols correspond to literature data (Barker et al., 2015; González-García et al., 2023; Weis et al., 2015). Inner rim and microlite compositions from the 2021 Tajogaite eruption are from Ubide et al. (2023). The gray field in each panel indicates the KD(Fe–Mg)$_{cpx–melt}$ of 0.28 ± 0.08 (Putirka, 2008), which is used to assess major element equilibrium between clinopyroxene and the matrix composition. Horizontal error bars reflect the matrix Mg# 2σ variability.

13
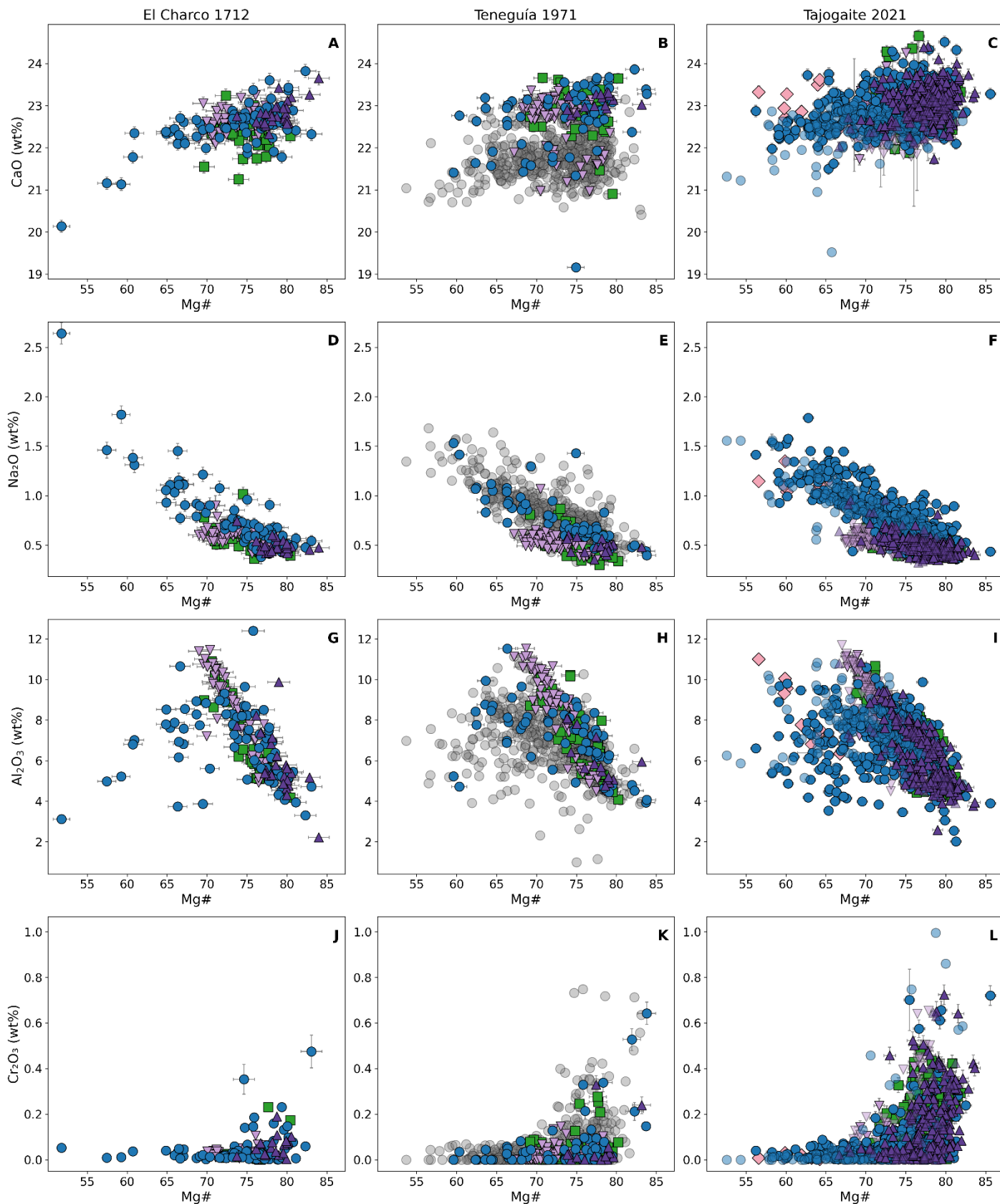
Fig. S8. Cpx major element. CaO, Na$_2$O, Al$_2$O$_3$ and Cr$_2$O$_3$ variation in clinopyroxene from the different eruptions studied in this work, with symbols and colors based on different textural positions. Literature data for Teneguía 1971 from Barker et al. (2015) and Weis et al. (2015) are not grouped into textures and are ploted as filled faded grey circles. For Tajogaite 2021, literature data are from González-García et al. (2023), shown with faded colours according to textural positions. We observe an offset in CaO contents between our data and previously published data from Teneguía, and a minor offset also in Na$_2$O and Al$_2$O$_3$ (Barker et al., 2015; Weis et al., 2015). We consider our measurements of good quality, as they closely match concentrations in clinopyroxenes from other eruptions, which were analyzed using various microprobes. The data quality is further supported by our cross-validation across instruments (see Fig. S1-S2). In contrast, the literature data from Teneguía (Barker et al., 2015; Weis et al., 2015) were acquired using the same instrument (JEOL JXA-8530F at Uppsala University), and the observed discrepancy may reflect a calibration issue specific to CaO and on that instrument. Error bars indicate 2σ uncertainties derived from EMPA counting statistics.
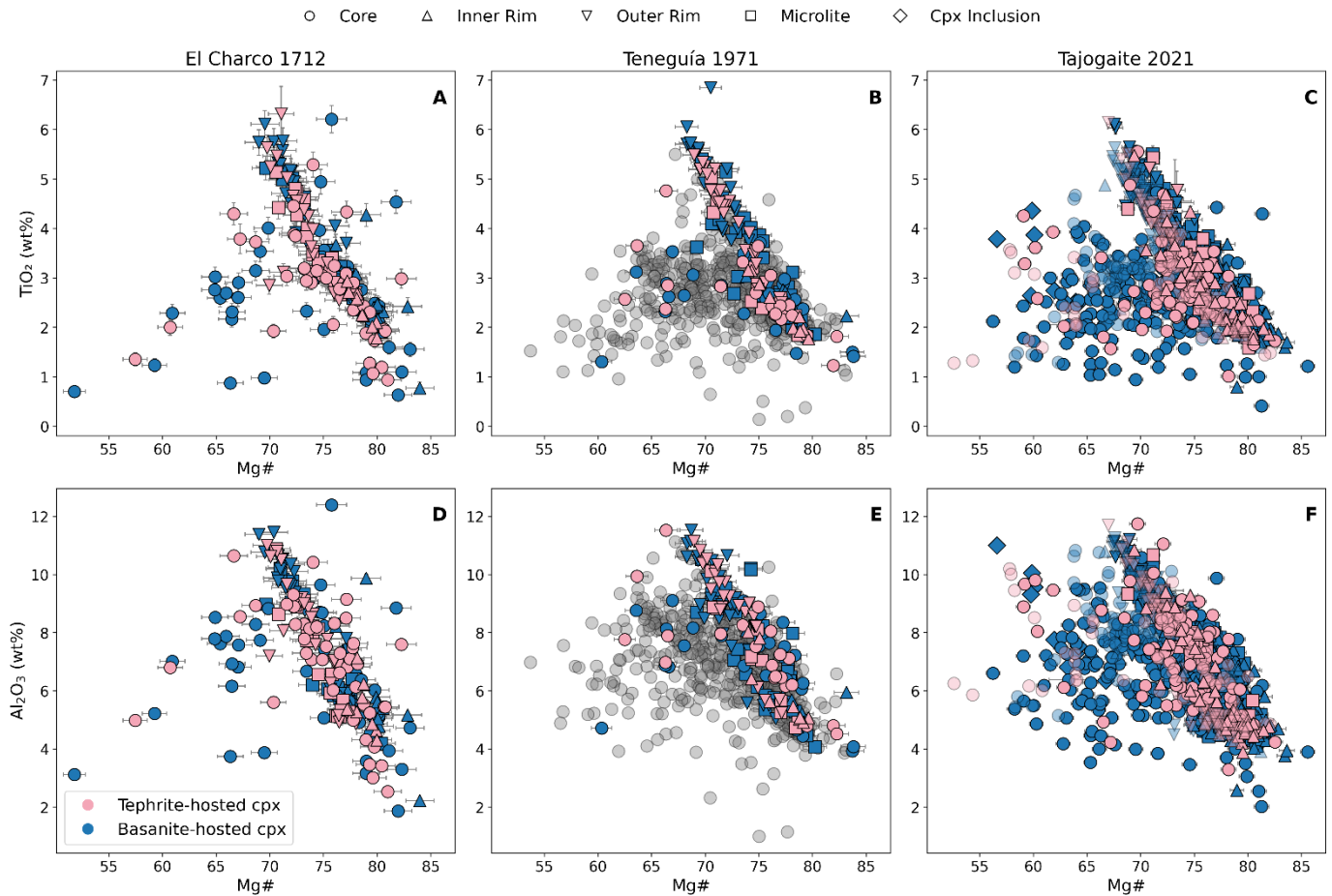
Fig. S9. Tephrite and Basanite-hosted Cpx. (A–C) TiO$_2$ and (D–F) Al$_2$O$_3$ variations as a function of Mg# in clinopyroxene, color-coded based on whether they occur in amphibole-bearing tephrite (pink) or olivine-bearing basanite (blue) rocks. No clear relationship is observed between clinopyroxene composition and rock type. .

Literature data for Teneguía 1971 from Barker et al. (2015) and Weis et al. (2015) are plotted as faded filled grey circles. For Tajogaite 2021, literature data are from González-García et al. (2023), shown with faded colors. Error bars indicate 2σ uncertainties derived from EMPA counting statistics.
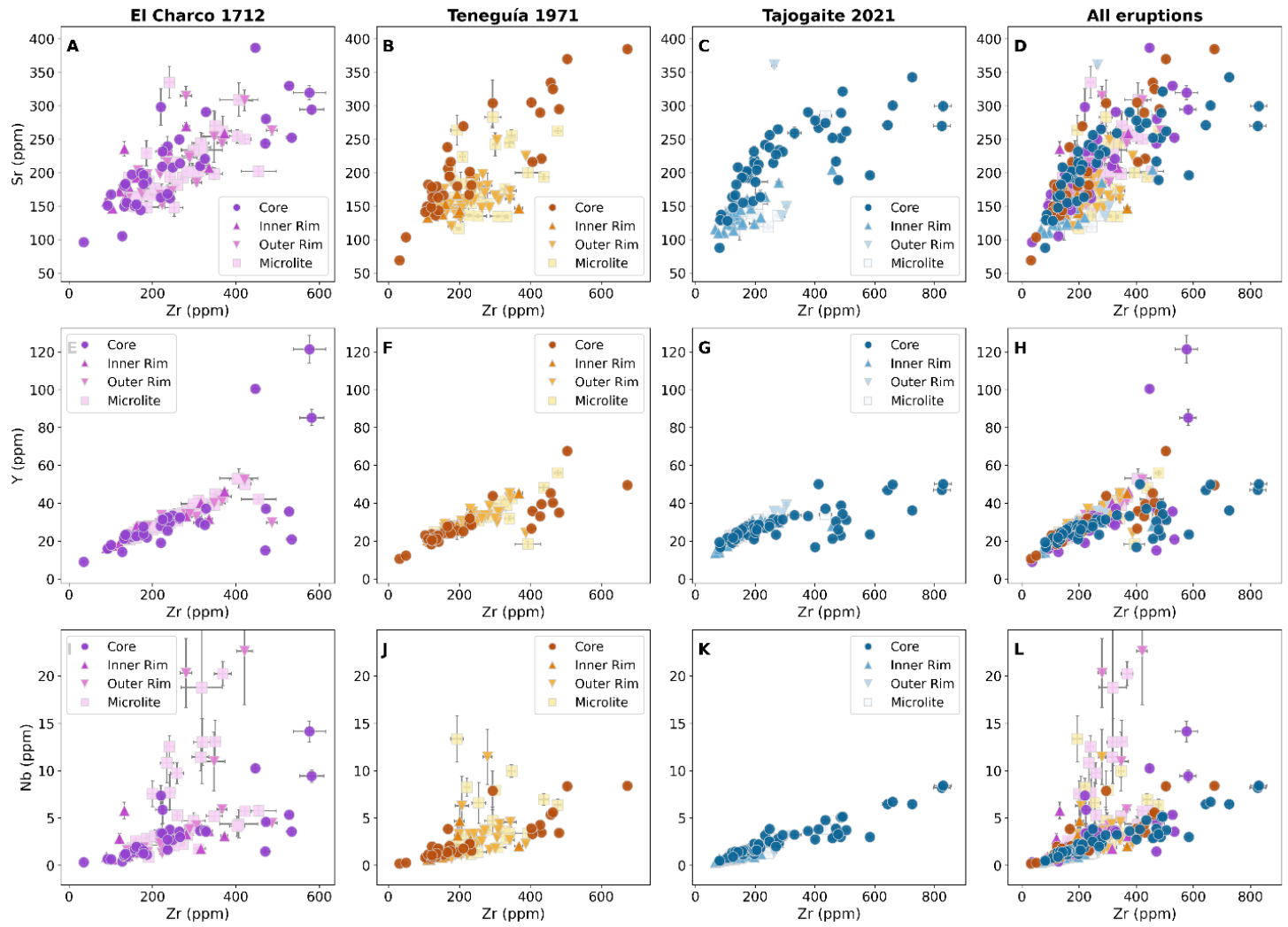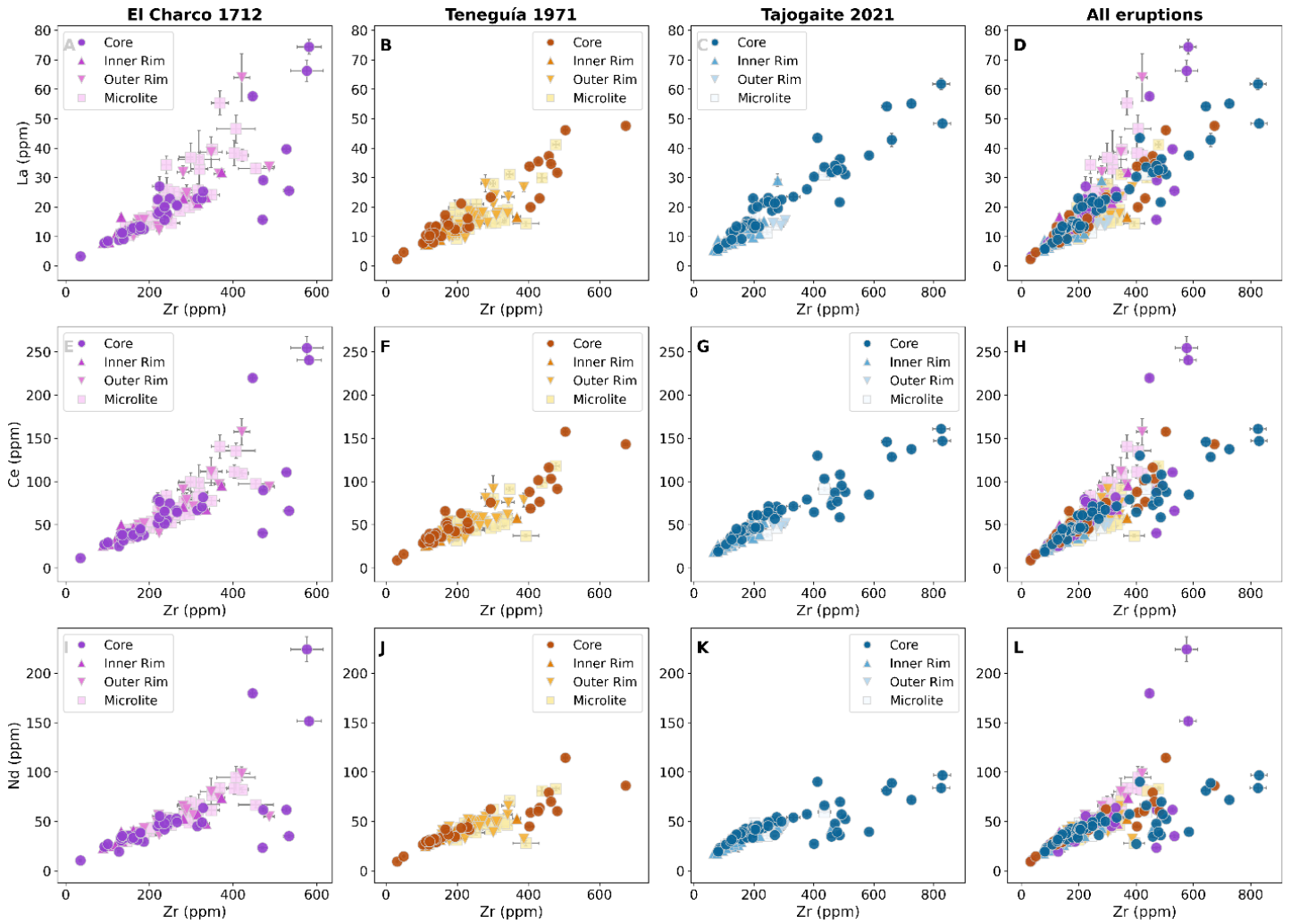
3. Clinopyroxene trace elements
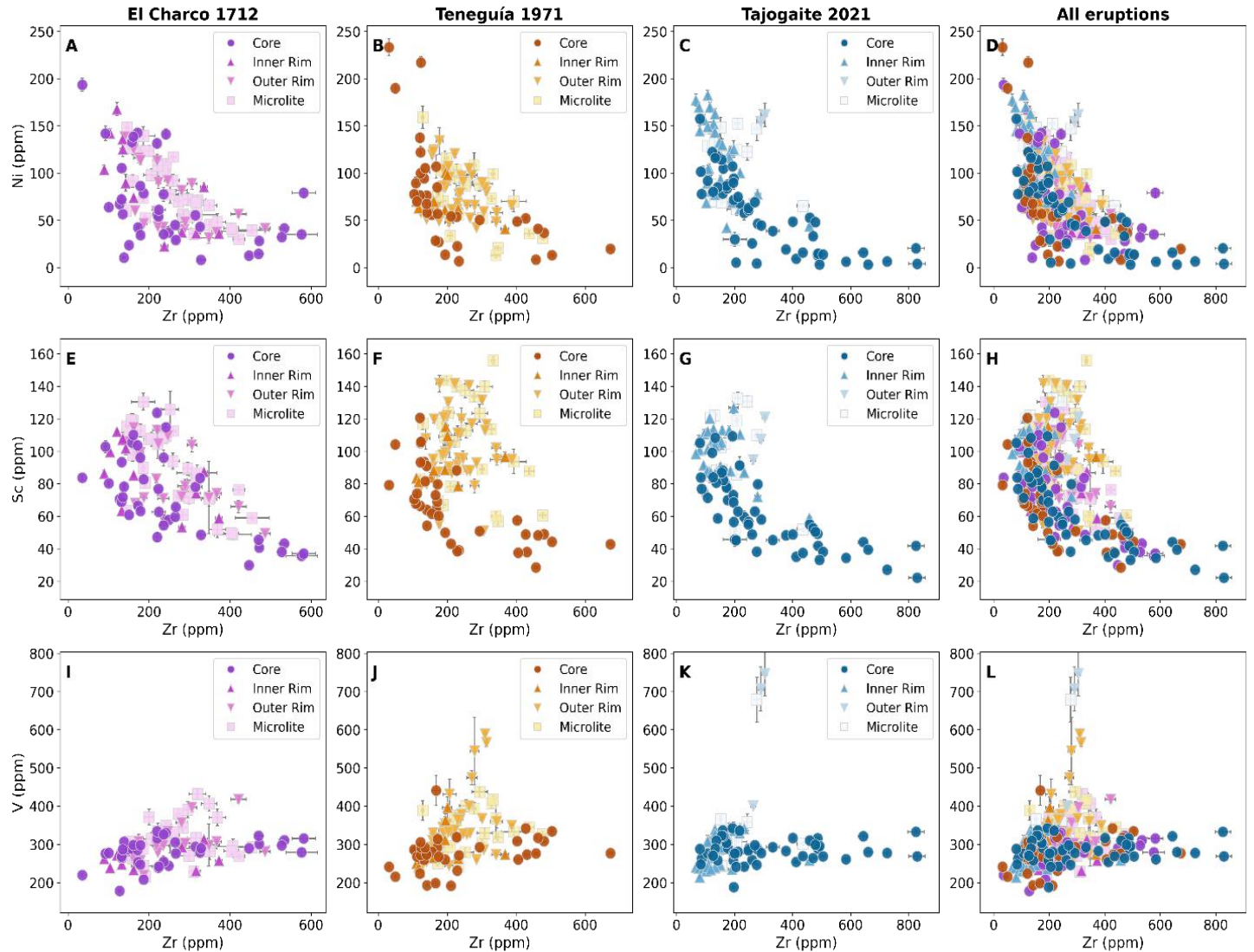
Fig. S10. Cpx compatible TE composition (NI, Sc, V). Clinopyroxene trace element bivariant plots of (A-D) Ni (E-H) Sc and (I-L) V vs Zr. Each column corresponds to a different eruption, as indicated by the column titles, with the final column showing data from all eruptions combined. Each symbol represents a different clinopyroxene textural position. Error bars indicate the internal 2SE analytical uncertainty.

Fig. S11. Cpx incompatible TE composition (Sr, Y, Nb). Clinopyroxene trace element bivariant plots of (A-D) Sr (E-H) Y and (I-L) Nb vs Zr. Each column corresponds to a different eruption, as indicated by the column titles, with the final column showing data from all eruptions combined. Each symbol represents a different clinopyroxene textural position. Error bars indicate the internal 2SE analytical uncertainty.

Fig. S12. Cpx incompatible TE composition (La, Ce, Nd). Clinopyroxene trace element bivariant plots of (A-D) La (E-H) Ce and (I-L) Nd vs Zr. Each column corresponds to a different eruption, as indicated by the column titles, with the final column showing data from all eruptions combined. Each symbol represents a different clinopyroxene textural position. Error bars indicate the internal 2SE analytical uncertainty.
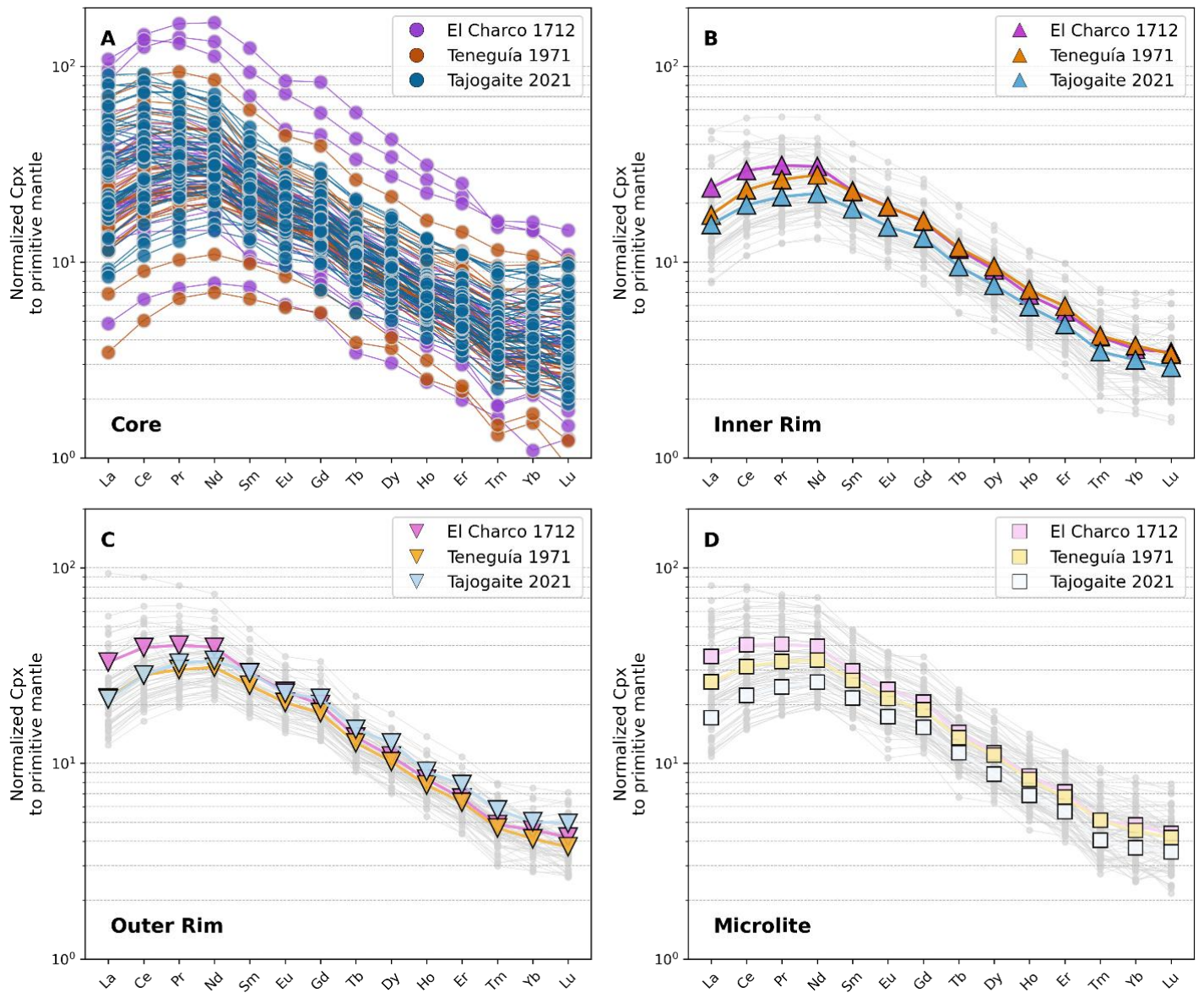
Fig. S13. Texture-grouped cpx REE patterns. Rare earth element (REE) patterns of clinopyroxene, normalized to the composition of primitive mantle (Palme and O'Neill, 2014). REE patterns of cores are shown as individual data, whereas for inner rims, outer rims, and microlites we show the average for each eruption, with individual patterns displayed in light grey.
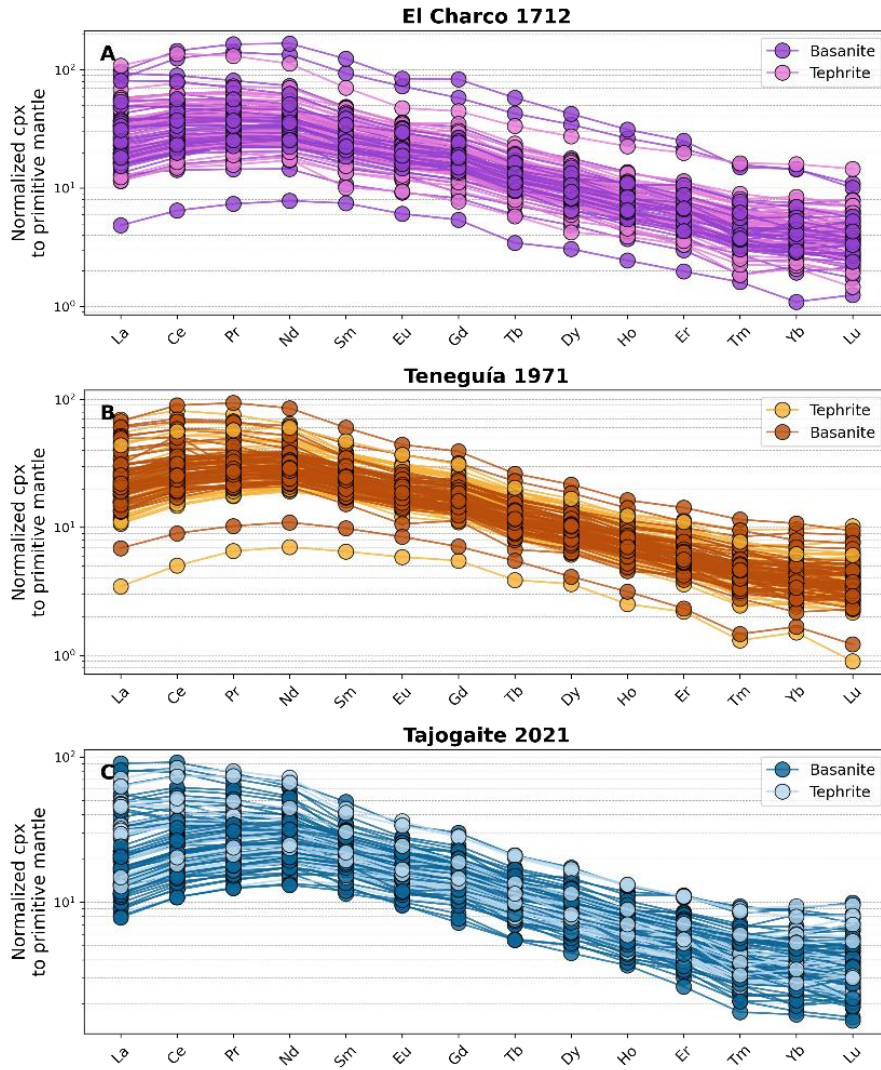
Fig. S14. Rock-grouped cpx REE patterns. Clinopyroxene trace element patterns colored by host rock type, tephrite and basanite.
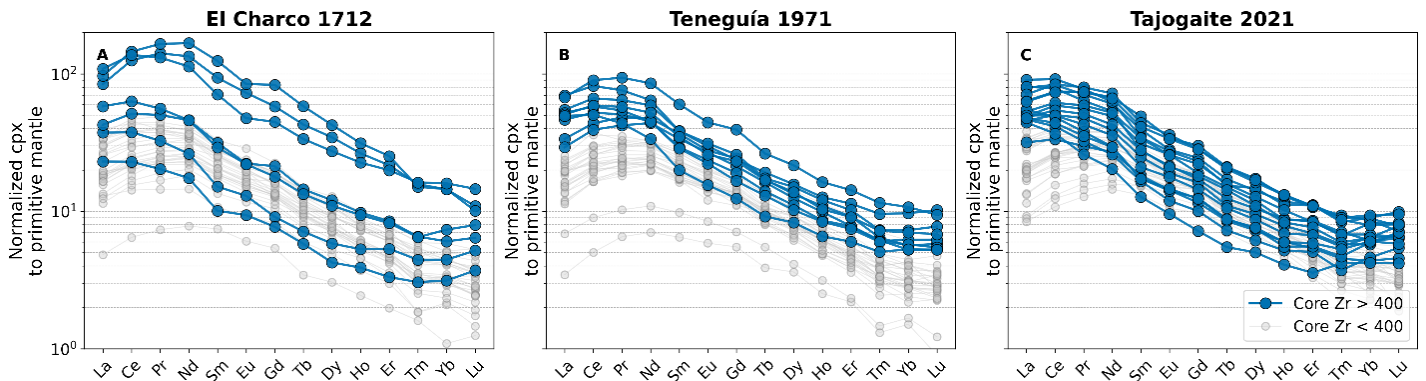
Fig. S15. Cpx core REE patterns. Trace element pattern of clinopyroxene cores, color-coded based on Zr concentrations, used as a proxy for magma evolution. Evolved core compositions (Zr>400 ppm), marked in blue,

are the most fractionated and show a slight enrichment in heavy REE elements Tm, Yb and Lu compared to less evolved core compositions (Zr<400 ppm).
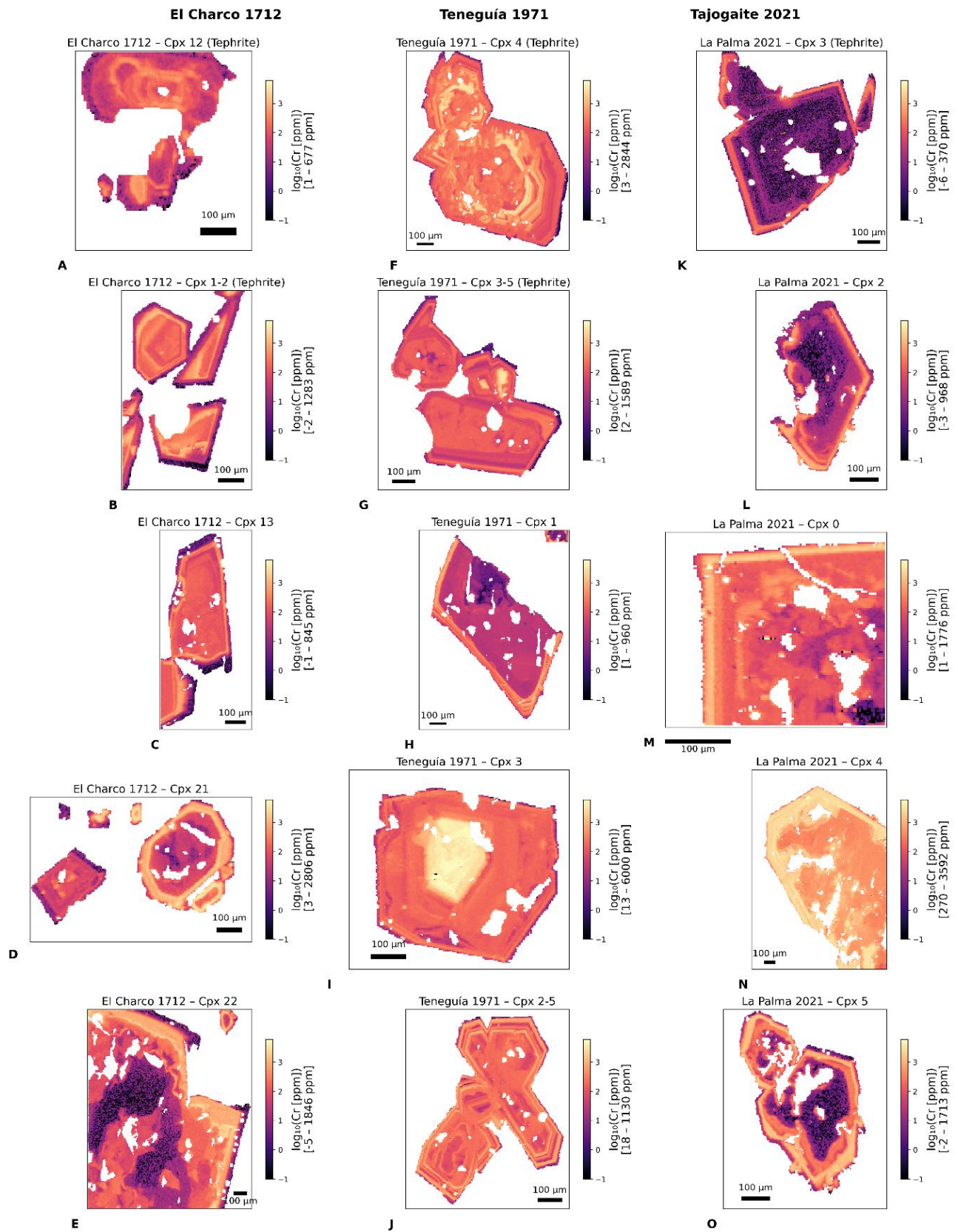
Fig. S16. Cr chemical maps. LA-ICP-MS maps of Cr in clinopyroxene from El Charco 1712, Teneguía 1971 and Tajogaite 2021. Maps are visualized using a logarithmic scale and scaled to the maximum common range observed across all maps (0.1–6000 ppm Cr; $\log_{10}$ = -1–3.8) to allow direct comparison of Cr variations among samples and eruptions.

4. Geochemistry of the matrix
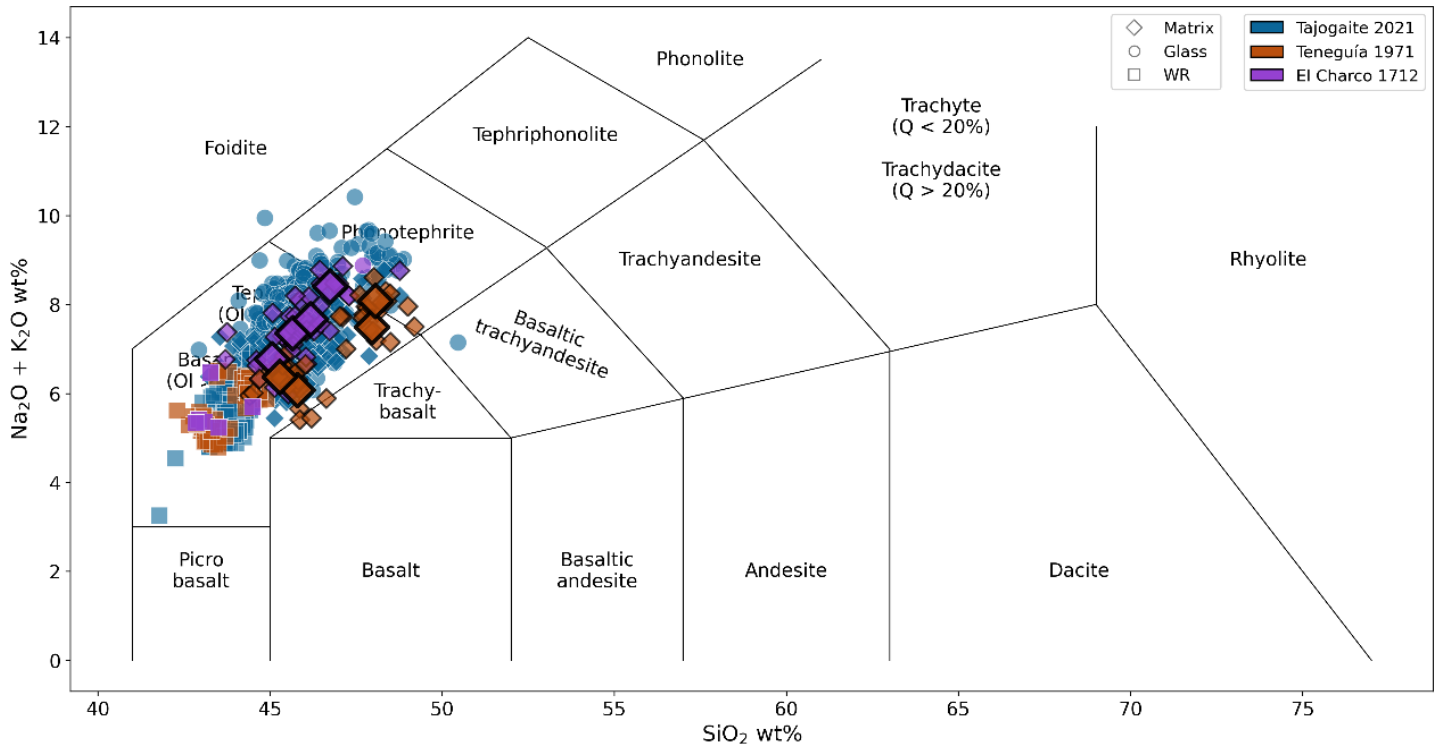
Fig. S17. TAS diagram. TAS diagram showing the matrix compositions studied in this work, compared with literature data. Large diamonds for Teneguía 1971 and El Charco 1712 represent the average matrix compositions based on 10 analyses from this study. Matrix data for Tajogaite 2021 are from Ubide et al. (2023). Whole-rock (WR) data for Tajogaite 2021 are from Day et al. (2022), Pankhurst et al. (2022) and Ubide et al. (2023). WR data for El Charco 1712 (Carracedo et al., 2001; Day et al., 2010; Hernandez-Pacheco and Valls, 1982; Turner et al., 2015) and Teneguía 1971 (Barker et al., 2015; Carracedo et al., 2001; Ibarrola, 1974; Lundstrom et al., 2003; Turner et al., 2015; Weis et al., 2015) were retrieved from the GEOROC database.
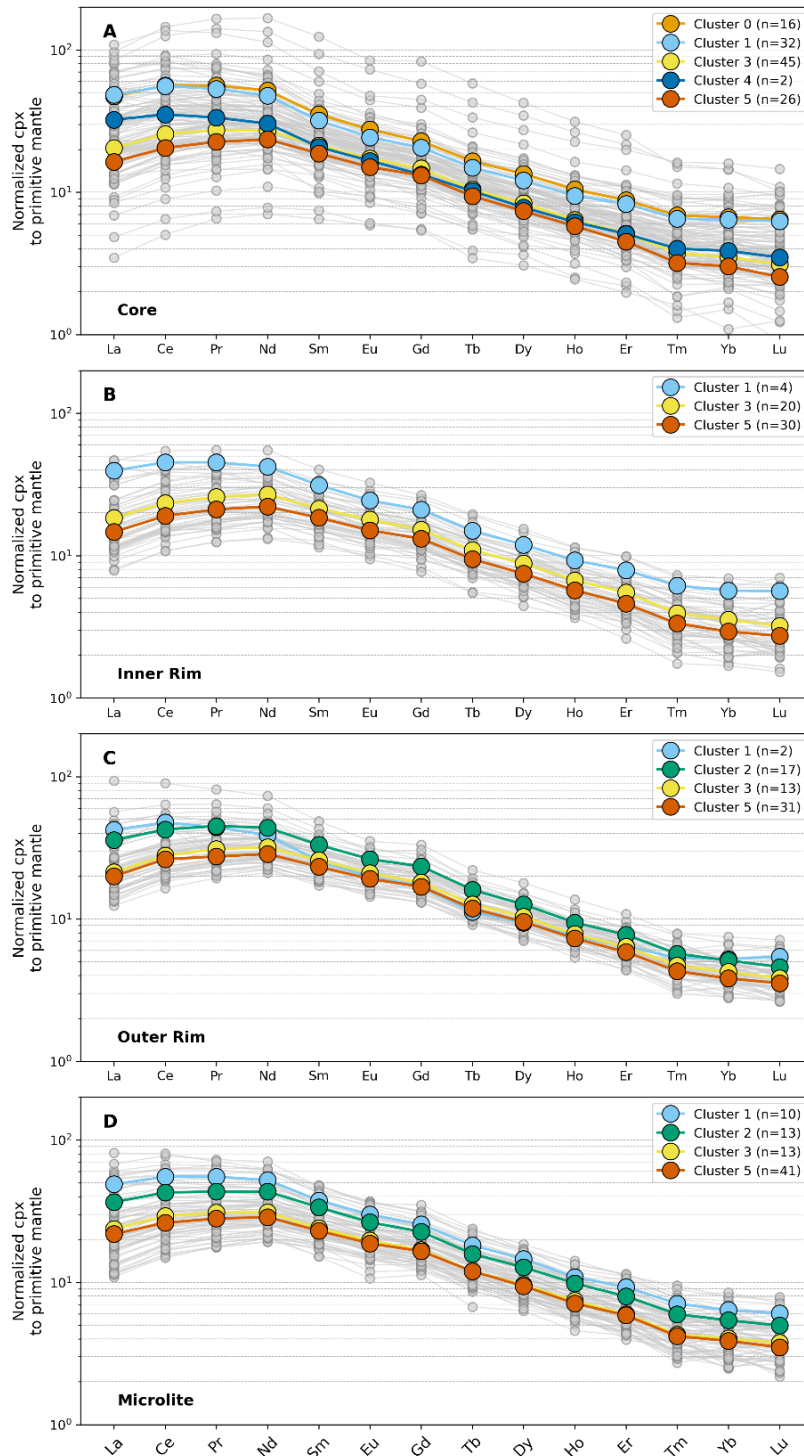
5. Clustering results

Fig. S18. Cluster-colored cpx REE patterns. Trace element patterns are color-coded based on clusters. Grey lines and points represent individual measurements, while colored lines show the average for each cluster group. Each panel corresponds to a specific textural position: (A) core (B) inner rim (C) outer rim and (D) microlite.
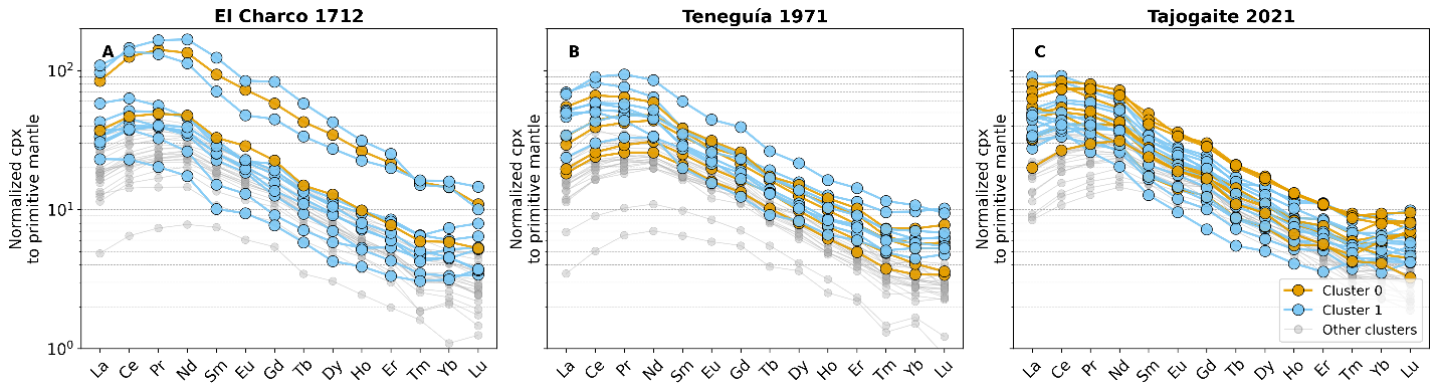

Fig. S19. Evolved cpx REE patterns. Trace element pattern of evolved clinopyroxene cores belonging to Cluster 0 and 1. These compositions are the most differentiated, with patterns showing an enrichment in heavy REE elements Tm, Yb and Lu, typical of phonolite-derived compositions. Grey lines represent patterns of clinopyroxenes belonging to Cluster 2, 3, 4 and 5.

24
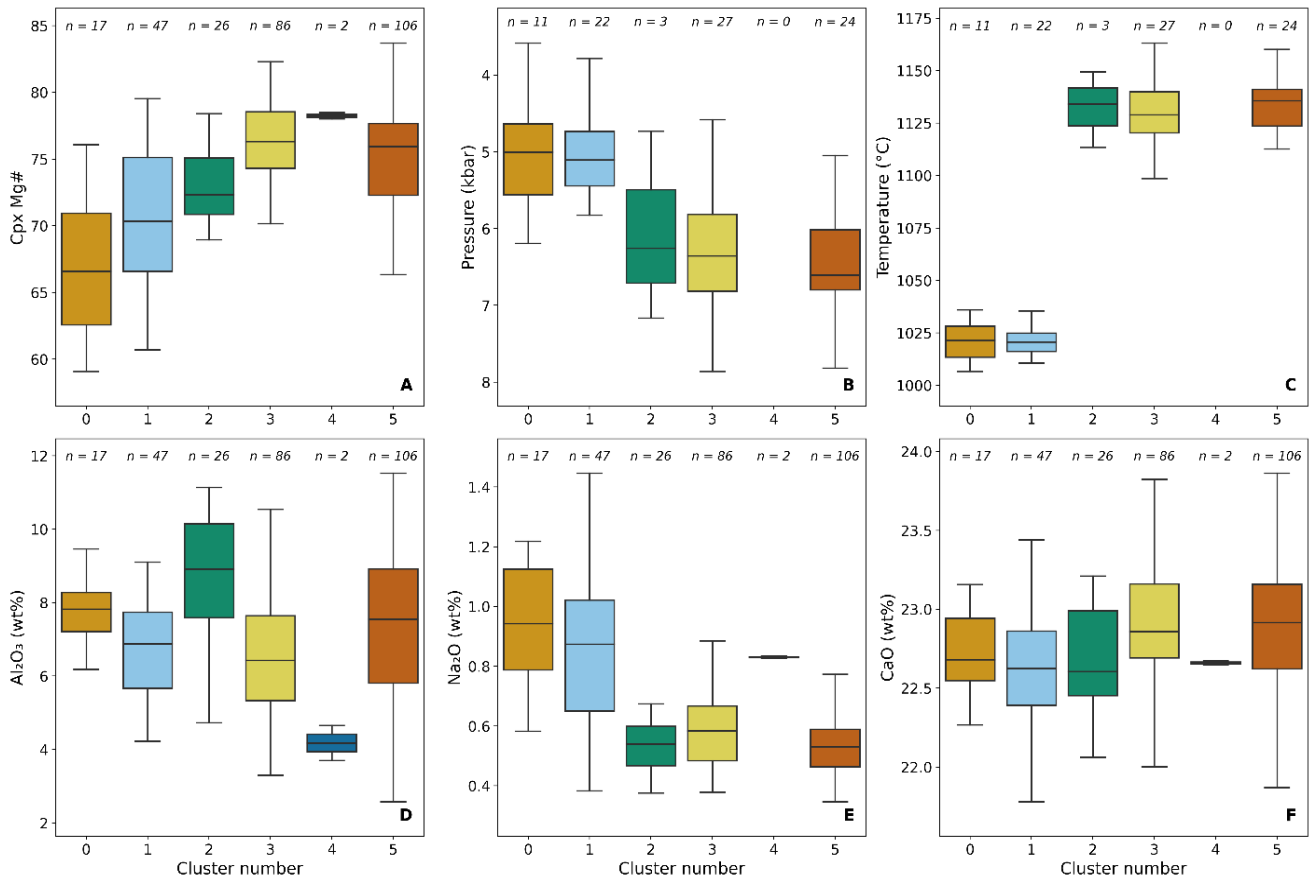
Fig. S20. Cluster-colored cpx composition, P and T. Box plots show the distribution of clinopyroxene (A) Mg# for each cluster. Panels (B) and (C) show clinopyroxene–melt equilibrium pressures and temperatures, respectively, for each cluster. Only data that passed the equilibrium criteria following the approach of MacDonald et al. (2023) are included, as described in the method section. (D-F) Distribution of Al_2O_3, Na_2O and CaO for each cluster. In this figure, only analyses with both EMPA and LA-ICP-MS single-spot data are plotted.

6. Equilibrium melt composition and trace elements modelling

We reconstructed the trace element melt composition in equilibrium with each measured clinopyroxene trace element composition to compare these with the trace element composition of the matrix, interpreted here as representative of the carrier melt, and to model fractional crystallization (FC).

Equilibrium melt compositions were calculated using partition coefficients (KDs) derived from multiple parametrizations published in Bédard (2014). Specifically, for each element, we applied several parameterizations calibrated for terrestrial systems (TE), mafic terrestrial systems (MTS), and low-pressure MTS as reported in Bédard (2014). The resulting KDs were averaged, and uncertainties were estimated based on the 1σ variability across parameterizations. Using these fixed KDs for each trace element, we reconstructed the equilibrium melt composition for each clinopyroxene, incorporating the uncertainty from the different parameterizations. Overall, the calculated KDs are of the same order of magnitude as those reported for alkali basalts in the GERM database.

Fractional crystallization was modeled starting from a primitive matrix composition, obtained by averaging the least differentiated matrix compositions with Zr concentrations between 300–330 ppm. The crystal assemblage was set following Ubide et al. (2023) to reflect the average assemblage observed in natural products (64% clinopyroxene, 28% olivine, 2% oxides, and 6% plagioclase). For clinopyroxenes, we used a fixed Kd for each trace element, calculated as the median of individual values estimated from the Bédard (2014) parameterizations described above. For the other mineral phases, Kd values were taken from the GERM database for alkali basalts. Specifically, Kds for amphibole and olivine are from Adam and Green (2006); for plagioclase, from Schnetzler and Philpotts (1970) and Villemant et al. (1981); and for oxides, from Elkins et al. (2008) and McKenzie and O'nions (1991).
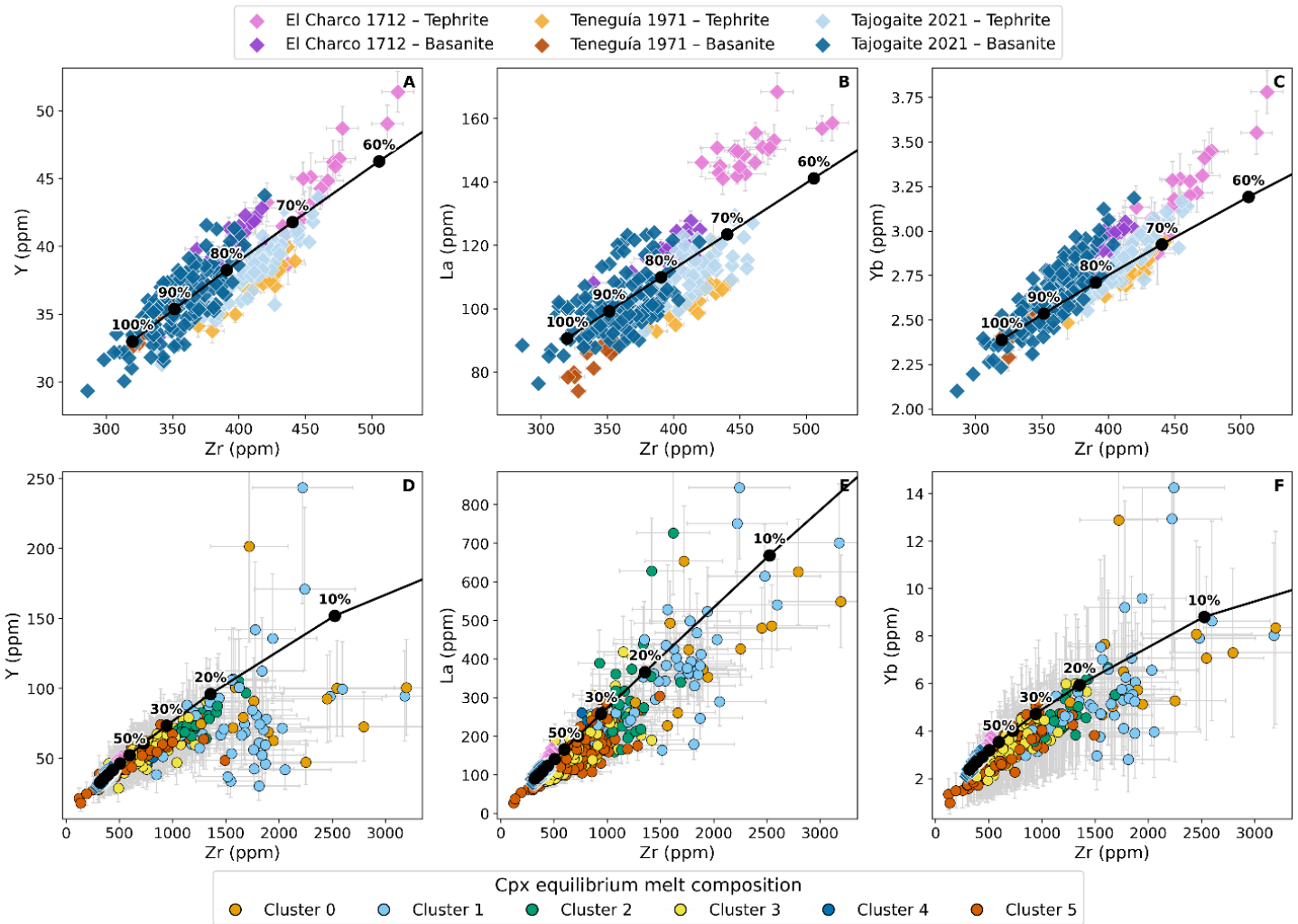
Fig. S21. Equilibrium melt composition and FC model. (A–C) Trace element composition of the matrix and FC results. Each black filled circle represents 10% increments of fractionation starting from 100% melt phase. Note that the tephrite compositions for each eruption can be reproduced by ~10% fractionation from a basanite composition of the same eruption. (D–F) Reconstructed clinopyroxene equilibrium melt compositions, colored according to clustering. The black line represents the FC model. Note that Clusters 0 and 1 compositions are consistent with 80–90% fractionation.
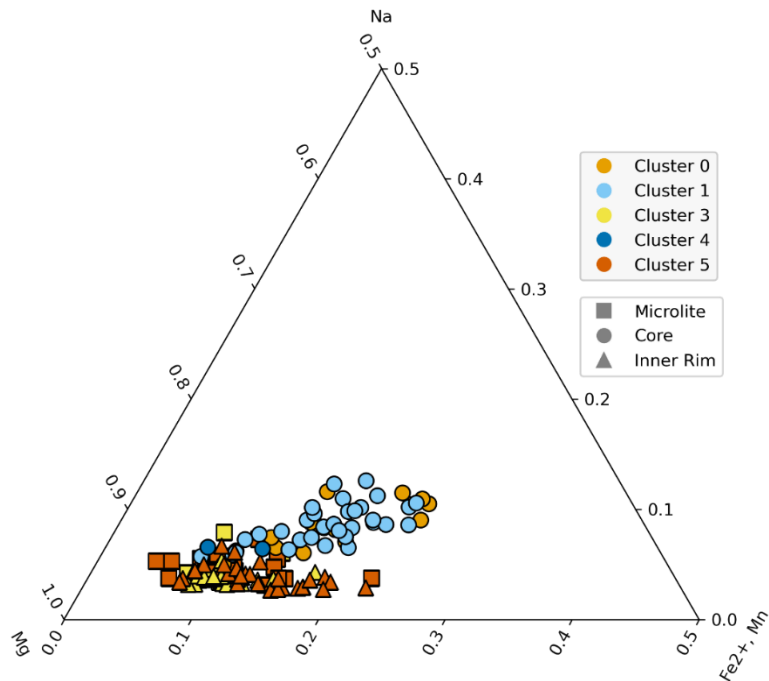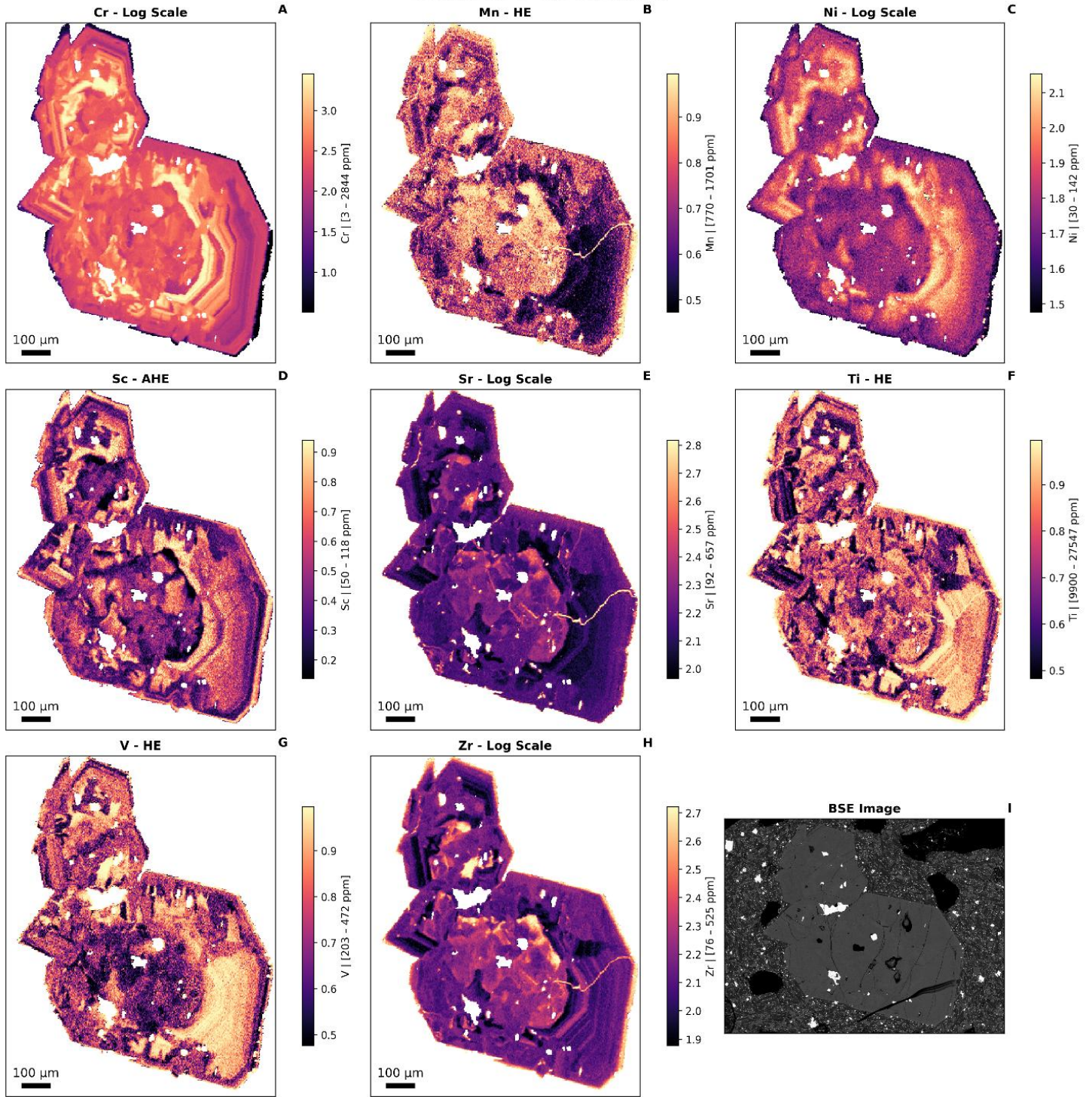
Fig. S22. Mg–Fe²⁺(+Mn)–Na Cpx classification. Clinopyroxene compositions are plotted on the Mg–Fe²⁺(+Mn)–Na atoms per formula unit diagram after Larsen (1976). We show Cluster 0 and 1 core compositions, Cluster 4 core compositions (n=2), and Cluster 3 and 5 inner rim and microlite compositions to compare evolutionary trends of the phonolite-derived (Clusters 0 and 1) and tephrite–basanite (Clusters 3 and 5) recharge compositions relative to Cluster 4. Notably, Clusters 0 and 1 cores define a distinct lineage from the Cluster 3 and 5 recharge compositions, while Cluster 4 lies at the beginning of the phonolite lineage, potentially representing a composition capable of evolving into phonolitic melts. Cluster 2 compositions are not included in this plot as they are related to magma ascent and surface cooling.
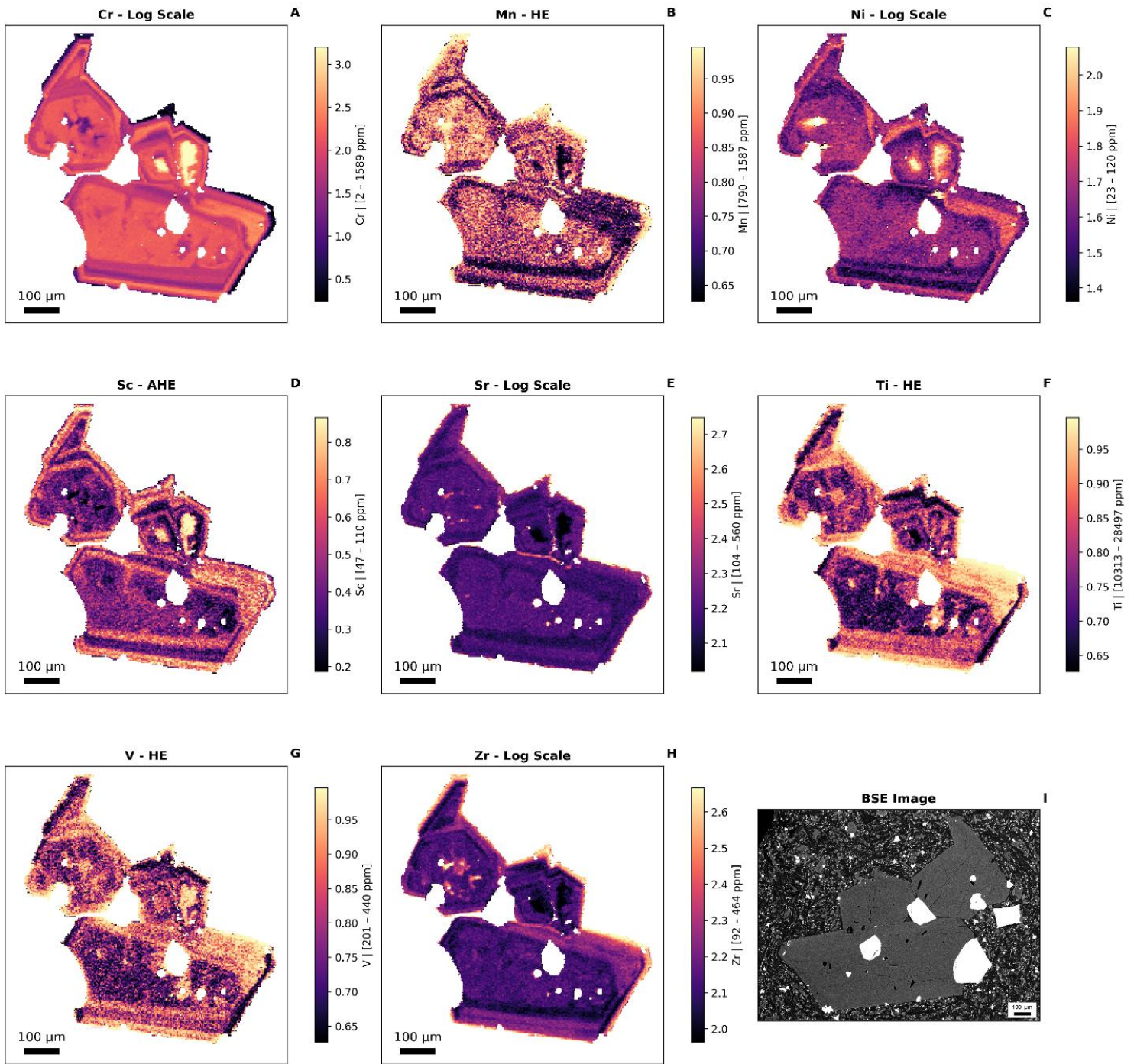
7. Clinopyroxene trace element maps

Fig. S23. LA-ICP-MS chemical maps. We present 15 figures of clinopyroxene trace element maps for Cr, Mn, Ni, Sc, Sr, Ti, V, and Zr. For each element and each sample, the optimal visualization method, either logarithmic scaling, histogram equalization (HE), or adaptive histogram equalization (AHE), was selected and is indicated at the top of each panel (Panels A–H). Note that colors are not comparable between images, as this approach is designed to enhance zoning contrast within each map. The quantitative range for each element (in ppm) is shown in the title of each color bar. In each figure, Panel I displays the BSE image of the mapped area. BSE images were acquired after crystal mapping and gentle repolishing, which may result in minor differences between the crystals shown in the trace element maps and those in the BSE image. The eruption, clinopyroxene name, and rock type (basanite or tephrite) are indicated at the top of each figure.
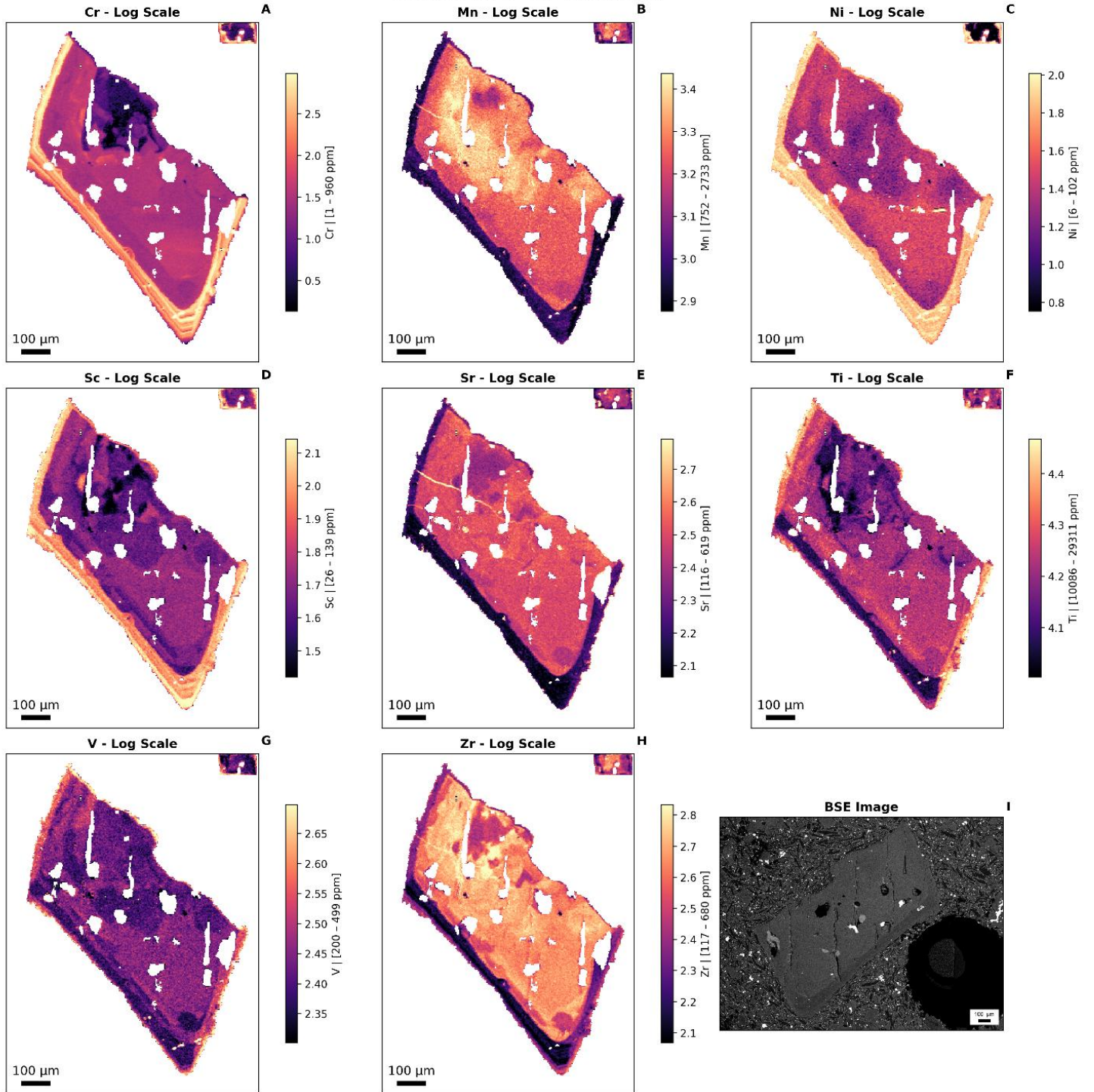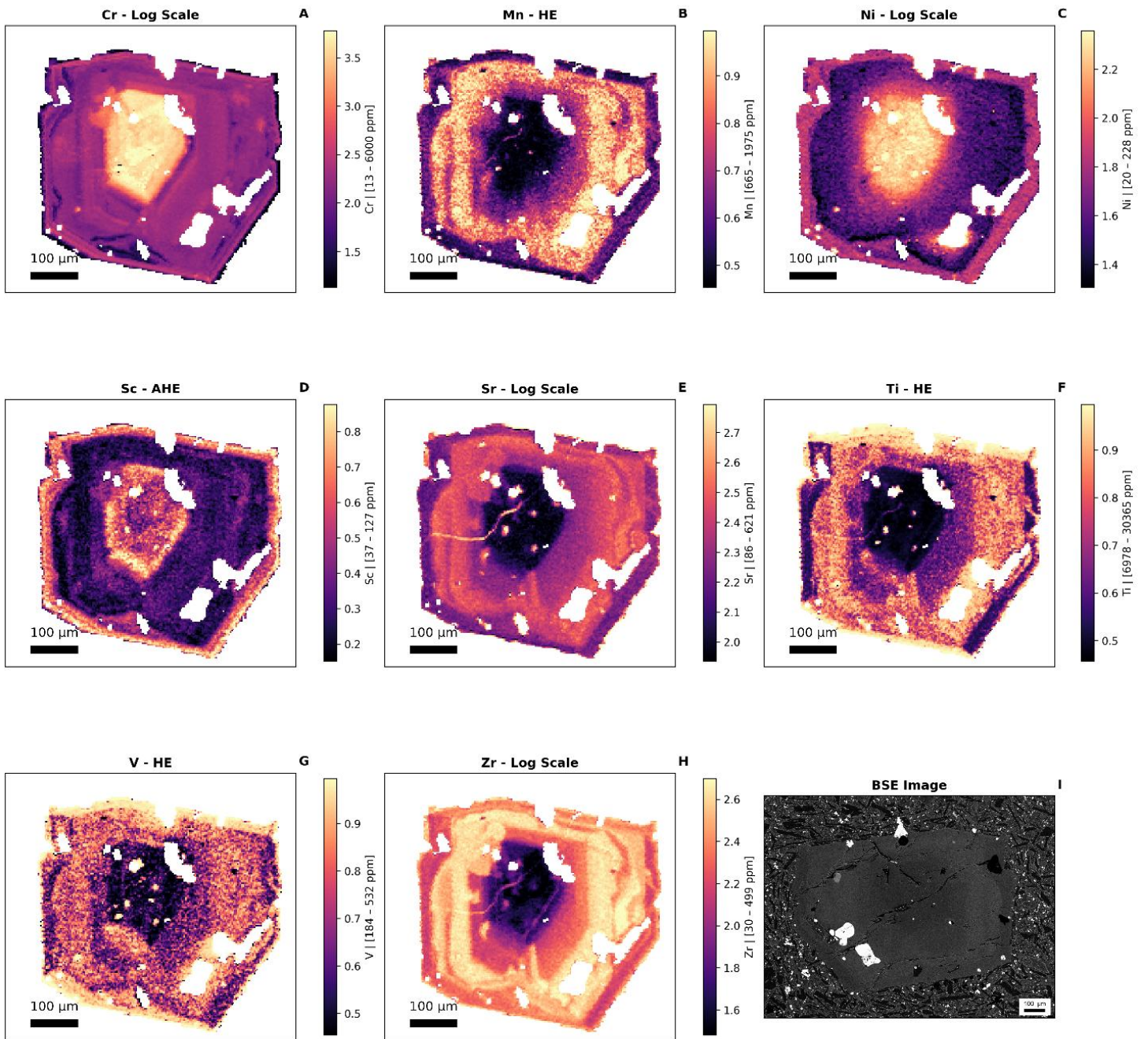
Teneguía 1971 – Cpx 4 (Tephrite)
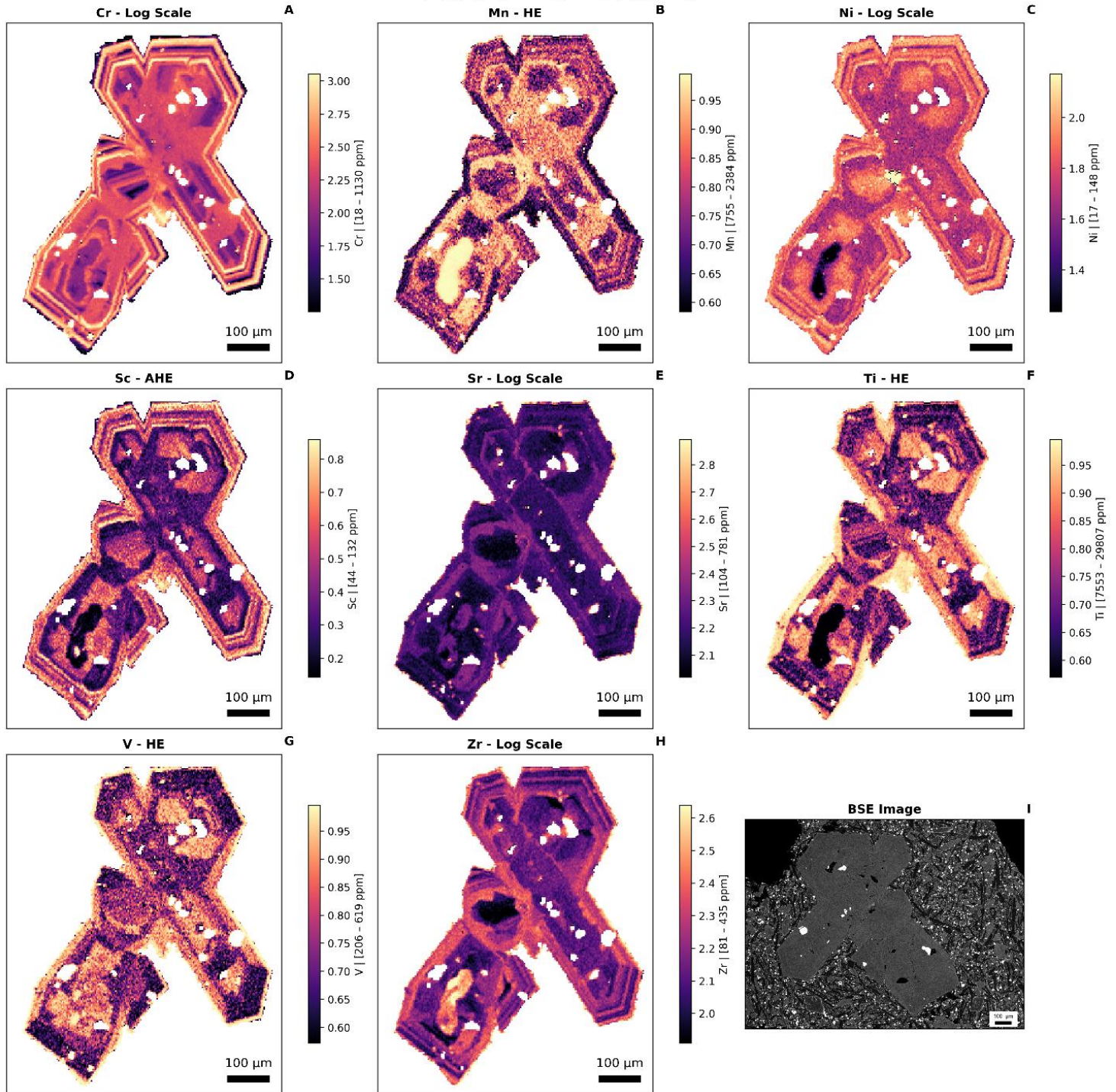

29

Teneguía 1971 – Cpx 3-5 (Tephrite)

Cr - Log Scale · A
Mn - HE · B
Ni - Log Scale · C
Sc - AHE · D
Sr - Log Scale · E
Ti - HE · F
V - HE · G
Zr - Log Scale · H
BSE Image · I

Teneguía 1971 – Cpx 1 (Basanite)

Teneguía 1971 – Cpx 3 (Basanite)

A Cr - Log Scale

B Mn - HE

C Ni - Log Scale

D Sc - AHE

E Sr - Log Scale

F Ti - HE

G V - HE

H Zr - Log Scale

I BSE Image

Teneguía 1971 – Cpx 2-5 (Basanite)

A Cr - Log Scale

B Mn - HE

C Ni - Log Scale

D Sc - AHE

E Sr - Log Scale

F Ti - HE

G V - HE

H Zr - Log Scale

I BSE Image

El Charco 1712 – Cpx 12 (Tephrite)

A — Cr - Log Scale
B — Mn - Log Scale
C — Ni - Log Scale
D — Sc - AHE
E — Sr - Log Scale
F — Ti - Log Scale
G — V - Log Scale
H — Zr - Log Scale
I — BSE Image

El Charco 1712 – Cpx 13 (Basanite)

El Charco 1712 – Cpx 1-2 (Tephrite)

A Cr - Log Scale

B Mn - HE

C Ni - Log Scale

D Sc - AHE

E Sr - Log Scale

F Ti - HE

G V - HE

H Zr - Log Scale

I BSE Image

36
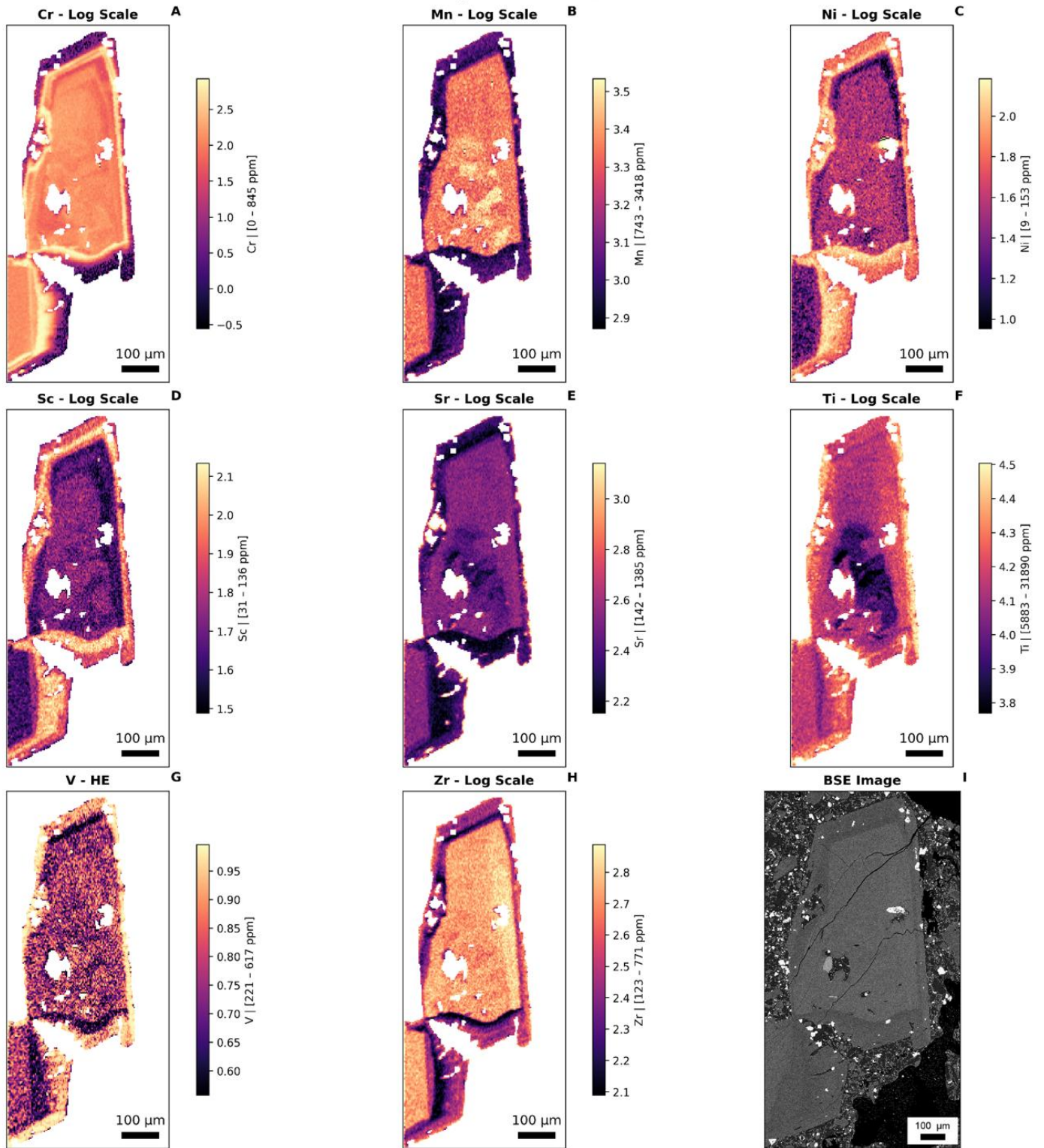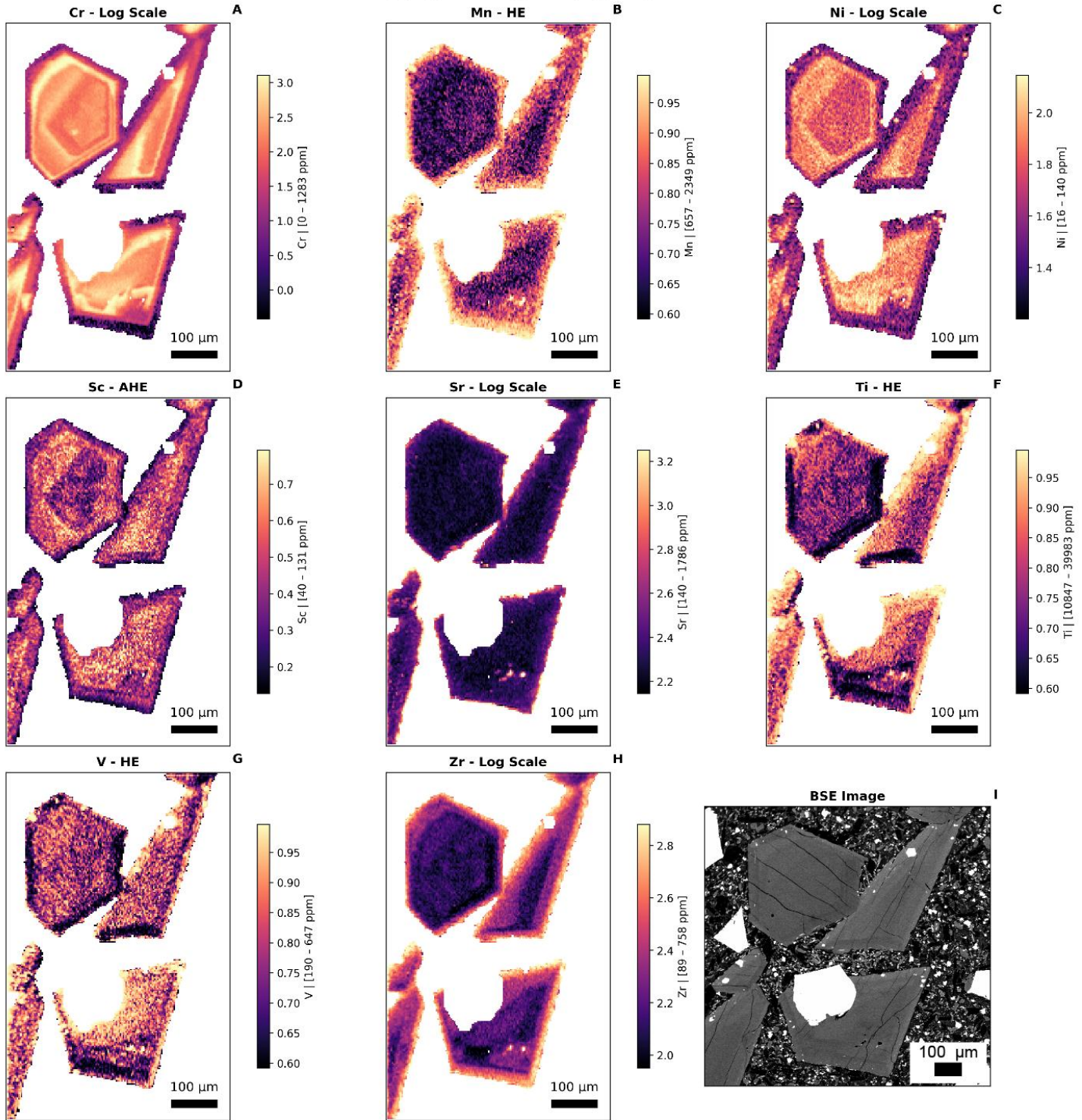
El Charco 1712 – Cpx 21 (Basanite)

A Cr - Log Scale

B Mn - Log Scale

C Ni - Log Scale

D Sc - Log Scale

E Sr - Log Scale

F Ti - Log Scale

G V - Log Scale
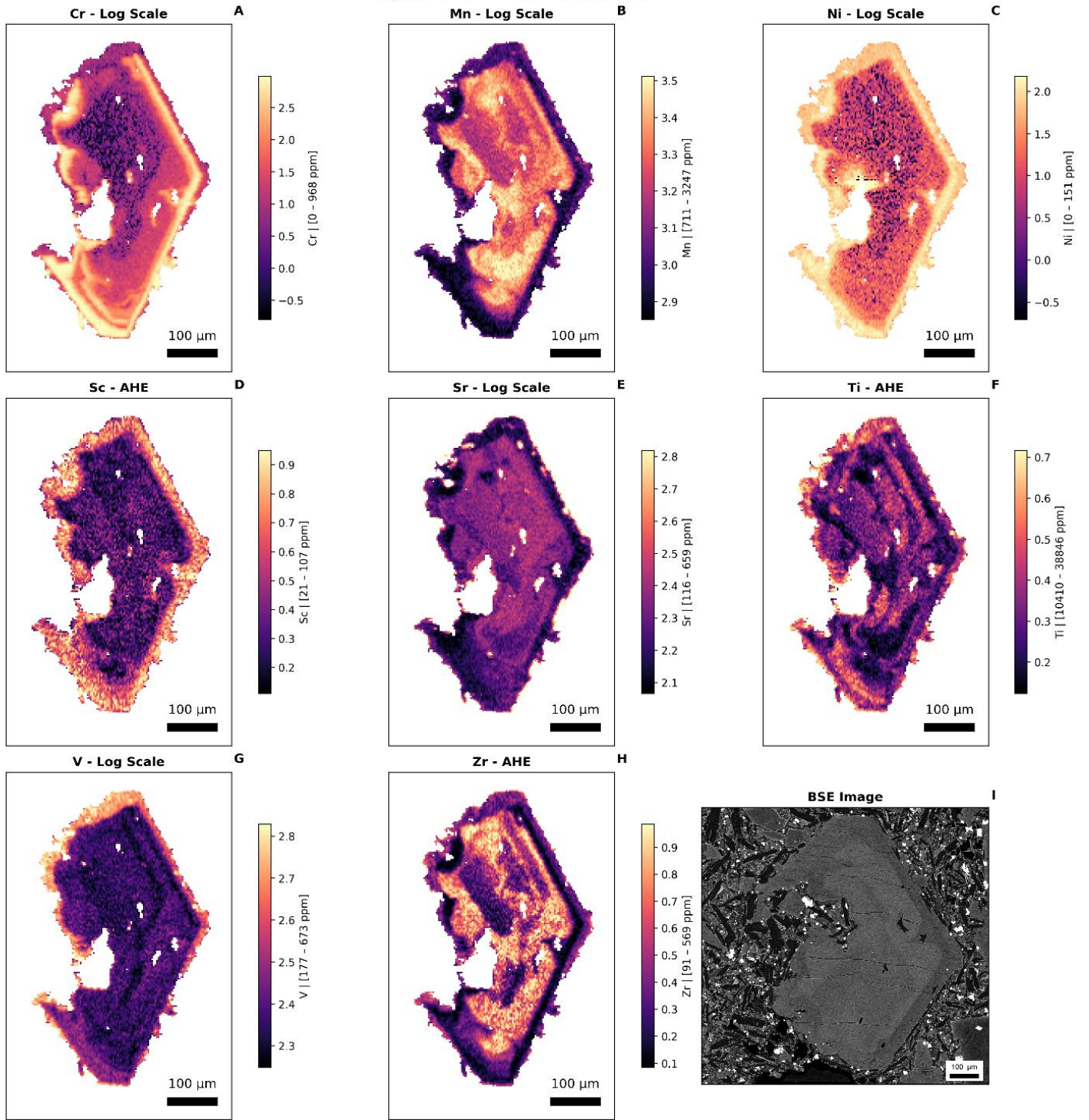
H Zr - Log Scale

I BSE Image
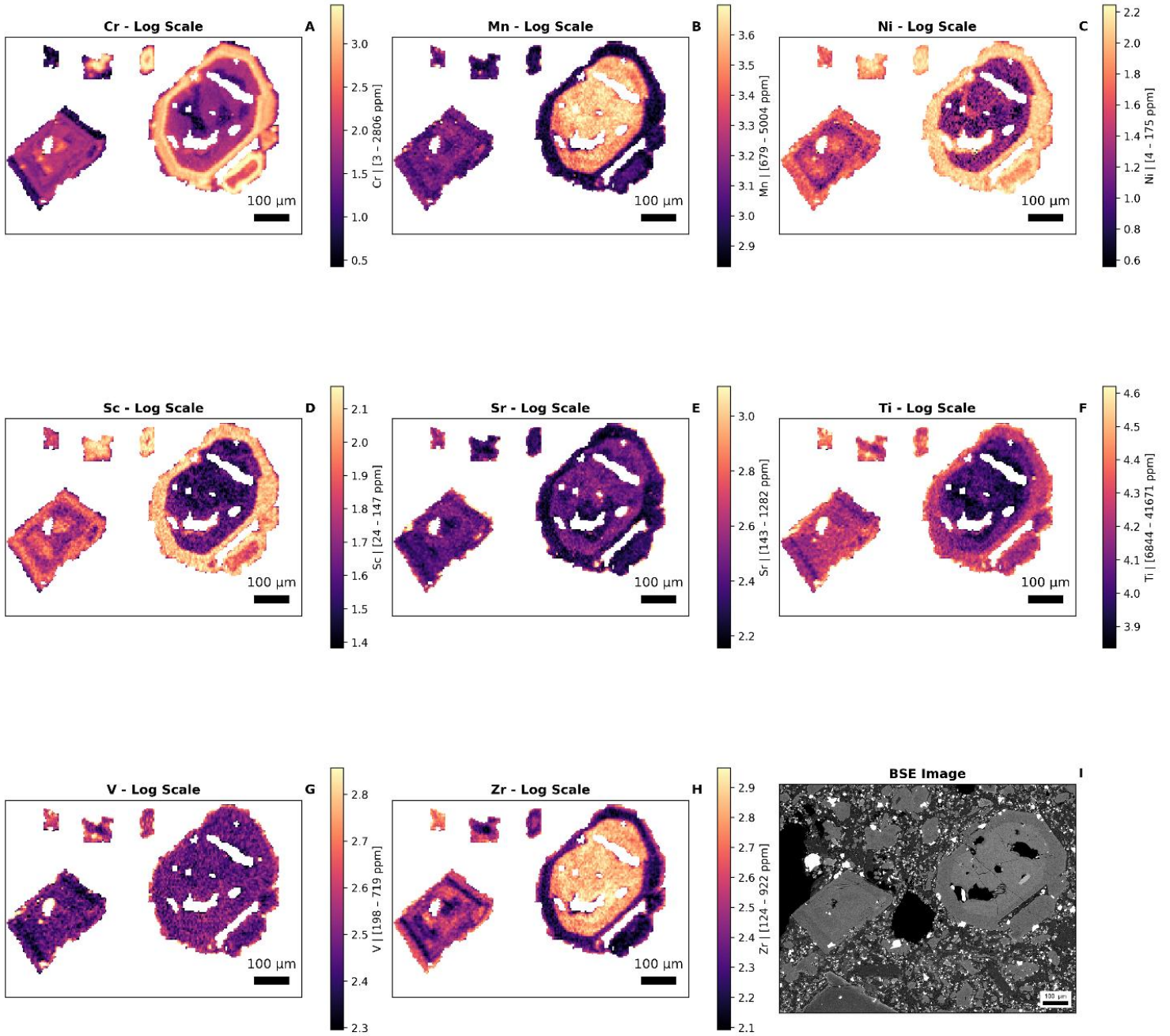
El Charco 1712 – Cpx 22 (Basanite)
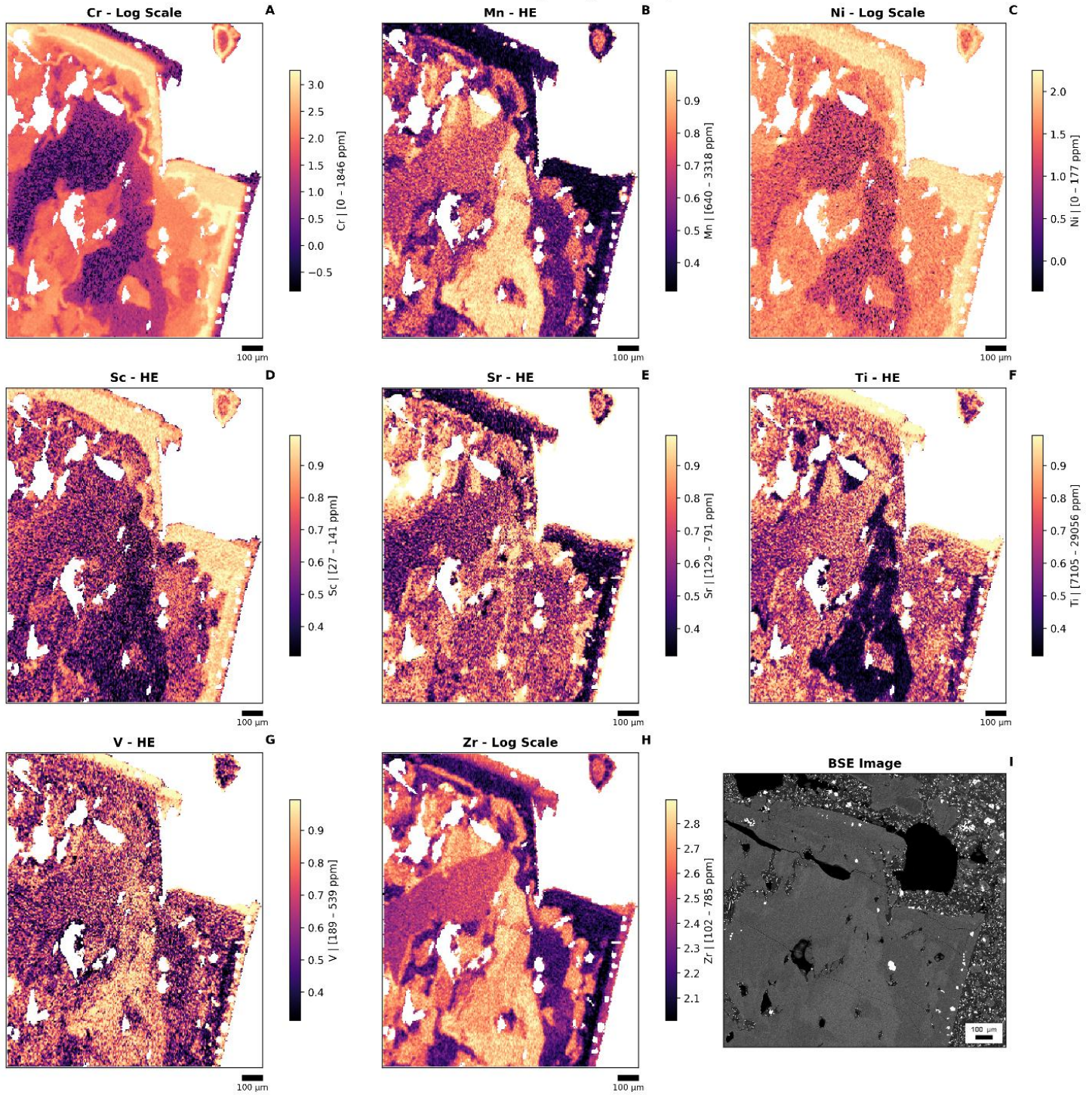
Tajogaite 2021 – Cpx 3 (Tephrite)

39
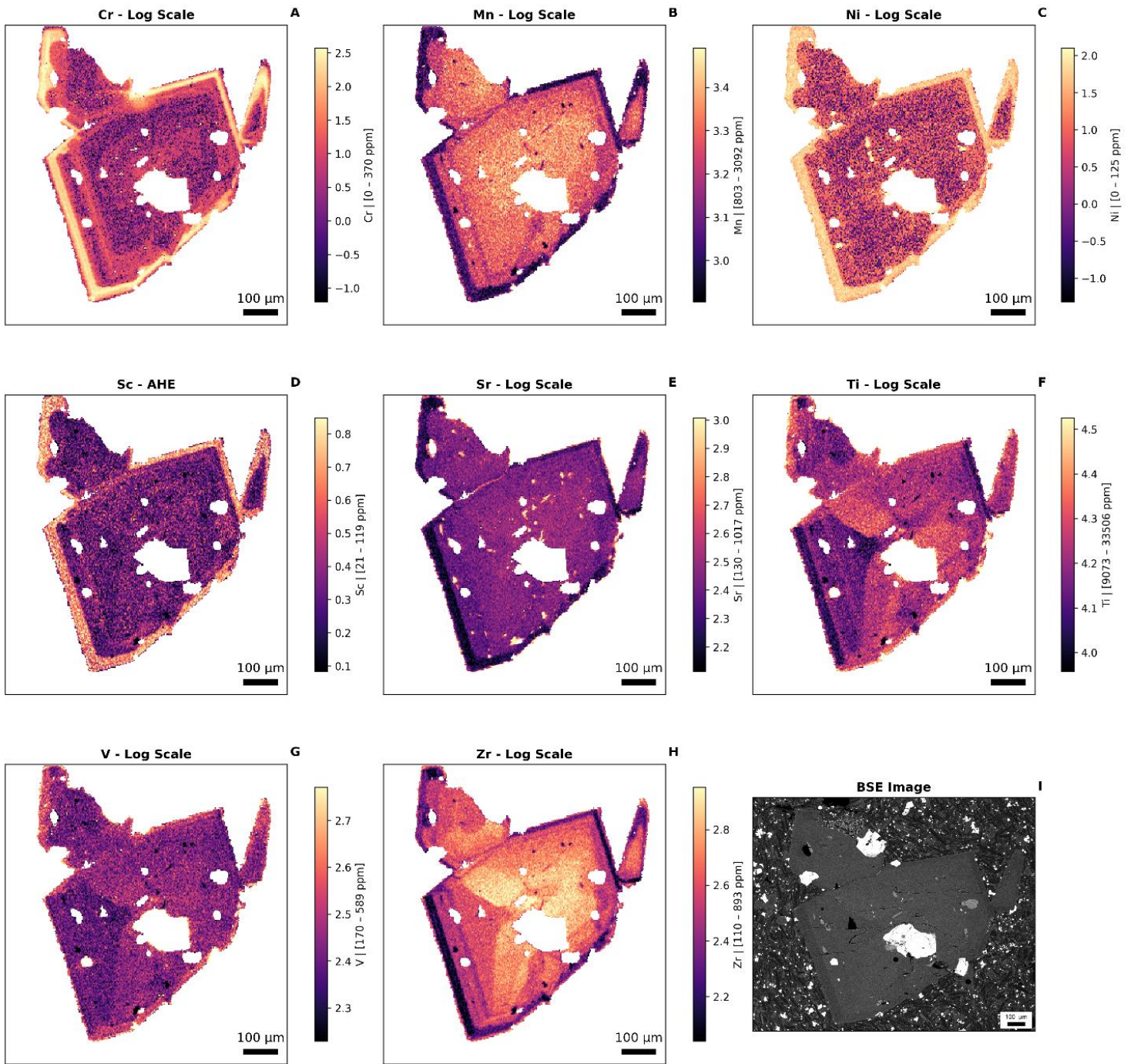
Tajogaite 2021 – Cpx 2 (Basanite)

A — Cr - Log Scale — Cr | [0 – 968 ppm]

B — Mn - Log Scale — Mn | [711 – 3247 ppm]

C — Ni - Log Scale — Ni | [0 – 151 ppm]

D — Sc - AHE — Sc | [21 – 107 ppm]

E — Sr - Log Scale — Sr | [116 – 659 ppm]

F — Ti - AHE — Ti | [10410 – 38846 ppm]

G — V - Log Scale — V | [177 – 673 ppm]

H — Zr - AHE — Zr | [91 – 569 ppm]

I — BSE Image
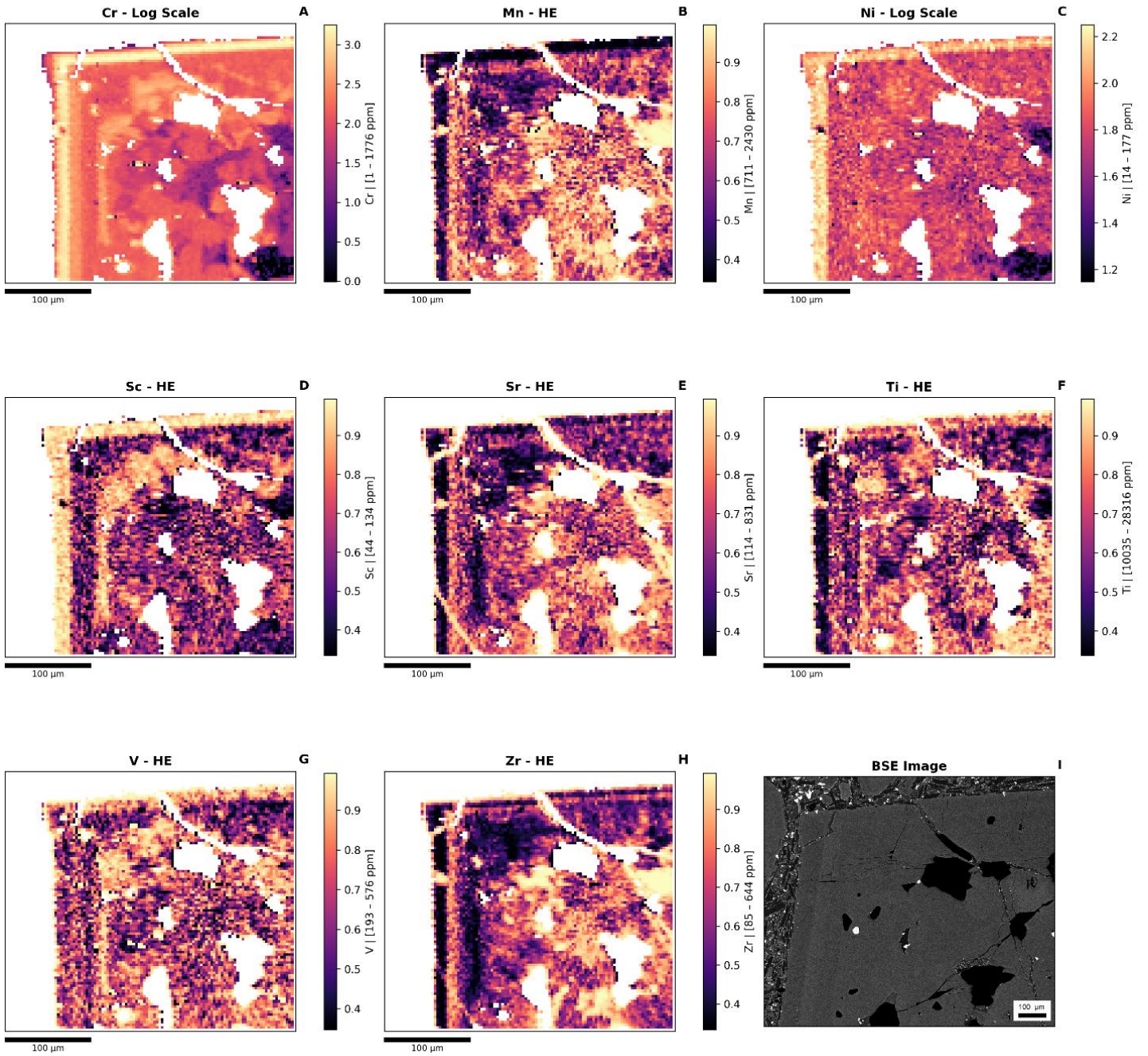
Tajogaite 2021 – Cpx 4 (Basanite)
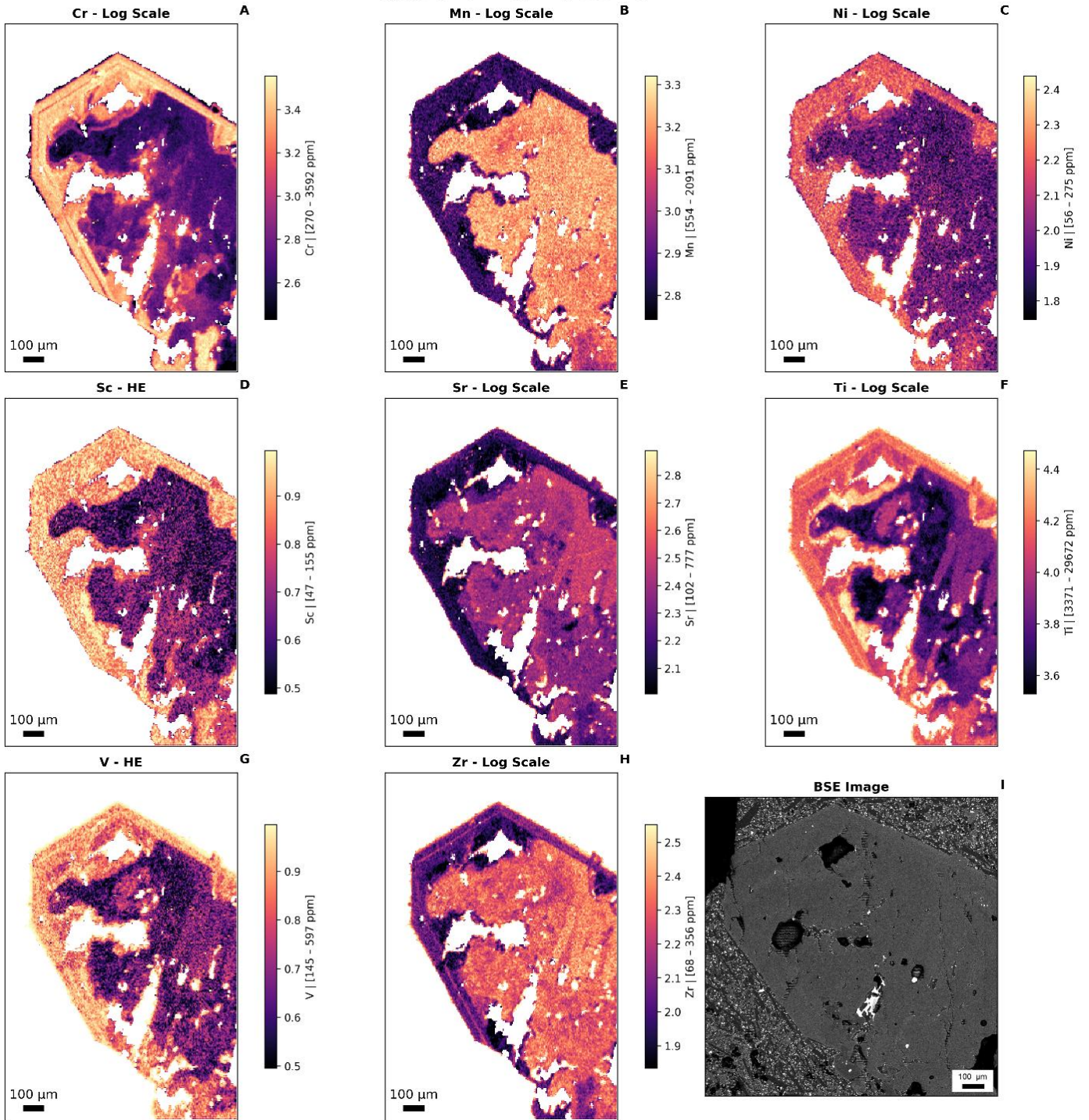
Tajogaite 2021 – Cpx 5 (Basanite)

42
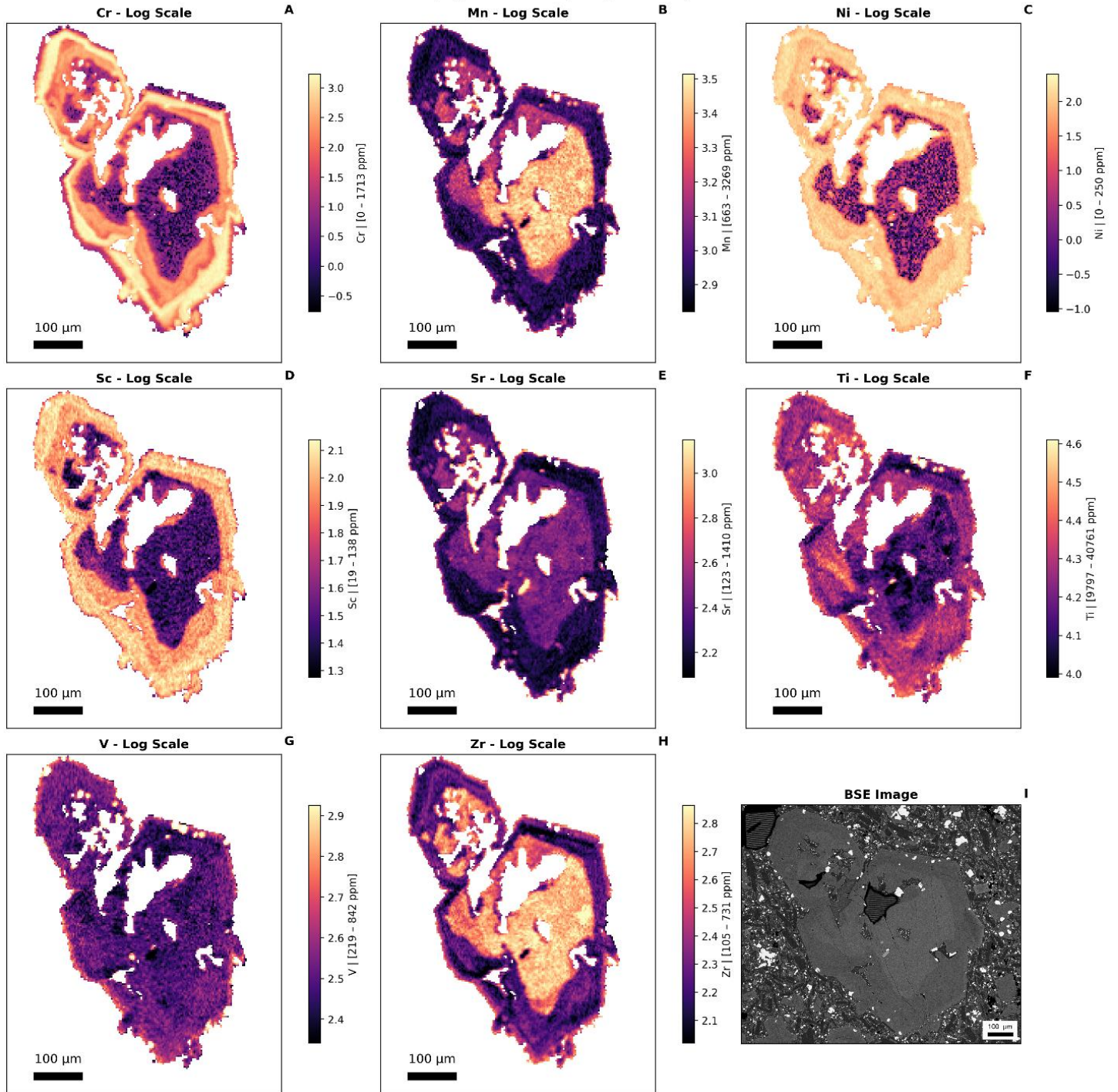
Tajogaite 2021 – Cpx 0 (Basanite)

8.Supplementary references

Adam, J., Green, T., 2006. Trace element partitioning between mica-and amphibole-bearing garnet lherzolite and hydrous basanitic melt: 1. Experimental results and the investigation of controls on partitioning behaviour. Contributions to Mineralogy and Petrology 152, 1–17.

Afonso, A., Aparicio, A., Hernández-Pacheco, A., Badiola, E.R., 1974. Morphology evolution of Teneguía volcano area. Estudios Geológicos, Vol. Teneguía 19–26.

Ágreda-López, M., Musu, A., Jorgenson, C., Šala, M., Giordano, G., Caricchi, L., Stremtan, C., Petrelli, M., 2025. The crystal cargo provides a chronicle of pre-caldera dynamics in mafic volcanic systems: insights from Colli Albani. Bull Volcanol 87. https://doi.org/10.1007/s00445-025-01865-6

Andújar, J., Scaillet, B., Frascerra, D., Di Carlo, I., Casillas, R., Suárez, E.D., Domínguez-Cerdeña, I., Meletlidis, S., López, C., Slodczyk, A., Martí, J., Núñez-Guerrero, E., 2025. Evolution of the crustal reservoir feeding La Palma 2021 eruption. Insights from phase equilibrium experiments and petrologically derived time scales. Journal of Volcanology and Geothermal Research 463. https://doi.org/10.1016/j.jvolgeores.2025.108327

Anguita, F., Fernández, C., Márquez, Á., León, R., Casillas, R., 2025. The Canary hotspot revisited: Refutation of the Hawaii paradigm and an alternative, plate-based hypothesis. Earth Sci Rev. https://doi.org/10.1016/j.earscirev.2024.105038

Barker, A.K., Troll, V.R., Carracedo, J.C., Nicholls, P.A., 2015. The magma plumbing system for the 1971 Teneguía eruption on La Palma, Canary Islands. Contributions to Mineralogy and Petrology 170, 1–21. https://doi.org/10.1007/s00410-015-1207-7

Bonechi, B., Polacci, M., Arzilli, F., Romero, J.E., Fellowes, J., Burton, M., 2024. Magma residence time, ascent rate and eruptive style of the November ash-laden activity during the 2021 Tajogaite eruption (La Palma, Spain). Volcanica 7, 51–65. https://doi.org/10.30909/vol.07.01.5165

Carracedo, J.C., Badiola, E.R., Guillou, H., De La Nuez, J., Pérez-Torrado, F.J., 2001. Geology and volcanology of La Palma and El Hierro, Western Canaries. Estudios Geológicos 57, 175–273.

Carracedo, J.C., Troll, V.R., Day, J.M.D., Geiger, H., Aulinas, M., Soler, V., Deegan, F.M., Pérez-Torrado, F.J., Gisbert, G., Gazel, E., Rodríguez-González, A., Albert, H., 2022. The 2021 eruption of the Cumbre Vieja volcanic ridge on La Palma, Canary Islands. Geology Today 38, 94–107. https://doi.org/10.1111/gto.12388

Chamberlain, K.J., Pankhurst, M., Neave, D., Morgan, D., Barbee, O., Scarrow, J., Hickey, J., Broom-Fendley, S., Gardner, J., Rollinson, G., Walshaw, R., Stewart, A., Wieser, P., Coldwell, B., Martín-Lorenzo, A., Rodríguez, F., 2025. Crystal cargo perspectives on magma assembly and dynamics

during the 2021 Tajogaite eruption, La Palma, Canary Islands. Volcanica 8, 399–425. https://doi.org/10.30909/vol/vujv5852

Chicharro Fermín, N., 2024. La erupción de El Charco de 1712, La Palma. Características petrológicas e implicaciones en la peligrosidad volcánica. Universidad Complutense de Madrid. https://doi.org/https://docta.ucm.es/entities/publication/b8280

D'Auria, L., Koulakov, I., Prudencio, J., Cabrera-Pérez, I., Ibáñez, J.M., Barrancos, J., García-Hernández, R., Martínez van Dorth, D., Padilla, G.D., Przeor, M., Ortega, V., Hernández, P., Peréz, N.M., 2022. Rapid magma ascent beneath La Palma revealed by seismic tomography. Sci Rep 12. https://doi.org/10.1038/s41598-022-21818-9

Day, J.M.D., Pearson, D.G., Macpherson, C.G., Lowry, D., Carracedo, J.C., 2010. Evidence for distinct proportions of subducted oceanic crust and lithosphere in HIMU-type mantle beneath El Hierro and La Palma, Canary Islands. Geochim Cosmochim Acta 74, 6565–6589. https://doi.org/10.1016/j.gca.2010.08.021

Day, J.M.D., Troll, V.R., Aulinas, M., Deegan, F.M., Geiger, H., Carracedo, J.C., Pinto, G.G., Pérez-Torrado, F.J., 2022. Mantle source characteristics and magmatic processes during the 2021 La Palma eruption. Earth Planet Sci Lett 597. https://doi.org/10.1016/j.epsl.2022.117793

Dayton, K., Gazel, E., Wieser, P., Troll, V.R., Carracedo, J.C., Madrid, H. La, Roman, D.C., Ward, J., Aulinas, M., Geiger, H., Deegan, F.M., Gisbert, G., Pérez-Torrado, F.J., 2023. Deep magma storage during the 2021 La Palma eruption. Sci Adv 9, 1–8. https://doi.org/10.1126/sciadv.ade7641

Elkins, L.J., Gaetani, G.A., Sims, K.W.W., 2008. Partitioning of U and Th during garnet pyroxenite partial melting: Constraints on the source of alkaline ocean island basalts. Earth Planet Sci Lett 265, 270–286.

Fabbrizio, A., Bamber, E.C., Michailidou, E., Romero, J.E., Arzilli, F., Bonechi, B., Polacci, M., Burton, M., 2023. Phase equilibrium experiments and thermodynamic simulations to constrain the pre-eruptive conditions of the 2021 Tajogaite eruption (Cumbre Vieja volcano, La Palma, Canary Islands). Journal of Volcanology and Geothermal Research 442. https://doi.org/10.1016/j.jvolgeores.2023.107901

Fernández, J., Escayo, J., Hu, Z., Camacho, A.G., Samsonov, S. V., Prieto, J.F., Tiampo, K.F., Palano, M., Mallorquí, J.J., Ancochea, E., 2021. Detection of volcanic unrest onset in La Palma, Canary Islands, evolution and implications. Sci Rep 11. https://doi.org/10.1038/s41598-021-82292-3

González-García, D., Boulesteix, T., Klügel, A., Holtz, F., 2023. Bubble-enhanced basanite–tephrite mixing in the early stages of the Cumbre Vieja 2021 eruption, La Palma, Canary Islands. Sci Rep 13. https://doi.org/10.1038/s41598-023-41595-3

Hernandez-Pacheco, A., Valls, M.C., 1984. The historic eruptions of La Palma Island (Canaries). Arquipélago. Série Ciências da Natureza 83–94.

Hernandez-Pacheco, A., Valls, M.C., 1982. The historic eruptions of La Palma Island (Canaries). Arquipélago. Série Ciências da Natureza.

Ibarrola, E., 1974. Temporal modification of the basaltic materials from the 1971 eruption of the Teneguía volcano (La Palma, Canary Islands). Estudios Geológicos 49–58.

Jegal, Y., Ubide, T., Huertas, M.J., Herrera, R., Márquez, Á., Ancochea, E., Coello-Bravo, J.J., 2025. Plagioclase antecrysts record syn-eruptive incorporation of evolved mush during the 2021 Tajogaite eruption (La Palma, Spain). Contributions to Mineralogy and Petrology 180. https://doi.org/10.1007/s00410-025-02241-5

Klügel, A., Albers, E., Hansteen, T.H., 2022. Mantle and Crustal Xenoliths in a Tephriphonolite From La Palma (Canary Islands): Implications for Phonolite Formation at Oceanic Island Volcanoes. Front Earth Sci (Lausanne) 10. https://doi.org/10.3389/feart.2022.761902

Klügel, A., Hansteen, T.H., Galipp, K., 2005. Magma storage and underplating beneath Cumbre Vieja volcano, La Palma (Canary Islands). Earth Planet Sci Lett 236, 211–226. https://doi.org/10.1016/j.epsl.2005.04.006

Klugel, A., Schmincke, H.-U., White, J.D.L., Hoernle, K.A., 1999. Chronology and volcanology of the 1949 multi-vent rift-zone ž / eruption on La Palma Canary Islands, Journal of Volcanology and Geothermal Research.

Larsen, M.L., 1976. Clinopyroxenes and Coexisting Mafic Minerals from the Alkaline Dimaussaq Intrusion, South Greenland 17, 258–290.

Longpré, M.A., Felpeto, A., 2021. Historical volcanism in the Canary Islands; part 1: A review of precursory and eruptive activity, eruption parameter estimates, and implications for hazard assessment. Journal of Volcanology and Geothermal Research 419. https://doi.org/10.1016/j.jvolgeores.2021.107363

Longpré, M.A., Tramontano, S., Pankhurst, M.J., Roman, D.C., Reiss, M.C., Cortese, F., James, M.R., Spina, L., Rodríguez, F., Coldwell, B., Martín-Lorenzo, A., Barbee, O., D'Auria, L., Chamberlain, K.J., Scarrow, J.H., 2025. Shifting melt composition linked to volcanic tremor at Cumbre Vieja volcano. Nat Geosci. https://doi.org/10.1038/s41561-024-01623-x

Lundstrom, C.C., Hoernle, K., Gill, J., 2003. U-series disequilibria in volcanic rocks from the Canary Islands: Plume versus lithospheric melting. Geochim Cosmochim Acta 67, 4153–4177. https://doi.org/10.1016/S0016-7037(03)00308-9

MacDonald, A., Ubide, T., Mollo, S., Pontesilli, A., Masotta, M., 2023. The Influence of Undercooling and Sector Zoning on Clinopyroxene-Melt Equilibrium and Thermobarometry. Journal of Petrology 64, 1–18. https://doi.org/10.1093/petrology/egad074

Masotta, M., Mollo, S., Freda, C., Gaeta, M., Moore, G., 2013. Clinopyroxene-liquid thermometers and barometers specific to alkaline differentiated magmas. Contributions to Mineralogy and Petrology 166, 1545–1561. https://doi.org/10.1007/s00410-013-0927-9

McKenzie, D.A.N., O'nions, R.K., 1991. Partial melt distributions from inversion of rare earth element concentrations. Journal of petrology 32, 1021–1091.

Mollo, S., Blundy, J., Scarlato, P., De Cristofaro, S.P., Tecchiato, V., Di Stefano, F., Vetere, F., Holtz, F., Bachmann, O., 2018. An integrated P-T-H2O-lattice strain model to quantify the role of clinopyroxene fractionation on REE+Y and HFSE patterns of mafic alkaline magmas: Application to eruptions at Mt. Etna. Earth Sci Rev. https://doi.org/10.1016/j.earscirev.2018.05.014

Neave, D.A., Bali, E., Guðfinnsson, G.H., Halldórsson, S.A., Kahl, M., Schmidt, A.S., Holtz, F., 2019. Clinopyroxene-Liquid Equilibria and Geothermobarometry in Natural and Experimental Tholeiites: The 2014-2015 Holuhraun Eruption, Iceland. Journal of Petrology 60, 1653–1680. https://doi.org/10.1093/petrology/egz042

Neave, D.A., Putirka, K.D., 2017. A new clinopyroxene-liquid barometer , and implications for magma storage pressures under Icelandic rift zones. American Mineralogist 102, 777–794. https://doi.org/http://dx.doi.org/10.2138/am-2017-5968

Pankhurst, M.J., Scarrow, J.H., Barbee, O.A., Hickey, J., Coldwell, B.C., Rollinson, G.K., Rodríguez-Losada, J.A., Martín-Lorenzo, A., Rodríguez, F., Hernández, W., Calvo Fernández, D., Hernández, P.A., Pérez, N.M., Sánchez, F., 2022. Rapid response petrology for the opening eruptive phase of the 2021 Cumbre Vieja eruption, La Palma, Canary Islands. Volcanica.

Paton, C., Hellstrom, J., Paul, B., Woodhead, J., Hergt, J., 2011. Iolite: Freeware for the visualisation and processing of mass spectrometric data. J Anal At Spectrom 26, 2508–2518.

Petrelli, M., Morgavi, D., Vetere, F., Perugini, D., 2016. Elemental imaging and petro-volcanological applications of an improved Laser Ablation Inductively Coupled Quadrupole Plasma Mass Spectrometry. Periodico di Mineralogia. https://doi.org/10.2451/2015PM0465

Putirka, K.D., 2008. Thermometers and barometers for volcanic systems. Rev Mineral Geochem 69, 61–120. https://doi.org/10.2138/rmg.2008.69.3

Putirka, K.D., Mikaelian, H., Ryerson, F., Shaw, H., 2003. New clinopyroxene-liquid thermobarometers for mafic, evolved, and volatile-bearing lava compositions, with applications to lavas from Tibet and the Snake River Plain, Idaho. American Minerologist 88, 1542–1554.

Ranero, C.R., Torné, M., Banda, E., 1995. Gravity and multichannel seismic reflection constraints on the lithospheric structure of the Canary Swell. Mar Geophys Res (Dordr) 17, 519–534.

Romero Ruiz, M. del C., 1990. Las manifestaciones volcánicas históricas del Archipiélago Canario.

Scarrow, J.H., Pankhurst, M.J., Barbee, O.A., Chamberlain, K.J., Morgan, D.J., Longpré, M.A., Tramontano, S., Hickey, J., Neave, D.A., Rollinson, G.K., Stewart, A.G., Wieser, P.E., Coldwell, B.C.,

Hernández, W., D'Auria, L., Pérez, N.M., 2024. Decoding links between magmatic processes and eruption dynamics: whole-rock time series petrology of the 2021 Tajogaite eruption, La Palma. Volcanica 7, 953–980. https://doi.org/10.30909/vol.07.02.953980

Schnetzler, C.C., Philpotts, J.A., 1970. Partition coefficients of rare-earth elements between igneous matrix material and rock-forming mineral phenocrysts—II. Geochim Cosmochim Acta 34, 331–340.

Tenzer, R., Bagherbandi, M., Vajda, P., 2013. Global model of the upper mantle lateral density structure based on combining seismic and isostatic models. Geosciences Journal 17, 65–73. https://doi.org/10.1007/s12303-013-0009-z

Torres-González, P.A., Luengo-Oroz, N., Lamolda, H., D'Alessandro, W., Albert, H., Iribarren, I., Moure-García, D., Soler, V., 2020. Unrest signals after 46 years of quiescence at Cumbre Vieja, La Palma, Canary Islands. Journal of Volcanology and Geothermal Research 392, 106757. https://doi.org/10.1016/J.JVOLGEORES.2019.106757

Turner, S., Hoernle, K., Hauff, F., Johansen, T.S., Klügel, A., Kokfelt, T., Lundstrom, C., 2015. 238 U–230 Th–226 Ra disequilibria constraints on the magmatic evolution of the Cumbre Vieja volcanics on La Palma, Canary Islands. Journal of Petrology 56, 1999–2024.

Ubide, T., Márquez, Á., Ancochea, E., Huertas, M.J., Herrera, R., Jesús Coello-Bravo, J., Sanz-Mangas, D., Mulder, J., Macdonald, A., Galindo, I., 2023. Discrete magma injections drive the 2021 La Palma eruption. Sci Adv.

Villemant, B., Jaffrezic, H., Joron, J.-L., Treuil, M., 1981. Distribution coefficients of major and trace elements; fractional crystallization in the alkali basalt series of Chaine des Puys (Massif Central, France). Geochim Cosmochim Acta 45, 1997–2016.

Weis, F.A., Skogby, H., Troll, V.R., Deegan, F.M., Dahren, B., 2015. Magmatic water contents determined through clinopyroxene: Examples from the Western Canary Islands, Spain. Geochemistry, Geophysics, Geosystems 16, 2127–2146. https://doi.org/10.1002/2015GC005800

Wieser, P.E., Petrelli, M., Lubbers, J., Wieser, E., Özaydın, S., Kent, A.J.R., Till, C.B., 2022. Thermobar: An open-source Python3 tool for thermobarometry and hygrometry. Volcanica 5, 349–384. https://doi.org/10.30909/vol.05.02.349384

Wilson, J.T., 1973. Mantle plumes and plate motions. Tectonophysics 19, 149–164.